Faculté des Sciences
Département de Physique - Unité de recherche CESAM
Group for Research and Applications in Statistical Physics

Bubbles under electric or magnetic field

Dissertation présentée par

Sébastien Mawet

assistant au département de Physique
en vue de l'obtention du titre de
Docteur en Sciences Physiques

Année académique 2022-2023

Jury Members

Pr. Ngoc Duy Nguyen	President
Dr. Eric Bousquet	Secretary
Pr. Hervé Caps	Supervisor
Dr. Stéphane Dorbolo	Co-Supervisor
Dr. Baptiste Darbois Texier	
Pr. Florence Elias	
Pr. Benoit Scheid	

Cover illustration: Flying bubbles
Joséphine Van Hulle, Florence Mignolet and Sébastien Mawet

Bookmark front illustration: Taylor cone
Barbara Linon and Sébastien Mawet

Bookmark back illustration: Ferrofluid bubble
Sébastien Mawet

Acknowledgments

Que ce soit à ses débuts, lors de son déroulement ou encore de son aboutissement, notamment avec la rédaction du présent manuscrit, de nombreuses personnes m'ont aidé, encouragé, encadré et, de manière plus générale, ont participé d'une manière ou d'une autre à ce projet, à cette thèse. Sans vous, ça n'aurait pas été pareil et je ne sais pas si j'y serais arrivé. J'aimerais donc prendre le temps de vous remercier, en espérant n'oublier personne...

Je tiens tout d'abord à remercier Eric Bousquet, Hervé Caps, Baptiste Darbois-Texier, Stéphane Dorbolo, Florence Elias, Duy Nguyen et Benoit Scheid d'avoir accepté de lire ma thèse et de faire partie de mon jury. J'en suis à la fois honoré et heureux. J'espère être à la hauteur de vos attentes.

Un merci tout particulier à mon promoteur, Hervé Caps, qui sans vraiment le savoir, une fin d'après-midi d'un jour de mai au fin fond du cercle de physique, m'a permis de transformer ce qui n'était jusqu'alors qu'une envie, une idée, en un projet dans lequel j'ai pu me développer et m'épanouir. Je suis très heureux d'avoir pu bénéficier de tes conseils durant ces 7 années. Tes multiples casquettes ont fait que nous n'avons pas pu avoir autant d'interactions qu'ont habituellement un superviseur et son doctorant, mais il n'empêche que tu as indubitablement su mettre à profit ces dernières pour me communiquer la manière dont tu fais de la physique. Tu as également été là pour me rassurer dans les moments les plus difficiles, pour me soutenir dans mes projets et pour me pousser lorsque je n'osais pas avancer. En un mot comme en mille, on peut dire que la qualité a primé sur la quantité. Merci pour tout !

La seconde personne à qui j'aimerais adresser des remerciements particuliers est mon co-promoteur, Stéphane Dorbolo. Tu m'as récupéré (au sens propre du terme) à mi-parcours, au moment de ma thèse où j'étais au plus mal. Rien ne t'y obligeait et sans ce geste, je ne sais pas si j'aurais été capable de tenir la barre jusqu'à bon port. Tu as été la présence quotidienne qui m'a permis d'avoir un point de repère, tu as su

me conseiller, et ce malgré le fait que j'arrivais avec un sujet qui n'était pas le tien et beaucoup de casseroles à nettoyer. Merci pour tes idées, ta présence, ton soutien, tes attentions, ta patience et aussi merci d'avoir supporté mon côté perfectionniste qui, combiné à certaines phases de remise en question, a pu être compliqué à gérer. Encore désolé pour le Mauve, je n'ai compris que bien trop tard que c'était lié à une rivalité de coeur… À défaut de l'avoir fait dans l'article, j'ai retiré toute mention de cette couleur dans la thèse.

Merci à Florence Elias d'avoir accepté de me prendre en stage pendant 3 mois malgré l'organisation de dernière minute. Ce stage est arrivé à point nommé. Ton encadrement m'a beaucoup apporté et j'ai énormément appris durant ces quelques mois de temps. Merci beaucoup pour l'accueil.

Merci à Duy Nguyen. Votre enthousiasme à proposer aux étudiants un cours le plus stimulant possible est ce qui m'a motivé à donner le meilleur de moi-même pendant ces 6 années d'électronique. Votre bienveillance et votre soutien sont très certainement les raisons pour lesquelles j'aime toujours enseigner aujourd'hui. Merci également à tous mes co-assistants d'élec : Bruno, Alain, Emile et Thomas. Savoir que je pouvais compter sur vous lors des galères les a rendues plus simples à gérer.

Merci à Eric Bousquet, pour tous les moments passés au troisième étage avant le déménagement. Ton intérêt, ta sympathie et ton enthousiasme font qu'il est toujours agréable de pouvoir discuter de science, de tout et de rien avec toi. De manière plus générale, merci à tous les membres de l'ex-pôle matériaux du troisième. Partager l'étage avec vous était génial, sachez que ce n'est plus du tout pareil sans vous. Un merci particulier à Alain et Jordan, le temps passé à discuter et à déguster toute la nourriture que vous apportiez a grandement contribué à mon équilibre mental.

Durant ces années, j'ai occupé deux bureaux que j'ai partagés avec des gens exceptionnels. Tout d'abord, merci à celle avec qui j'ai cohabité le plus longtemps : Flo, Flosi la séditieuse, Picaflo, … le nombre de surnoms que je t'ai donné durant toutes ces années n'est égalé que par tout ce que tu as pu m'apporter. Merci de m'avoir supporté (au sens anglais du terme), tu as su me motiver ou me soutenir quand j'en avais

besoin. Aussi, merci pour nos désaccords et les discussions qui en ont découlé, elles m'ont permis de ré-envisager de nombreux sujets. Merci pour les moments passés sur le marché de Noël et ailleurs pour trouver des cadeaux ou simplement se détendre. Merci d'avoir partagé avec moi tes instants de pause, tes envolées artistiques et la découverte des Naïades de la Hoëgne, d'avoir participé au marathon "The Riddle", en autres (c'est grâce à toi que je reconnais Nik Kershaw à coup sûr à tous les blind-tests), d'avoir relu ces presque 200 pages, de m'avoir partagé tes goûts musicaux et littéraires et initié aux frites sauce mayo/lapin... Si la période de COVID a eu un point positif, c'est qu'elle nous a rapprochés. Tu es une personne avec qui j'aime être, tout simplement. Ne change rien, tu es géniale. Merci !

Merci aussi à mon Bobo d'amour qui m'a suivi lors de mon déménagement. Tes petites photos qui me donnent de tes nouvelles me font toujours plaisir. Ton accueil pour le jeune doctorant que j'étais a été très important. Merci pour les délires, les voyants médiums marabouts guérisseurs de portable par téléphone. ZEGEMA BEACH et SAFARI l'ami. Merci également à Sofiene, même si tu étais toujours entre Gembloux et Liège, ta présence et ta sympathie ont fait de toi un collègue de bureau exceptionnel. Thanks to Maxime, Maryam, Way, Intesaaf, Pierre-Brice, and Marion, even if some of you only stayed a few months in the office, I thank you, because all of you, in your own way, made our office a pleasant place.

Au-delà des portes du bureau, c'est également toute une équipe, celle du GRASP, à laquelle je me suis intégré. En particulier un énorme merci à Josi. Tu as été une présence solaire durant ma thèse (et avant aussi d'ailleurs). Passer du temps en ta compagnie a toujours eu le don de me remonter le moral. Merci également pour ton soutien, nos longues discussions, les soirées jusqu'à pas d'heure, ton rire communicatif, les tests de personnalité et pour me faire confiance au point d'être convaincue de m'avoir confié tes clés lorsque tu as trop bu (j'espère que cette phrase est assez longue). Ta présence durant ces années m'a permis de rendre les moments difficiles plus supportables et de sublimer ceux de joie. Merci aussi à Floflo, pour tes avis sur l'esthétisme, ton écoute qui m'a permis de garder le cap et pour ta bienveillance à mon égard. L'attention que tu portes à ce que la forme porte le fond est toujours

une inspiration pour moi.

Merci à Galien de m'avoir accueilli et montré les premières ficelles, passer du temps à discuter avec toi est toujours un plaisir. Merci à Charlotte d'avoir pu s'intégrer parmi tous ces physiciens et pour ton amour des restaurants que tu nous fais partager. Merci d'avoir accepté de relire cette thèse jusqu'à la dernière ligne et pour tes gentils commentaires. Merci Geoffroy pour avoir pris le temps de prendre de mes nouvelles, pour les temps de midi et pour ton avis en tant que membre de mon comité. Merci à Jean pour tes avis ingénieux sur les choses. Merci à Christophe de m'avoir permis de profiter de tes talents de MJ. Merci au Professeur Vandewalle de m'avoir appris, à son corps défendant, que pour avancer, il faut parfois renoncer. Merci à Alexis, pour avoir été, que ce soit pendant nos études ou pendant la thèse, toujours disponible pour parler physique. Merci à Martial, Eric et Salvator pour les vols paraboliques. Merci aussi à Martin, Laurent, Baptiste, Alexis, Charles, Michaël, Martin, Nicolas, Ylona, Nathan, Megan, Matteo, Adrien et de manière plus générale à tous ceux qui sont passés par le laboratoire durant ces années, vous m'avez tous marqué à votre manière.

Merci aux membres de l'AGEM. Médéric, je pense que c'est en bonne partie grâce à ma capacité à traduire ce que tu m'expliquais en students-readable que j'ai pu donner le cours d'électronique correctement. Ta passion pour cette dernière et ton envie de la partager sont contagieuses. Merci aussi de m'avoir initié à Python à travers tes scripts. Merci à Olivier, Olivier, Chouaib, Michel et Samuel d'avoir toujours été disponibles dès que j'avais une demande et pour les débriefings de fin de journée. Merci à Alice pour ta gentillesse et ton accueil. Les temps de midi en ta compagnie étaient toujours un bon moment. Merci à Jean-Yves pour les cafés et les discussions, pour tes avis et tes mises en garde qui m'ont évité bien des soucis. Merci à Benoit d'avoir été membre de mon comité de thèse. Je suis toujours ressorti de nos réunions avec plein de nouvelles idées et de pistes à creuser.

Merci à Judith, ma marraine de physique, qui, dès mon arrivée, a été une présence rassurante qui m'a toujours guidé. Ton énergie et ton soutien sont très importants pour moi. Merci à Matthieu, Laurent, David, Jacqueline, Clementine, Lyne, Elodie et plus généralement à tous les membres des départements de physique et d'astrophysique. Si

y donner des cours a été si agréable, c'est grâce à votre volonté que tout se passe pour un mieux et à nos échanges. Merci à Bruno, Daniel, Dorian, François, Pauline et Pierre-Xavier pour les temps de midi dans vos bureaux. Un merci particulier à Pierre-Xavier pour les longues discussions autour d'un dernier(s) verre(s). Merci à Stéphanie, Audrey, Hervé et Bernard de m'avoir permis de faire partie de l'aventure Science et Culture, ce fûrent des moments mémorables.

Un immense merci à Pauline ou Pauli-(à compléter selon l'humeur du moment), avec qui j'ai partagé toutes mes années depuis mon arrivée en physique. Je ne pourrai jamais te dire au combien ces moments ont été fondamentaux pour moi. Si je suis là où j'en suis, c'est en partie grâce à toi. Ta bienveillance, tes idées, tes combats, couplés à ton écoute et ta tolérance, m'ont permis de développer mes opinions et ont fait de moi quelqu'un de meilleur. Tu fais partie des personnes qui me poussent à aller chercher le meilleur de moi-même et je n'arrive même pas à imaginer ce qu'auraient été ces années sans ta présence. Merci d'avoir veillé sur moi, en particulier quand je ne savais plus refaire mes lacets. Merci pour tout. Merci Lucas pour les heures passées à se détendre, que ce soit dans La faille, dans les mers chaudes des Caraïbes ou dans tout autre univers. Passer du temps avec toi est toujours un plaisir et je sais que je peux compter sur toi en cas de coup dur. Avec Pauline, William et Ezra vous formez une magnifique famille qui est pour moi un écrin de paix dans lequel je peux me reposer. Merci à Nicolas pour nos discussions phyloso/hysto/physique en terrasse. Tu es une personne exceptionnelle et comme ce à quoi notre nom semblait nous prédestiner, un second frère pour moi. Kevin, Maëva, merci pour les instants passés avec vous, votre intérêt et vos encouragements. Chaque fois que l'on se voit, vous m'apportez une bouffée d'air frais, je vous adore. Merci aussi à Manon et Martin, pour votre accueil et l'initiation au LARP. Chez vous, je me sens un peu chez moi et ça, ça n'a pas de prix. Merci à Joseph, France, Margaux, Thierry, Fabian, Julien pour nos années d'études passées ensemble.

Maxime, merci d'être la personne que tu es. On se connaît depuis trop longtemps pour que je puisse faire une liste de nos aventures, mais en vrac : merci pour Peine et Panique, pour les soirées chez toi, de ne pas avoir retenu les paroles de ma superbe chanson, pour tes conseils

cinématographiques (je vais peut-être avoir le temps de me rattraper un peu), … Je sais que tu seras toujours disponible si j'ai besoin de toi et je t'en suis reconnaissant. Merci à Léna d'être toujours présente après toutes ces années, les moments qu'on passe ensemble sont toujours aussi agréables. Merci à Marine pour les dîners chez poivre et sel et la complicité après toute ces années. Merci à Valentin et Alix pour les blind-test, les soirées et tout le reste. Merci à Estelle, Gabriel, Noël, Anne, Sophie, Caroline et de manière générale à tous mes amis Verviétois/Nivezétois et Jalhaytois (ou futur ?). Votre bienveillance et votre accueil sont la raison pour laquelle je me sens chez moi à Sart. Merci à Barbara pour la superbe photo du marque-page. Merci Jessica, pour tous les trajets passés ensemble, prendre le train avec toi rendait ce moment agréable. Merci à Florence, ma conductrice, qui est devenue bien plus que cela au fil des années. Les heures de co-voiturage passées ensembles étaient autant d'heures de débriefing qui me faisaient un bien fou. Merci beaucoup, je suis heureux d'être venu te filer un coup de main pour ton lecteur de cartes.

Enfin, merci à ma famille. À mes oncles et tantes qui se sont intéressés à mes bulles. En particulier à Tony pour son préambule. À Granny et Daddy qui m'ont accueilli sans compter durant mes sessions et lorsque j'ai du commencer la rédaction. À Papy et Mammy qui ont toujours cru en moi et su y voir le meilleur. Merci à mon frère, ma soeur et à mes parents de m'avoir soutenu pendant toutes ces années, y compris pendant les moments les plus compliqués. En particulier, je tiens à remercier mes parents de m'avoir nourri/logé/blanchi pendant mes années de thèse, et surtout permis de rester dans le cadre magnifique qu'est notre région. Sans vous je n'y serais pas arrivé. Merci.

Contents

Abstract

A Bubble is a biphasic object in every sense of the word. First, as a concept. Indeed, its production is within everyone's reach as long as they have soap, a frame and their breath at their disposal. Yet, the physics behind their very existence and the phenomena associated with them remain puzzling questions that involve complex notions. Second, they are literally made up of two phases: a gaseous and a liquid. The combination, nature and distribution of these phases are responsible for the unique behaviour of bubbles. Among other things, bubbles are easily deformed by external fields, which make them a wonderful object to highlight their effects.

In this work, we investigate the different effects that external fields and the body forces related to them have on the bubbles shapes. More precisely, we describe the deformation that bubbles undergo under an electric or a magnetic field. These reshaping are linked both to the applied fields properties and to those of the liquids used to make the bubbles. In addition, the substrate also appears to have an influence on the deformation. We show that these dependencies can be expressed by dimensionless numbers that describe the competition between the forces involved. Moreover, we find that the functions relating the shapes and these dimensionless numbers are linear under weak fields. We obtain these linear functions and, using them, we properly define what weak fields are. With these results, we are able to propose a general guide on how to handle, control and deform bubbles. Furthermore, by comparing the deformation of bubbles and droplets under similar fields, we demonstrate that bubbles are a wonderful object to illustrate the very nature of the forces acting on them.

Résumé

La Bulle est un objet biphasique dans tous les sens du terme. Tout d'abord, en tant que concept. En effet, sa production est à la portée de tous, pour peu que l'on dispose de savon, d'un cadre et de son souffle. Cependant, la physique qui sous-tend leur existence même et les phénomènes qui y sont associés restent des questions compliquées qui peuvent faire appel à des notions complexes. Deuxièmement, elles sont littéralement constituées de deux phases : une gazeuse et une liquide. La combinaison, la nature et la répartition de ces phases sont à l'origine du comportement unique des bulles. Entre autres, les bulles peuvent être facilement déformées par des champs externes, ce qui en fait un objet merveilleux lorsqu'il s'agit de mettre en évidence leurs effets.

Dans ce travail, nous examinons les effets que les champs externes et les forces qui y sont liées ont sur la forme des bulles. Plus précisément, nous y décrivons la déformation que subit une bulle sous l'effet d'un champ électrique ou magnétique. Ces nouvelles formes sont liées à la fois aux propriétés des champs appliqués et à celles des liquides utilisés pour fabriquer les bulles. De plus, nous y constatons que le substrat a également une influence sur les déformations. Nous montrons que ces dépendances peuvent être exprimées sous forme de nombres sans dimension qui décrivent la compétition entre les forces impliquées. En plus de cela, nous trouvons que les fonctions qui relient la forme aux nombres sans dimension sont linéaires si les champs sont faibles. Nous obtenons ces fonctions linéaires et, en les utilisant, nous définissons proprement à quoi correspondent les champs faibles. Grâce à ces résultats, nous sommes en mesure de proposer un guide général sur la façon de manipuler, contrôler et déformer les bulles. En outre, en comparant les déformations subies par une bulle et une goutte sous des champs similaires, nous démontrons que les bulles sont des objets qui illustrent merveilleusement la nature même des forces qui agissent sur elles.

Publications

This thesis is based on work that has been peer-reviewed and published, as well as on another that is in preparation. They are listed below:

S. Mawet, H. Caps and S. Dorbolo, *Deformation of soap bubbles in uniform electric fields*, Phys. Rev. Fluids **6**, 043603 (2021).

S. Mawet, H. Caps, S. Dorbolo and F. Elias, *Deformation of ferrofluid bubbles in uniform magnetic fields* (in preparation).

A. Cazaubiel, S. Mawet, A. Darras, G. Grosjean, J.J.W.A. van Loon, S. Dorbolo and E. Falcon , *Wave Turbulence on the Surface of a Fluid in a High-Gravity Environment*, Phys. Rev. Lett. **123**, 244501 (2019).

I also had the opportunity, during my Ph.D. thesis, to work on other projects and one of them resulted in a publication:

M. Noirhomme, A. Cazaubiel, E. Falcon, D. Fischer, Y. Garrabos, C. Lecoutre-Chabot, S. Mawet, E. Opsomer, F. Palencia, S. Pillitteri and N. Vandewalle, *Particle Dynamics at the Onset of the Granular Gas-Liquid Transition*, Phys. Rev. Lett. **126**, 128002 (2021).

Make a soap bubble and observe it; you could spend a whole life studying it.

Sir William Thomson, Lord Kelvin

1 Preamb(ul)le

In French, the word Physics is read *physique* and can be an adjective or a noun. In both cases, its primary definition is to describe what belongs to the natural or material world, as opposed to the psychic (*psychique* in French) or spiritual one. The science that shares the same name, unsurprisingly, aims to describe and explain the laws that govern this material world, namely to study the interaction between matter and the forces that act upon it. Moreover, since matter is made up of constitutive particles, its characteristics result from the particles interactions with their environment as well as from their intrinsic properties.

Of all of them, the state of matter is certainly the property that we experience most in our daily lives. Indeed, no one wants to live in a house made of melting bricks, take a shower with hailstones or, even worse, drink evaporated beer. As these examples illustrate, matter appears mainly in three different states in our daily lives: solid, liquid and gaseous (other states, such as plasma, exist, the sun being the best example, but are far less common). Each of these states has general properties that we can define based on both our sensitive experience and on physics. In a solid, the constitutive particles are strongly bound together and form a lattice, giving the solid its defined shape and volume as well as its structural rigidity. Conversely, in a gas, as there is almost no interaction between the constitutive particles, neither the shape nor the volume are strictly defined as they depend only on the container.

Figure 1.1: Illustrative picture of bubbles blown by a physicist dedicated to their study (used with his permission).

Finally, in a liquid, particles are bound, but not as much as in a solid, allowing liquids to share properties with both solids and gases, namely to have a defined volume, but not a defined shape. Because of these properties, a liquid volume can be relatively easily deformed, moved or manipulated with external fields.

Most of the objects we interact with in our lives are in one defined state: the air you breathe right now is gaseous, the water we drink is liquid, and the computer on which I am currently writing these lines is solid. However, some peculiar objects are inherently defined as the combination of two (or more) phases in different states. The central subject of this thesis is precisely one of those biphasic objects: the

bubble[1] (which translates into *la bulle* in French and is illustrated in Fig. 1.1). It is, actually, a pocket of gaseous phase encapsulated inside a liquid phase forming a thin film. These two phases appear in two quite different sizes within the bubbles, with the gas pocket forming a sphere whose typical radius ranges from millimetre to metre and the liquid film having a micrometric typical thickness and a length defined by the gaseous phase. This combination of two phases and their interplay give bubbles their unique behaviour. Among others example of this behaviour, the shape that a bubble takes at a beer surface depends directly on its gas volume, which is defined as the volume enclosed by the liquid film. Furthermore, its lifetime is defined by the drainage inside its liquid film whose curvature is defined by the bubble gas volume. Yet, to say that these behaviours are solely due to the two phases that make up the bubbles is at least incomplete. There is another fundamental element that defines how bubbles react under different conditions: the interfaces between their gaseous and liquid phases. The properties of these interfaces are crucial in the bubble life, allowing for their very existence. Indeed, without the surface tension gradient along its surface, a soapy water bubble would not live more than a few microseconds. But it does not stop there, the interfaces of a bubble impact all its aspect, from its shape to its bursting, via its drainage. Bubbles are therefore not only biphasic objects, but also objects whose overall appearance is greatly influenced by their interfaces.

These different influences make the bubble a multi-scale object. Indeed, as we have just mentioned, the two phases are very different in size: millimetric to metric for the gaseous and micrometric for the liquid. Moreover, the interfacial phenomena that allow for the bubbles' existence, such as the agglomeration of amphiphilic molecules at the said interfaces, take place at the nanometric scale. Furthermore, if the bubble rests on a solid substrate or floats at a liquid surface, a meniscus, containing the vast majority of the liquid, forms at the junction with the liquid/solid substrate and has a typical size of the order of a millimetre. The different scales as well as the combination of surface

[1]Another biphasic object is intensively used in one of the chapters of this thesis: ferrofluids that are colloidal suspensions consisting of solid magnetic particles suspended inside a liquid.

and volume effects that occur in the bubble physics make it a wonderful object not only to study, but also to illustrate how different forces act at different scales and how surface effects interact with volume ones. This obviousness has already become apparent to several great scientists such as, among others, Robert Hooks [1] (1635-1703), Isaac Newton [2] (1643-1727), Charles Vernon Boys [3, 4] (1855-1944) and Cyril Isenberg[2] [5]. Like them, we think that bubbles are a fascinating and scheming subject, worthy of a thesis. Yet a thesis is not only a wonderful subject, it is also puzzling questions that need to be answered.

Due to their popularity, many questions have already been raised about bubbles, however, plenty of them remain unsettled. Given the breadth of choice, we were privileged to be able to choose, and the ones we decided to focus on are directly related to the biphasic nature of bubbles. Indeed, as bubbles consist of a liquid and a gas, they are easily deformed by external fields while having a defined volume due to the liquid thickness. We therefore decided to focus on how a bubble can be manipulated and more precisely deformed by an external field derived from a body force such as gravity, electricity or magnetism. More precisely, we focused on the effect of electric and magnetic field on the bubbles shape because a lot has already been done about gravity [6, 7, 8] and there are still some grey areas, despite the pioneer works of Taylor [9] and Macky [10] on bubbles under electric field. Moreover, to our knowledge, no one has tried to characterise the effect of a magnetic field on ferrofluid soap bubbles. This primary question raises another equally interesting one: how and where do the body forces manifest their effects on the bubbles? Indeed, due to the nature of both bubbles and forces, we expect the different body forces to act very differently on the bubble. On the one hand, the magnetic and gravitational forces are volume forces. However, the magnetic force should only influence the liquid phase of the bubble, mainly concentrated in the meniscus area, whereas gravity is expected to influence both the gaseous and liquid phases. On the other hand, the electric force that acts on a perfectly conducting liquid is a pure surface force, similarly to the force due to surface tension. Accordingly, the electric force should modify the whole

[2]Visit www.youtube.com/watch?v=Np9TuarsoX8 to watch one of his physics lectures about soap bubbles and films, among other topics.

bubble since it acts on its entire surface. Thanks to their biphasic and multi-scale nature, bubbles are therefore perfectly suited to probe and illustrate the volume or surface nature of the force that act on them.

Usually, good storytellers should not reveal the outcome of their plot before the ending and especially not at the beginning. Yet, I have decided not to follow this practice, inherited from thousands of years of tales and legends, and to answer the questions we have just clarified right now. Firstly, yes, the electric body force only acts at the surface of a conductor, deforming the whole sessile (or floating) bubbles from a hemispherical to a hemi-spheroidal shape and inducing a Taylor cone[3] for a sufficiently strong electric field, in a fashion quite similar to what it does on droplets. Secondly, yes, the magnetic body force directly acts within a ferrofluid, only deforming it instead of the entire bubble. Since the vast majority of the liquid that makes up a sessile bubble is located at its foot, in the meniscus, the latter is most impacted by the magnetic field. This induces a reshaping of the sessile bubble from a hemisphere to a spherical cap sitting atop of a cylinder, a completely different deformation from that of a droplet under similar conditions. These main results are summarised in the graphical abstract of this thesis presented in Fig. 1.2. The effects of the electric and magnetic fields on bubbles and droplets are put face to face to allow for a comparison. This parallel highlights two facts. First, the electric force on a conductor is indeed a surface effect, thus inducing a similar effect on bubbles and droplets. Second, the magnetic force on a ferrofluid is undoubtedly a volume effect, consequently deforming bubbles and droplets in completely different ways. These conclusions are related to the nature of the force and seem pretty obvious in addition to being known for centuries. This is why I am taking liberties with the usual good writing practices. Indeed, the purpose of this thesis is not to prove you that the electric and magnetic forces act respectively at the liquid surface and inside its volume, but rather to show you that bubbles and their deformations are a wonderful way to illustrate it. Furthermore, the work and reflection that allow us to re-obtain these notorious conclusions and to rationalise the deformations are certainly much more interesting than the conclu-

[3]Named after Geoffrey Ingram Taylor (1886–1975), an English mathematician, physicist, aerodynamicist and meteorologist [11]

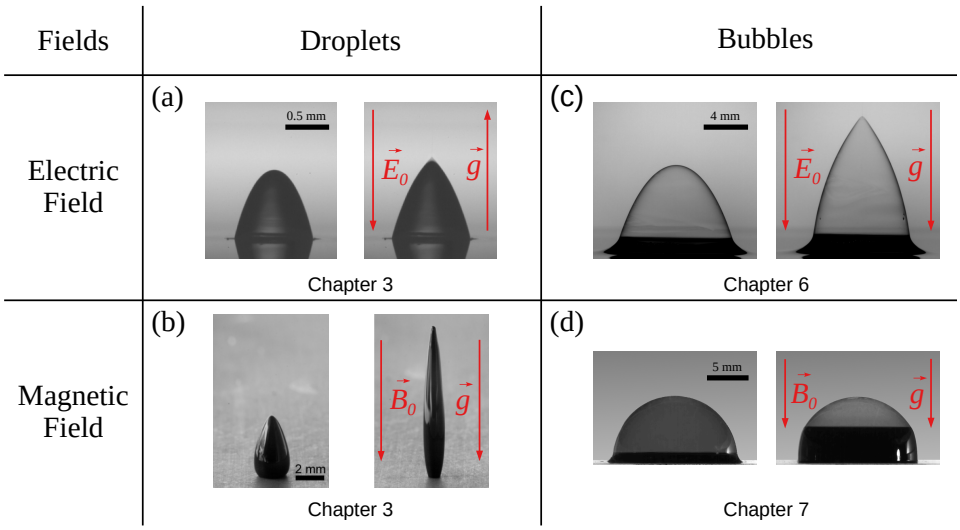

Figure 1.2: Graphical abstract. The deformation undergone by droplets (first column) and bubbles (second column) are compared when subjected to an electric (first row) or magnetic (second row) field. (a) Pictures of conducting pendant droplets pinned on a conducting surface and subjected to a uniform electric field $\vec{E}_0$ [V/m] taken from the article of Beroz *et al.* [12] (the direction of the electric field and gravity as well as the scale have been added). In the left picture, the intensity of the field E_0 is just below that needed to trigger the droplet instability, namely the Taylor cone, whereas in the right one, E_0 is sufficient to trigger it. (b) Pictures of ferrofluid droplets on a superhydrophobic substrate subjected to a magnetic field $\vec{B}_0$ [T] from the paper of Timonen *et al.* article [13] (the direction of the magnetic field has been added). The intensity of the magnetic field B_0 (as well as its gradient along the vertical direction) is increased between the left and right pictures. (c) Pictures of bubbles floating on their constitutive conducting soap mixture and exposed to a uniform electric field from [14]. Similarly to droplets, the right and left pictures display respectively a bubble under a field intensity just above and below that required to prompt the Taylor cone. (d) Pictures of ferrofluid soap bubbles resting on a microscope slide under the influence of a uniform magnetic field. The field intensity increases between the left and right pictures.

sions themselves. The laws we obtained allow us to clarify the physics that drives the deformation and therefore to provide a general guide on how to handle, control and especially deform bubbles.

To answer the questions of how and where bubbles are deformed by electric or magnetic fields (in order to provide you with a general guide to manipulate them) and to convince you that bubbles are indeed well suited to reveal the nature of the forces acting on them, we used the following framework. As a bubble consists of two fluid phases, the next chapter, Ch. 2, is devoted to present the equations that describe the fluid motion and the conditions at their interfaces. Once the equations are presented, the pressure differences linked to the different body forces are highlighted through their effects on the waves at the liquid surface. After this initial approach, Ch. 3 is used to describe the effect of a body force on droplets. Indeed, as shown in Fig. 1.2, within this thesis, droplets are used in comparison to bubbles, serving as a seed point for reflection and highlighting the nature of the deforming forces. Thanks to these two introductory chapters, all the concepts necessary to tackle the main subject of this thesis will have been developed and Ch. 4 can therefore focus on it. More precisely, the bubble is quantitatively defined with its various scales and peculiarities and these are linked to the main questions of this thesis. Each of the following chapters is devoted to describing bubbles under different fields. In Ch. 5, the different shapes adopted by sessile or floating bubbles are presented when the only body force is gravity. In Ch. 6, the deformation induced on sessile and floating conducting bubbles by an external electric field are explored. In this chapter, particular attention is paid to the effect of the substrate on the bubbles deformation and we justify the observations depicted in the first row of Fig. 1.2. In Ch. 7, the deformation due to an external magnetic field on a sessile bubble made of ferrofluid soap is investigated. The meniscus shape reveals the presence of two regimes as a function of the applied magnetic field and the deformations presented in the second row of Fig. 1.2 are also rationalised. Finally, in the last chapter (Ch. 8) we review the work done in order to draw a conclusion and try to answer the various questions that have been raised in this introduction. Furthermore, as with any good scientific subject, the questions we have answered are just as many starting points for new ones. We therefore

propose some of those we would have liked to be able to answer if we had been given an infinite amount of time.

2
Fluid Dynamics and Waves

Dynamics is a fundamental part of physics. Its purpose is to link the motion of a given body to its causes, namely the forces acting on it. The founding principles of dynamics were laid down by Isaac Newton in his famous *Principia* [15] in the form of the no less famous three laws that now bear his name. In particular, Newton's second law directly makes explicit the link between the changes over time of the linear momentum of a body and the sum of the forces acting on that body.

The description of fluid motion, which is the purpose of fluid dynamics, is not different from classical solid dynamics and is therefore based on Newton's laws as well. However, unlike classical solid dynamics, fluid dynamics, and more generally continuous media dynamics, has to deal with body deformation. Because of these deformations, and although Newton's laws already contain all the information about the relationship between forces and changes in momentum, it is convenient to re-express those laws in a more suitable form. Notably, the forces influencing the fluid motion can be sorted into two groups according to the way they act on the fluid. The first kind of forces are body forces (or volume forces) which are related to the presence of fields and act on each element of the fluid. The second group consists of surface forces that only act at the fluid interface. The objective of this thesis is to explore the effect of body forces on bubbles, which are a very particular fluid configuration that can be easily deformed to achieve new equilibrium shapes.

Since bubbles are themselves the result of complex interactions between surface and body forces, it is necessary to explain how each of these forces acts on a fluid. To do this, let us start with a simple initial configuration: a large fluid pool. From our daily experience, we know that such a liquid mass has a flat surface when undisturbed. However, this liquid mass can be disrupted and its surface deformed by external factors. For example, the wind or rain forms ripples on the water surface, while the tides induce waves. Diving into the pool also deforms the surface, causing a splash of varying size depending on the quality of the dive. The way in which the liquid contained inside the pool is deformed under the effect of a perturbation depends on the perturbation itself, but also on the surface and volume forces acting on the liquid. For example, waves in seas and oceans can be explained using wave turbulence theory. This framework allows the derivation of a dispersion relation that highlights the presence of two types of waves depending on the mechanism that tends to bring the liquid back to its steady state: capillary and gravity waves that are due to surface and volume forces respectively. If other body forces are applied, such as an electric or magnetic one, new terms must be added to the dispersion relation in order to describe these new effects.

Waves and their description by wave turbulence theory are used in this chapter to highlight the effect of different body and surface forces on the fluid. In the first two parts of this chapter, the mathematical framework describing fluids and the boundary conditions are presented. Then, the description of the wave formation at the liquid surface when only gravity is present is given. In the next two parts, the effects of an electric field on waves generated at the surface of a conducting liquid and the effects of a magnetic field on waves propagating at the surface of a ferrofluid are exposed. Finally, a conclusion is drawn.

2.1 Equations of Motion

In order to describe the fluid motion and, in particular, its steady shape, we need differential equations describing the motion of the fluid and how this motion is related to the forces acting on the fluid. Mass conservation and Newton's second law of motion fulfil this purpose. The former

rationalises the fact that no matter is created nor destroyed within a fluid volume, thus constraining the velocity field and local density. The second relates the linear momentum variations to the forces acting on the fluid. These equations can be re-expressed under the continuum approximation [16, 17], which means that the fluid properties must vary continuously. Colloidal suspensions, for example, cannot technically be described according to the continuum approximation because they form a two-phase system, inducing discontinuities in the fluid properties [17]. Under the continuum assumption, the continuity equation and the Cauchy equation of motion[1] can be derived [16]. On the one hand, the former can be written as follows

$$\frac{\partial \rho}{\partial t} + \vec{\nabla} \cdot (\rho \vec{u}) = 0, \tag{2.1}$$

with ρ [kg/m^3] the fluid density, $\vec{u} = \vec{u}(x, y, z, t)$ [m/s] the velocity at a given time t [s] and at a point in space (x, y, z) [m] and $\vec{\nabla}$ the nabla operator representing the spatial variation of the field on which it is applied. On the other hand, in the Cauchy equation, the forces are sorted into two groups according to the way they act on the fluid. The first kind, the body (or volume) forces, are capable of acting on the entire fluid volume and are related to the presence of fields such as gravity or electric and magnetic fields. The second kind, the surface forces, are consequences of the continuum approximation. They result from the microscopic molecular structure and act only on the boundaries of the fluid volume. The Cauchy equation reads as follows

$$\underbrace{\rho \left(\frac{\partial \vec{u}}{\partial t} + (\vec{u} \cdot \vec{\nabla}) \vec{u} \right)}_{\substack{\text{Momentum} \\ \text{Variations}}} = \underbrace{\vec{f}}_{\substack{\text{Body} \\ \text{Forces}}} + \underbrace{\vec{\nabla} \cdot \underline{\underline{T}}}_{\substack{\text{Surface} \\ \text{Stresses}}}. \tag{2.2}$$

The left-hand side of the equality is simply the momentum variation per unit volume. The second term is called the advective or inertial term because it describes how a particle in the fluid moves due to the speed of the surrounding fluid mass. The terms on the right-hand side of the equality are respectively the body and surface forces with $\vec{f} = \vec{f}(x, y, z, t)$ [N/m^3]

[1] Named after Augustin-Louis Cauchy (1789–1857), a French mathematician [18].

the body force per unit volume and $\underline{\underline{T}}$ [N/m^2] the stress tensor. The body forces term directly depends on the field used to generate it and can therefore be derived from the associated forces[2]. Conversely, since the surface forces term has a microscopic origin, continuum mechanics cannot provide any basis for deriving its form. To obtain information about the stress tensor $\underline{\underline{T}}$, assumptions about the fluid properties must be made to guess the constitutive equations that relate $\vec{u}$ and $\underline{\underline{T}}$.

Firstly, in many cases the fluid can be considered incompressible, which means that its density is constant throughout its volume. In such a case, the continuity equation 2.1 can be rewritten in a simpler form

$$\vec{\nabla} \cdot \vec{u} = 0. \tag{2.3}$$

The density ρ must be constant everywhere and, therefore, the particles in the fluid cannot accumulate or deplete at any point in the fluid. Therefore, the velocity field cannot concentrate or disperse particles[3].

Two other common assumptions are that the fluid is isotropic and Newtonian. The first assumption means that the intrinsic properties of the fluid are the same in all directions. The second implies that the shear stress is proportional to the strain rate, that is to say that the proportionality constant between them, *i.e.* the dynamic viscosity, does not depend on the shear stress.

The three assumptions made about the fluid properties (incompressible, isotropic and Newtonian) provide the constitutive equations, which then constrain the form of the stress tensor $\underline{\underline{T}}$ (for details of how these constitutive equations are derived and how they impose the form of $\underline{\underline{T}}$, see the second chapter of [16] on pages 45-49). From Eq. 2.2 and thanks to the relations obtained with the constitutive equations, new motion laws for an incompressible isotropic Newtonian fluid can be derived. These equations are the Navier-Stokes equations[4] and read as

[2]For example, the term related to gravity is $\rho\vec{g}$, with $\vec{g}$ [m/s^2] the gravitational acceleration.

[3]An important exception to Eq. 2.3 occurs when there are sources or drains within the fluid. Indeed, since these are points within the fluid volume where particles are injected ("created") or withdrawn ("destroyed"), the divergence of the velocity is not equal to zero everywhere within the fluid volume.

[4]The historical context in which these equations were found and the origin of their name can be found in Ref. [19].

follows

$$\underbrace{\rho\left(\frac{\partial\vec{u}}{\partial t}+(\vec{u}\cdot\vec{\nabla})\vec{u}\right)}_{\substack{\text{Momentum}\\\text{Variations}}}=\overbrace{\vec{f}}^{\substack{\text{Body}\\\text{Forces}}}\underbrace{-\vec{\nabla}P_l+\eta\Delta\vec{u}}_{\substack{\text{Surface}\\\text{Stresses}}}. \tag{2.4}$$

The last two terms are a re-expression of surface forces. The fourth term characterises the stresses normal to the surface, namely the pressures, and the tendency of a fluid to flow in the direction of least pressure, with $P_l = P_l(x, y, z, t)$ [N/m^2] the local pressure. The last term describes the shear stresses, tangential to the surface, and the diffusion of momentum through the viscosity with η [Pa s] the dynamic viscosity. The most common example of an isotropic incompressible Newtonian fluid is water, which is therefore well described by Eq. 2.4.

Given the assumptions made to obtain it, the Navier-Stokes equations are technically only capable of describing a continuous isotropic incompressible Newtonian fluid. Blood, for example, is a colloidal suspension due to its erythrocytes (which are approximately elliptical in shape) and therefore cannot, in principle, be characterised using Eq. 2.4. This is especially true because of the anisotropy of erythrocytes and their deformations induced by shear stresses. However, in large arteries, the length scale of the flow is sufficient to consider the blood as an homogeneous fluid [20]. The applicability of the Navier-Stokes equations can therefore be extended to colloidal fluids if the length scale of the described flow is large compared to the size of the colloidal particles suspended in the fluid. Another example is ferrofluids, which is a colloidal suspension of 10 nm particles bearing a magnetic moment. As far as we are not interested in describing the dynamics of micrometric or smaller flows, ferrofluids are well described by Eq. 2.4. However, Navier-Stokes equations are, in practice, difficult to solve. Indeed, they are non-linear second-order partial differential equations. Finding simpler versions of Eq. 2.4 in specific cases to circumvent this intrinsic complexity is therefore necessary to obtain information about the flow without numerical simulations. Those simpler versions are obtained by making assumptions.

A first way to derive an alternative expression to describe fluid mo-

tion is to compare the two mechanisms that drive the transport of momentum in the fluid, namely advection and diffusion, to determine which of them is dominant. This means that the advective flux of momentum J_a [kg/ms^2] must be compared to the diffusive one J_d [kg/ms^2] [21]. The first is the density of momentum multiplied by the convection speed, which gives $J_a = \rho u^2$ with u the speed of the fluid. The second derives from Fick's law[5] applied to momentum and can be expressed as $J_d = \eta u/L$, where L [m] is the characteristic length of the system. Dividing one by the other defines a dimensionless number, the Reynolds number[6], which reads as follows

$$\mathrm{Re} = \frac{\rho u L}{\eta}. \tag{2.5}$$

This dimensionless number compares the relative importance of advection and diffusion processes. If the Re $\ll 1$, diffusion transport dominates the flux and the non-linear term describing advection can be neglected. This regime will be the nest of this thesis.

If the flow is stationary, while occurring at a low Reynolds number, the term describing the variation of velocity with time can also be cancelled out and we are left with the Stokes equations describing the steady flow of viscous fluids:

$$\eta \Delta \vec{u} = \vec{\nabla} P_l - \vec{f}. \tag{2.6}$$

The Stokes equations are particularly well suited to describe the dynamics of fluids confined in a single direction [21], such as the drainage taking place in the liquid thickness of a soap bubble. Indeed, confinement induces a velocity variation nearly exclusively in the direction perpendicular to the flow, while the velocity itself as well as the pressure difference are in the direction of the flow. The viscous transport in such a configuration largely dominates and the dynamics is therefore described by Eq. 2.6.

The second alternative expression of Eq. 2.4 is obtained for the steady flow of an incompressible and inviscid fluid. In this case, the

[5]Named after Adolf Eugen Fick (1829-1901), an German physiologist [11].

[6]Named after Osborne Reynolds (1842-1912), an English physicist and engineer [11].

only transport of momentum in the fluid is advective and the viscous term in Eq. 2.4 is null. Provided that the body forces are conservative, the equations can be re-expressed as follows [22][7]:

$$\rho\vec{u} \times (\vec{\nabla} \times \vec{u}) = \vec{\nabla}(\frac{1}{2}\rho u^2 + P_l + P_f), \tag{2.7}$$

with $(\vec{\nabla} \times \vec{u})$ [s^{-1}], the vorticity and $\vec{f} = -\vec{\nabla}P_f$, P_f [N/m^2] being the pressure associated with the body forces[8]. If the flow is irrotational, the left-hand side of the equality is null. Therefore, the derivative of the quantity on the right-hand side of the equality is zero and this quantity must be constant throughout the fluid [22], giving

$$\frac{1}{2}\rho u^2 + P_l + P_f = \text{cst}. \tag{2.8}$$

This equation is known as the Bernoulli equation[9]. In particular, if the fluid is still and has reached its equilibrium shape, the velocity is null and Eq. 2.8 can be rewritten as follows

$$P_l + P_f = \text{cst}. \tag{2.9}$$

This last equation is a generalisation of Pascal's principle[10] to any type of conservative body forces and is of paramount importance in this thesis as it relates the pressure inside the fluid P_l to the pressure induced by the various body forces P_f acting on the fluid. The steady shapes adopted by a bubble directly depend on the pressure P_f that body forces apply to the bubble. It should be noted that Eq. 2.9 can be obtained directly by imposing a null velocity in Eq. 2.4. This means that in addition to the assumption made to obtain Eq. 2.4, the only two conditions for Eq. 2.9 to be applicable are that velocity must be null and that the body forces must be conservative. Indeed, the zero velocity condition

[7]The vector identity $(\vec{u} \cdot \vec{\nabla})\vec{u} = \frac{1}{2}\vec{\nabla}(u^2) - \vec{u} \times (\vec{\nabla} \times \vec{u})$ is used to obtain the equation.

[8]For example, the pressure due to gravity is $P_f = \rho g z$, with z [m] the fluid height.

[9]Named after Daniel Bernoulli (1700–1782), a Dutch mathematician [18].

[10]Named after Blaise Pascal (1623–1662), a French mathematician and physicist [18].

makes any other assumption about the velocity and flux of momentum unnecessary.

All equations derived here relate forces per unit volume, pressures and velocities at different locations in the fluid. Yet, in order to obtain the absolute values of these quantities everywhere in the fluid, they must be known at at least one of its point. The boundary conditions fulfil this purpose by giving these quantities at the fluid interfaces. The form of these boundary conditions is presented in the next section.

2.2 Boundary Conditions

The continuum approximation in which the equations of motion have been derived states that the material properties of the fluid must vary continuously within it. However, in the vicinity of the fluid boundaries (which may either be solid/fluid or fluid/fluid boundaries), these properties vary abruptly from the values in one bulk phase to those of the other. Boundary conditions reflect this discontinuity and, in the same fashion as the stress tensor, are consequences of the continuum approximation. They also result from microscopic interactions within both media and, therefore, cannot be deduced from the continuum approximation.

Boundary conditions can be sorted into three groups: kinematic, dynamic and stress conditions. The last two are derived from assumptions, while the first can be inferred directly from mass conservation. Indeed, considering that the interface is not a source or sink of mass (*e.g.*, no evaporation nor solidification of a liquid phase), the net flux of mass across the interface must be zero. Assuming that the shape of the interface is constant over time[11], the kinematic condition takes the following form:

$$\vec{u}_1 \cdot \vec{n} = \vec{u}_2 \cdot \vec{n}, \tag{2.10}$$

with $\vec{u}_1$ [m/s] and $\vec{u}_2$ [m/s], the velocity in the first and the second bulk phases respectively and $\vec{n}$, the dimensionless vector, normal to the

[11]For a generalisation of the kinematic condition in the case of a phase transition between the two bulk phases and for a time dependent interface, see Ref. [16] on pages 67-68 and 74-75, respectively.

interface[12]. This condition simply requires that the normal component of the velocity is continuous across the interface.

For their part, the dynamic boundary condition concerns the two tangential components of the velocity across the interface. However, unlike the kinematic condition, there is, strictly speaking, no fundamental macroscopic principle on which to build. Yet, the energy conservation and, in particular, the fact that the stress tensor cannot diverge at the interface, guide the assumptions that need to be made to obtain this condition. In most cases, the no-slip condition, which simply imposes that the tangential components of the velocity are continuous across the interface, applies. This condition can be written as follow

$$\vec{u}_1 \cdot \vec{t} = \vec{u}_2 \cdot \vec{t}, \tag{2.11}$$

with $\vec{t}$, any dimensionless vector, perpendicular to $\vec{n}$ and consequently tangential to the interface. More general dynamic conditions exist, such as the Navier-slip condition which allows slip at the interface, but we will stick to the no-slip condition in this thesis since drainage is not its main subject[13]. Altogether, the kinematic condition and the no-slip condition impose a continuous velocity across the interface. For a fluid/solid interface with an impermeable solid and a known solid motion, these two conditions are sufficient to determine the fluid velocity at the interface (and thus throughout the fluid through the equations of motion). However, for a fluid/fluid interface, three additional equations are needed and these are the stress conditions.

These conditions arise from the balance of forces on the interface. Indeed, because the interface is seen as a surface of zero thickness, there is no mass associated with it. Consequently, the sum of all the forces acting on the interface must be equal to zero in order to avoid infinite acceleration. In the same spirit as for $\underline{\underline{T}}$, constitutive properties of the interface must be assumed to characterise the forces equilibrium. The simplest constitutive property that can be used to describe an interface is that it is entirely characterised by a surface tension γ [N/m]. Under

[12]The normal can be chosen pointing to either medium, but by convention we choose to define it as pointing away from the medium we are describing.

[13]Interested readers may wish to consult Ref. [16] on pages 69-74 for more information on these more general conditions.

this assumption, two types of forces act on the interface: the surface forces acting on both its faces and a tensile force due to the surface tension, which acts in its plane. The balance of those two types of forces on the interface reads as follows:

$$(\underline{\underline{T_1}} - \underline{\underline{T_2}}) \cdot \vec{n} + \vec{\nabla}_t \gamma - \gamma \, \mathcal{C} \vec{n} = 0, \tag{2.12}$$

with $\underline{\underline{T_1}}$ [N/m^2] and $\underline{\underline{T_2}}$ [N/m^2] the total stress tensors (namely the stress tensors resulting from both surface and body forces) within the first and second bulk phases respectively, $\vec{\nabla}_t$, the components of the gradient along $\vec{t}$ (that is, within the local plane tangential to the interface) and $\mathcal{C}$ [m^{-1}], the local curvature of the interface. The first term of the equation is the expression of the forces exerted by the two media on both faces of the interfaces. The two stress tensors that make up this term result from the combined bulk effect[14]. The last two terms are manifestations of the tensile forces. These two manifestations are respectively due to a gradient of surface tension in the interface and to its curvature. They produce tangential and perpendicular stress at the interface respectively.

By separating the stress balance equation into its normal and tangential components, these normal and tangential stress equilibrium may be related to well-known effects. Under the same assumptions as those made to obtain the augmented Pascal's principle (see Eq. 2.9) (the fluid is Newtonian, still and subject to conservative forces), the normal stress balance is rewritten as the augmented Young-Laplace equation[15]. Furthermore, if we consider an interface between a liquid and air, which is considered to be a perfect dielectric and made up of non-magnetic particles, the normal stress balance reads [16]

$$P_l + P_f = P_0 + P_\gamma. \tag{2.13}$$

This equation balances the different pressures acting on the interface which are respectively the in-fluid pressure P_l, the pressure due to the

[14]To obtain these total stress tensors, the body force must be expressed in terms of their stress tensor: the Maxwell stress tensor for the electric and magnetic forces and the hydrostatic pressure for the gravity force.

[15]Named after Pierre-Simon de Laplace (1749–1827), a French mathematician, astronomer, and physicist and Thomas Young (1773–1829), an English physician, physicist and Egyptologist [23, 24, 18].

body forces acting on the fluid P_f, the atmospheric pressure P_0 [N/m^2] and the Laplace pressure $P_\gamma = \gamma\, \mathcal{C}$ [N/m^2]. When no force other than gravity is applied to a still liquid, the normal stress equilibrium is simply the Young-Laplace equation $P_l = P_0 + P_\gamma$, as there is no mass associated with the interface. In this case, the pressure jump across the interface is only due to the curvature of the latter. This is no longer true when other body forces, such as electric or magnetic forces, are applied to the liquid. Indeed, these body forces induce additional pressures P_f due to effects taking place directly inside the liquid or on the interface. These pressures and the deformations they induce are the main focus of this thesis.

Beside the normal stress balance, the stress balances in the other two directions inside the plan tangential to the interface give the shear stress balances. On the one hand, for a Newtonian fluid, with a constant surface tension γ along the interface, the tangential stress balance requires simply the shear stress to be continuous across the interface which reads as follows [16]

$$\eta_1 \frac{\partial u_{t,1}}{\partial n} = \eta_2 \frac{\partial u_{t,2}}{\partial n}, \tag{2.14}$$

with $u_{t,1}$ and $u_{t,2}$, the tangential components of the velocity along the tangent vector. If we consider an interface between a liquid and air, with $\eta_{air} \ll \eta_l$, these conditions become $\frac{\partial u_{t,l}}{\partial n} \approx 0$, which is known as the zero shear stress condition. On the other hand, a surface tension variation along the interface (expressed by a $\vec{\nabla}_t \gamma \neq 0$) induces a stress tangentially at this interface. A gradient of surface tension can generally be observed through a variation in temperature or surfactant molecules concentration. This mechanism is essential to the bubble life (see Appendix C.2 for further explanation) and even limits their maximum height [6]. Whatever the origin of the gradient, the induced stress always generates a flow of liquid from areas with low surface tension to areas with high surface tension. This effect is known as the Marangoni effect[16]. The stress induced by a surface tension gradient can also lead to buoyancy-like phenomena in a liquid film, as prettily illustrated by

[16]Named after Carlo Giuseppe Matteo Marangoni, a nineteenth century Italian physicist [11].

the rise of a hair ring in a soap film [25]. This is achieved by puncturing the soap film inside the hair curl, forcing the hair curl into a ring shape which then starts to rise due to the surface tension gradient. It should be noted that the ring shape adopted by the hair curl is a manifestation of the surface tension forces inside the soap film that pulls the hair along its circumference.

The equations of motion and the boundary conditions developed here depend both explicitly on the liquid properties which are, in the case of a Newtonian fluid, its viscosity η and its density ρ. Moreover, the conditions at the interface are intrinsically linked to the interface properties, which is characterised by a surface tension γ. Unlike η and ρ, γ is due to the assumed constitutive properties of the interface and is therefore extremely sensitive to any modification or contamination of this interface, as Agnes Pockels (1862-1935), a German chemist and physicist, noted very early on in a letter she addressed to Lord Rayleigh [26] and as she proved further in her subsequent works [27, 28]. Furthermore, surface tension is the macroscopic effect resulting from the microscopic interaction between the liquid particles and those of the external medium at the interface. Indeed, inside the liquid volume, the forces acting on a liquid particle by the surrounding ones are equally strong in all directions because of the isotropy of the fluid. However, at the interface between the fluid and the external medium, this isotropy is no longer respected and a net tension appears along the interface, inducing the interface particular properties. This tension arises from the interplay between close range repulsive interactions and long range attractive forces [29]. A sketch of the situation, based on the surface tension model proposed by Marchand *et al.* [29], is drawn in Fig. 2.1. The resulting microscopic interactions are attractive and lead to a macroscopic tensile force γ inside the interface.

This interfacial tension means that any extension of the interface is necessarily against the interaction of the fluid particles, meaning that, without external influence, a fluid always seeks to minimise its surface area. Consequently, any deformation of the interface must be fuelled with energy[17] and the surface tension can be redefined in terms of this

[17]The Young-Laplace equation (see Eq. 2.13 when no other force than gravity is present) can be re-obtained by minimising the virtual works associated with the surface

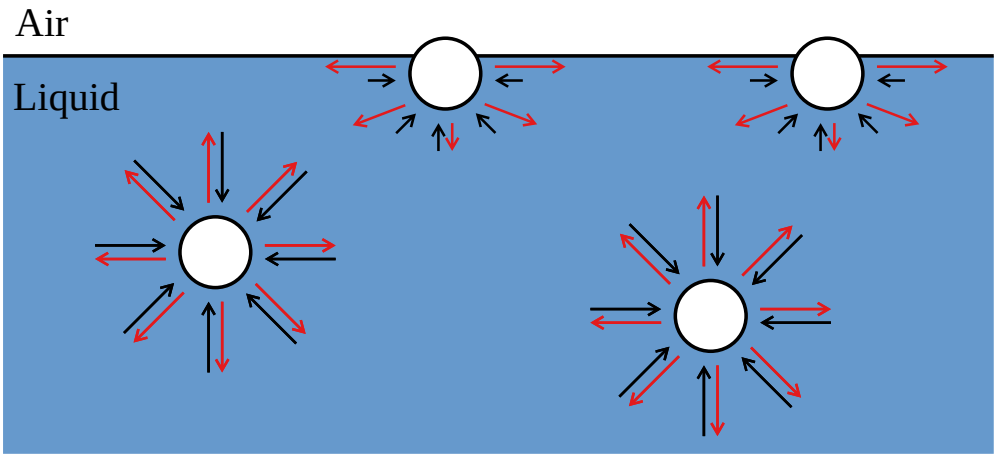

Figure 2.1: Sketch based on the surface tension model proposed by Marchand *et al.* [29], illustrating the microscopic origin of the surface tension. Surface tension arises from the combination of two effects: a close range isotropic repulsive interaction (black arrows) and a long range attraction (red arrows) which is strongly anisotropic near the interface. This results in an attractive interaction between the surface molecules, which ultimately leads to the macroscopic surface tension γ.

energy γ [J/m^2]. In nature, the surface minimisation is manifested by the ability of a droplet to form a perfect sphere or by the capacity of water striders to "walk" on water. Moreover, as a bubble consists of a thin liquid shell enclosed by two interfaces, the surface tension also greatly influences its shape, causing bubbles to naturally form a sphere. These interfacial properties are therefore of primary importance in this thesis.

2.3 Perturbations at the Interface and Waves

Thanks to the different equations describing the fluid motions and the boundary conditions, the effect of volume and surface forces can be

and volume energies, see Ref [30, 21] for the complete calculation.

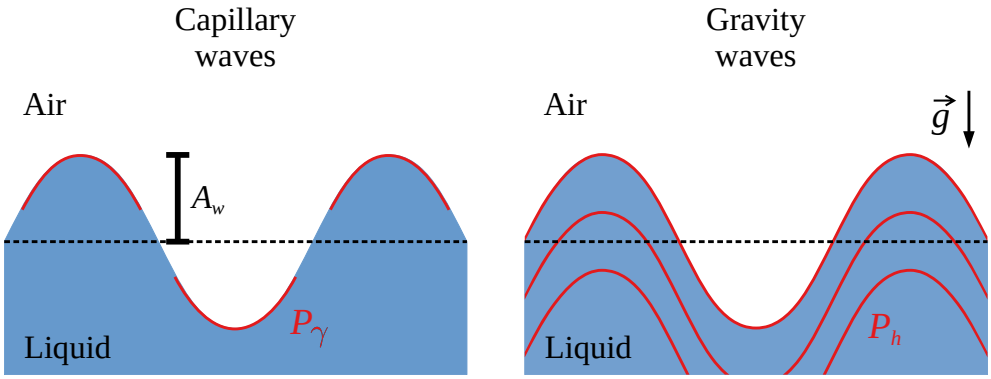

Figure 2.2: Drawings of the two mechanisms inducing the waves suppression. The isobaric lines are represented in red and the waves amplitude A_w as well as the gravitational acceleration $\vec{g}$ are in black. On the left-hand side, the surface tension seeks to minimise the interface area and induces a pressure P_γ at the curved interface. On the right-hand side, gravity tends to soften the variations of height thanks to the hydrostatic pressure P_h which increases with the liquid depth.

illustrated in a concrete situation: the waves at the seas and oceans surface. From our daily experience, we know that a free surface of liquid in equilibrium and submitted solely to gravity is flat. Since there is no curvature, by combining the Eq. 2.9 and 2.13, the pressure at any point in the liquid P_f is simply given by

$$P_f = P_0 - \rho g z, \tag{2.15}$$

with z [m] the liquid depth and $P_h = \rho g z$ [N/m^2] the hydrostatic pressure. If an external perturbation is imparted to the liquid, it moves and its surface deforms from its equilibrium shape. The perturbation propagates across the whole liquid surface, forming waves. Both the variation in height and the curvature of the interface induce a pressure that tends to bring back the surface to its equilibrium shape. The height of the

surface ξ [m] undergoing waves can be expressed as follows[18]

$$\xi(x,t) = A_w e^{kx-\omega t}, \tag{2.16}$$

where A_w [m] represents the amplitude of the wave, k [m^{-1}] the wavenumber and ω [s^{-1}] the angular frequency. If the fluid is inviscid and if $A_w \ll \lambda$, namely if the amplitude of the perturbation is small compared to its wavelength $\lambda = 2\pi/k$ [m], the only two mechanisms which induce the interfaces motion are the capillary pressure P_γ and the hydrostatic pressure P_h. Surface tension, for its part, flattens the interface because it decreases the interface area. Gravity, in turn, suppresses the waves through hydrostatic pressure. These two flattening mechanisms are presented in Fig. 2.2 and relate the wavenumber to the angular frequency by a dispersion relation[19]:

$$\omega^2 = gk + \frac{\gamma}{\rho}k^3. \tag{2.17}$$

The first right-hand term represents the gravity waves, while the second one stands for capillary waves. For small k and ω values, that is to say large and slowly oscillating waves, gravity dominates, while in the opposite limit the ripples are driven by capillarity. The transition between those two regimes occurs when both terms are equivalent:

$$k_{g,c} = \sqrt{\frac{\rho g}{\gamma}} = \frac{1}{\kappa^{-1}}, \tag{2.18}$$

with $k_{g,c}$ [m^{-1}], the critical wavenumber and κ^{-1} [m] the capillary length, a characteristic length symbolising the transition between gravity-driven and capillary-driven phenomena (for an explanation of its origin, see Appendix A). If the liquid object (in this case, the wave) has a typical size larger than the capillary length, it is dominated by gravity. Otherwise, capillarity drives its evolution. The frequency at which the transition

[18] Note that this description generalises to three dimensions, but this does not provide any additional understanding of the physics of the problem.

[19] See the sections 12 (pages 36-39) and 61 (pages 237-240) of Ref [31] for a full description of capillary and gravity waves and the associated dispersion relation.

occurs $f_{g,c}$ [s^{-1}] is obtained directly from 2.17:

$$f_{g,c} = \frac{1}{\sqrt{2}\pi}\left(\frac{\rho}{\gamma}\right)^{1/4} g^{3/4}. \tag{2.19}$$

This frequency is weakly modified by the intrinsic properties of the fluid. Comparatively, it can be changed more effectively by varying the gravity field. The apparent gravity can indeed be increased thanks to a centrifuge [32] or reduced to almost nothing in parabolic flies [33] or in the international space station [34].

The capillary and hydrostatic pressures, responsible for the waves dynamics and the dispersion relation, are respectively a surface effect and a volume effect. Yet, they both stabilise the interface by suppressing the perturbations. Other body forces, however, can have the opposite effect, destabilising the interface.

2.3.1 Influence of an Electric Field on Liquids

Applying another body force on a liquid pool, whose surface is deformed by a wave, modify the dispersion relation and the liquid dynamics due to the additional pressure. An electric field can apply such body force to a liquid, as the English scientist and physician William Gilbert early records. In his book *De Magnete*[20], published in 1600, he mentions that what he calls an electric (in more contemporary terms: a dielectric charged thanks to the triboelectric effect) attracts the nearest part of a water droplet towards itself, deforming it into a cone [35]. However, it was not until more than 300 years later that Taylor explained the conical shape adopted by the droplet [36]. It is in his honour that this phenomenon was named the Taylor cone. This first observation by William Gilbert marked the beginning of the scientific interest in the coupling between electric field and hydrodynamics, namely the electrohydrodynamics.

In a review on the role of interfacial shear stresses, Melcher and Taylor [37] highlight that the behaviour of a liquid under an electric field

[20]The original full title in Latin is *De Magnete, Magneticisque Corporibus, et de Magno Magnete Tellure* which can be translated as: "On the Magnet and Magnetic Bodies, and on That Great Magnet the Earth".

is prescribed by the relaxation time of the free charges present inside its bulk. This electric relaxation time can be expressed as $\tau_e = \varepsilon/\sigma$ [s], with ε [F/m] and σ [S/m] respectively the permittivity and the conductivity of the liquid. If the characteristic time of the experiment is much longer than τ_e, the liquid can be considered a perfect conductor, so that the interface undergoes no tangential electric stress and the electric surface force acts perpendicular to the interface. In the opposite case, when the characteristic time of the experiment is much shorter than τ_e, the fluid can be seen as a perfect insulator, with no free charges, but still with an electric surface force acting perpendicular to the interface.

Water, for instance, can be considered a perfect conductor if the characteristic time of the experiment is much greater than $1.29\ 10^{-4}$ s. Indeed, $\sigma > 5.5\ 10^{-6}$S/m and $\varepsilon \approx 80\ \varepsilon_0$, with $\varepsilon_0 \approx 8.85\ 10^{-12}$F/m the permittivity of free space, give us a characteristic electric relaxation time $\tau_{e,l} < 1.29\ 10^{-4}$ s, for water. In addition, air can be seen as a perfect dielectric if the characteristic time of the experiment is less than $\tau_{e,g} \sim 10^3$ s ($\sigma_g \sim 8\ 10^{-15}$S/m [38] and $\varepsilon_g \approx \varepsilon_0$). So, in the case an water/air interface, water can be considered a perfect conductor, while air is a perfect insulator.

In another article, Taylor *et al.* [39] studied how the presence of a uniform electric field $\vec{E}_0$ perpendicular to the interface between an inviscid conducting liquid and an insulating fluid influences the waves formed at this interface. The conducting liquid is also considered to have a sufficient thickness to neglect its influence (namely the liquid total depth is much bigger than its wavelength). They observe three main effects of the field on the conducting liquid. Firstly, they find that the liquid level rises due to the free charges' attraction. Secondly, the wave dispersion relation is modified by the effect of a surface electric pressure $P_e = \frac{\varepsilon_0}{2} E_n^2$ [N/m^2], with E_n [V/m] the component of the electric field normal to the liquid surface. Finally, a sufficiently strong electric field can lead to the destabilisation of this interface. The critical field intensity $E_{0,c}$ [V/m] naturally appears in the dispersion relation and can be calculated in a very similar way to that used to calculate the relation

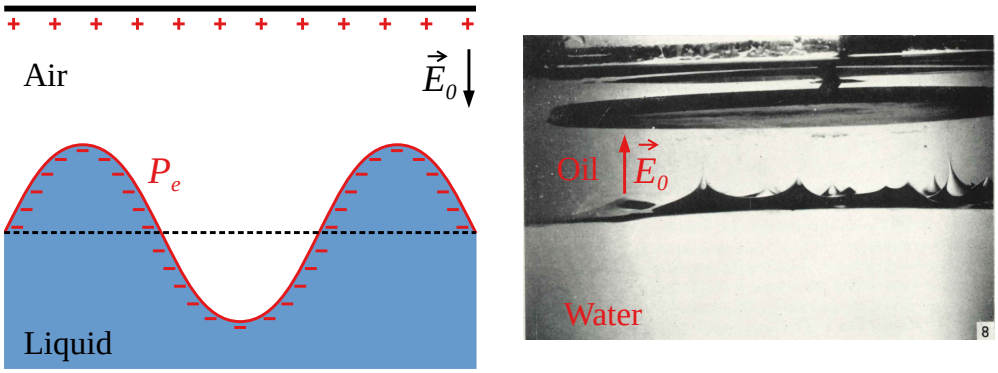

Figure 2.3: The left-hand side is a drawing of the effect of the electric field on the air/water interface. Due to the free charges, it adds an electric pressure P_e (in red) enhancing the destabilisation. The electric field $\vec{E}_0$, induced by a plane capacitor, is represented in black. The right-hand side is an original picture taken from Taylor's article [39] ($E_0 = 0.7$ kV/mm). It represents the destabilisation of an oil/water interface. The electric field as well as the liquid nature have been added in red.

without electric field[21]. The obtained relation reads as follows

$$\omega^2 = gk + \frac{\gamma}{\rho}k^3 - \frac{\varepsilon_0}{\rho}E_0^2 k^2. \tag{2.20}$$

The negative term represents the effect of the electric pressure. Unlike gravity and capillarity, the electric field tends to enhance the interface destabilisation. The effect of this term is illustrated in the left-hand side of Fig. 2.3. The critical field can be found by looking at which field at least one value of k leads to a negative value of ω^2. The critical field intensity $E_{0,c}$ obtained in this way is written

$$E_{0,c}^2 = \frac{1}{\varepsilon_0}\sqrt{4\gamma\rho g}, \tag{2.21}$$

which gives $E_{0,c} \sim 2.5$ kV/mm for an air/water interface.

[21] See the fifth exercise in the fifth section of Ref. [40] (page 33) for a full resolution.

When $E_0 > E_{0,c}$, the interface destabilises. This leads to the situation illustrated in the right-hand side of Fig. 2.3. This picture is one of those taken by Taylor in his article [39], in the case of an oil/water interface. They used oil instead of air because they observed that sparks occur directly after the instability is triggered, disrupting its development. Since the dielectric constant of oil is more than twice that of air, using it instead of air circumvents this difficulty.

If $E_0 > E_{0,c}$, the interface is stable for all k. However, the dispersion relation is modified by the presence of the field and this can be observed by taking pictures of the wavy interface. We performed the experiment on salt water by disturbing the interface at a given frequency thanks to a shaker. The shaker is connected to a plastic plate immersed in the water which oscillates up and down, imposing a standing wave on the water surface. A circular aluminium plate (of 70 mm radius) connected to a generator is placed over the interface, which is grounded, as shown on the left-hand side of Fig. 2.3. This allows us to apply a uniform electric field $\vec{E_0}$ between the top plate and the interface (it should be noted that the presence of the wavy interface changes the local value of the electric field although the applied one is uniform). By varying the oscillation frequency and measuring the distance between successive crests, the dispersion relation can be reconstructed experimentally on both regimes.

The result of these measurements is shown in Fig. 2.4, with an imposed electric field $E_0 = 1$ kV/mm in green and without electric field in blue. No error bars from the pixel detection are shown because they are smaller than the bullets. Those preliminary results clearly evidence an effect of the electric field on the dispersion relation, namely a decrease of ω at a given k. The blue line is adjusted using Eq. 2.17. The gravitational and capillary prefactors obtained from this adjustment are used to fit Eq. 2.20, leaving only the electric prefactor free. The resulting fit is represented by the green line. Those qualitative results were recently confirmed by Apffel *et al.* [41] who also used the electric field-induced modification on the medium to create a temporal interface.

Néron de Surgy *et al.* [42] generalised the results obtained on the dispersion relation and the destabilisation of the interface to any fluid thickness or viscosity. For their part, Onuki [43] and Schäffer *et al.*

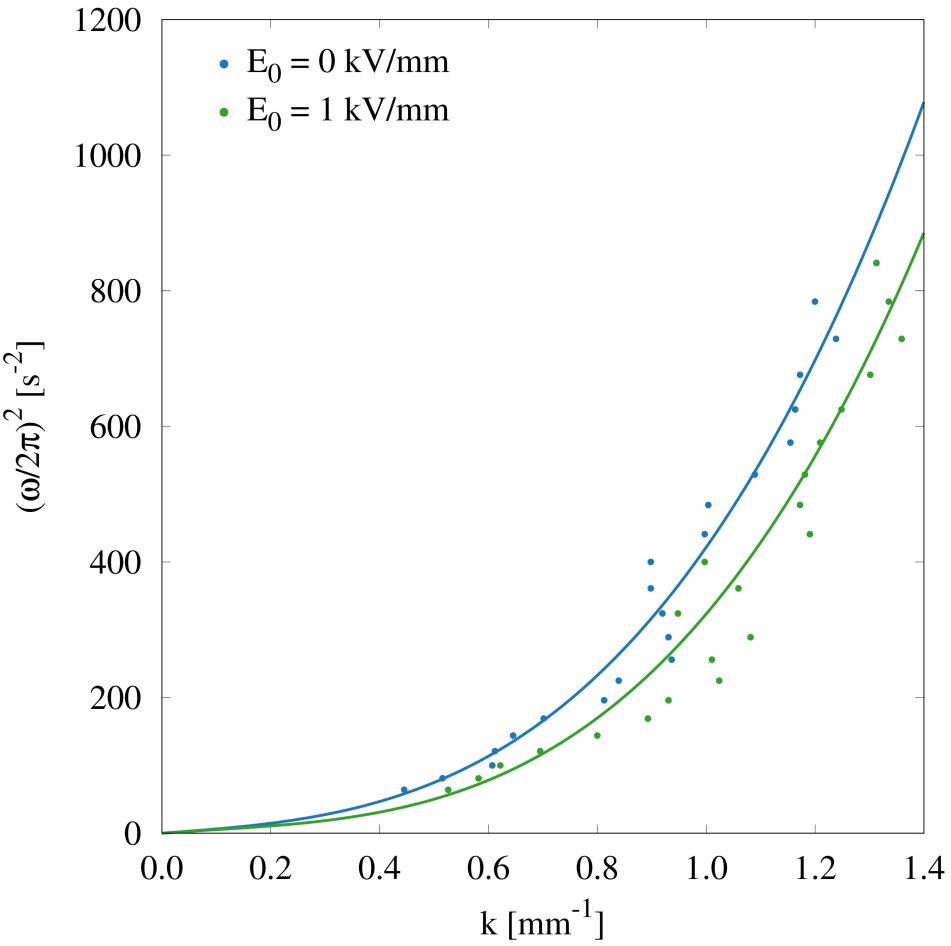

Figure 2.4: Pulsation ω of the wave as a function of the measured wavenumber k. In blue, the measured dispersion relation when no electric field is applied. In green, the water suffers a uniform electric field $E_0 = 1$ kV/mm generated by a plane capacitor. The dispersion relation is thus modified. The blue line is an adjustment of the Law 2.17. The green one is obtained by adjusting the Law 2.20, the electric prefactor being the only fitting parameter and the two others being fixed by the first adjustment.

[44, 45] studied the case of an interface between two insulating fluids. Furthermore, the limiting case of a thin liquid film submitted to a perpendicular electric field was studied numerically by Firouznia *et al.* [46] who showed that the two interfaces enclosing the film can be deformed in-phase or anti-phase. Finally, the effect of the field frequency on the interface stability has also been studied [47, 48, 49] and the authors show that the critical destabilisation field is always smaller when the electric field oscillates.

Due to the applied electric field and the associated pressure induced on the interface, the waves dynamics and the associated deformation are modified. In contrast to capillary and hydrostatic pressures, the electric pressure enhance the deformation of the interface due to the charges attraction. Moreover, for a sufficient electric field intensity, the interface destabilises, forming cones to discharge the charge induced by the electric field. Yet, an electric field is not the only kind of field that modifies the waves dynamics.

2.3.2 Influence of a Magnetic Field on Liquids

The interplay between liquid and magnetic field is a relatively recent topic. This is indubitably because most of "common" liquids, such as water, have a very weak response to magnetic fields. When such diamagnetic liquids are subjected to a magnetic field, Lorentz forces are induced on their constitutive particles. A very weak magnetic dipole emerges from these forces, which is directed at the opposite direction of the magnetic field. By using a very intense magnetic field $\vec{B}_0$, it is possible to observe a macroscopic repulsive effect and make a living frog fly for example [50] ($B_0 = 16$ T). This phenomenon can also be used to move droplets, or even bubbles, over a textured surface filled with lubricating liquid, also known as a slippery liquid-infused porous surface or SLIPS [51]. Another way to obtain a response of a fluid to a magnetic field is to apply an electric current in the fluid. The Lorentz force arising from the current and the magnetic field induces a volume force on the conducting fluid. The study of this coupling between hydrodynamics, current passing through the conducting liquid and magnetism is called magnetohydrodynamics.

To probe the effect of the magnetic dipoles' alignment in fluids, a fluid actually consisting of particles bearing a magnetic moment $\vec{m}$ $[\mathrm{Am}^2]$ is needed. Yet, no natural fluid seems to have this characteristic[22] and therefore an artificial one must be synthesised. This was achieved by Papell in 1965 [55] and further developed shortly thereafter by Rosensweig *et al.* [56]. These fluids are called ferrofluids and the study of their properties is named ferrohydrodynamics. They are colloidal dispersions and, in our case, the colloidal particles are maghemite ($\gamma-\mathrm{Fe_2O_3}$), which are ferrimagnetic monodomains. The solution is stabilised by negative electrostatic charges at the surface of each particle, preventing their agglomeration and subsequent sedimentation [57]. As maghemite particles have a typical diameter of 10 nm, the Navier-Stokes equations 2.4 (and those derived from them) are suitable for describing the flow of such a fluid as long as this flow is not micrometric or smaller.

It should be noted that the very name ferrofluid is a little odd. Indeed, ferrofluid does not bear a permanent magnetisation, as ferromagnetic materials do, but acquires one when subjected to a magnetic field. The induced magnetic moment is parallel to the applied magnetic field (unlike diamagnetic fluids), has an intensity similar to that found in ferromagnetic materials[23] and vanishes almost instantaneously when the magnetic field is switched off. This behaviour characterises paramagnetic fluids, but as the magnitude of the induced magnetic moment is much larger than that typically found in paramagnetic materials (10^2 to 10^5 times larger), ferrofluids are considered superparamagnetic fluids[24]. One of the most striking illustrations of the behaviour of a ferrofluid subjected to a magnetic field $\vec{B}_0$ perpendicular to its interface, is the Rosensweig instability (see the right-hand side of Fig. 2.5). This instability is characterised by the appearance of regularly spaced spikes

[22]It should be noted that a fluid made of magnetotactic bacteria [52] within their living environment can be seen as an active natural fluid whose particles bear an intrinsic magnetic moment [53]. However, such a fluid is much more complex to describe due to the living nature of bacteria and exhibits exotic behaviours [53, 54].

[23]For example, our ferrofluid has a magnetic field response of 10^5 greater than that of water.

[24]The name probably comes from the colloidal particles of which it consists, namely single-domain ferromagnetic or ferrimagnetic particles.

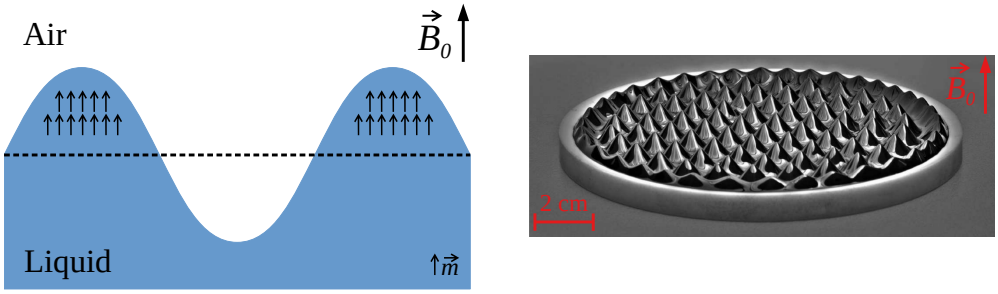

Figure 2.5: The left-hand side is a drawing of the effect of a vertical magnetic field $\vec{B}_0$ (in black) on the air/liquid interface. The vertical alignment of the magnetic moment $\vec{m}$, some of which are represented by black arrows, induces a combination of three pressures: $P_{m,s}$, $P_{m,i}$ and $P_{m,n}$. The right-hand side is a picture of a Rosensweig instability taken from [58]. For this particular ferrofluid (EMG 909 from Ferrotec Co.), they measured a critical field intensity triggering this instability $B_{0,c} = 25.7$ mT [58]. The scale and the magnetic field have been added in red.

when a layer of ferrofluid is subjected to a sufficiently high transverse non-uniform magnetic field.

In a spirit similar to the method undertaken by Taylor *et al.* [39] to determine the magnitude of the critical electric field required to destabilise an interface $\vec{E}_{0,c}$, Cowley *et al.* [59] carried out an analysis to obtain the critical magnetic field intensity $B_{0,c}$ [T] triggering the Rosensweig instability. The critical field naturally appears in the dispersion relation of waves under a constant applied magnetic field, normal to the interface at rest. This dispersion relation is modified by the three pressures due to the effect of magnetic field on the ferrofluid: the magnetostrictive pressure $P_{m,s}$ [N/m^2], the overpressure inside the fluid due to the interaction between the magnetic moments $P_{m,i}$ [N/m^2] and the normal magnetic traction at the fluid interface $P_{m,n}$ [N/m^2] [56]. Those

pressures read as follows

$$P_{m,s} = \mu_0 \int_0^{\tilde{H}} \left[\nu \frac{\partial M}{\partial \nu} \right]_{\tilde{H}^*,T} \mathrm{d}\tilde{H}^*, \tag{2.22}$$

$$P_{m,i} = \mu_0 \int_0^{\tilde{H}} M \mathrm{d}\tilde{H}^*, \tag{2.23}$$

$$P_{m,n} = \frac{\mu_0}{2} M_n^2, \tag{2.24}$$

with $\mu_0 = 4\pi\ 10^{-7}$ N/A^2 the magnetic permeability of free space, M [A/m] the magnetisation, which is the magnetic moment per unit volume, $\tilde{H}$ [A/m] the internal field related to the magnetic field B, T [] the temperature, $\nu = \rho^{-1}$ [m^3/kg] the specific volume and M_n [A/m], the normal component at the interface of the magnetisation. The calculation of the modified dispersion relation for an inviscid fluid and a fluid thickness much larger than the wavelength leads to[25]

$$\omega^2 = gk + \frac{\gamma}{\rho} k^3 - \frac{f(\chi)}{\rho \mu_0} B_0^2 k^2, \tag{2.25}$$

with $f(\chi) = \chi^2/(1+\chi)(2+\chi)$ a function of χ, the magnetic susceptibility, that is itself a function of the applied magnetic field. The modification due to such a perpendicular magnetic field on wave turbulence has been verified experimentally by Boyer *et al.* [60] and the generalisation of the modified dispersion relation to fluids of any viscosity and thickness was performed by Abou *et al.* [61].

As for the wave turbulence under an electric field, the magnetic term representing the magnetic influence due to a perpendicular magnetic field is negative, revealing that the field tends to destabilise the interface. Indeed, on the one hand, the magnetic dipoles composing the ferrofluid tend to align their magnetic moment along the imposed magnetic field, namely vertically. On the other hand, the dipole-dipole energy interaction is negative if the dipoles are aligned in the same direction as their magnetic moment. Conversely, if the dipoles alignment

[25] See the seventh section of Ref. [56] (pages 104-118) for a full calculation.

is perpendicular to their magnetic moment, the dipole-dipole energy interaction is positive[26]. Therefore, the magnetic moment tends to seek a vertical alignment and avoid a horizontal one. This is the origin of the destabilising effect which is represented on the left-hand side of Fig. 2.5.

The minimum field necessary to trigger the Rosensweig instability can thus be found in the same way as in the case of wave turbulence under electric field, leading to a critical magnetic field $B_{0,c}$:

$$B_{0,c} = \frac{\mu_0}{f(\chi)}\sqrt{4\gamma\rho g}. \tag{2.26}$$

This gives $B_{0,c} \sim 11.5$ mT for an interface between air and the ferrofluid soap used for the experiments presented in this thesis (see Appendix B for a description of the soap and see Table 3.1 for its properties). However, this instability can be inhibited by vibrating the ferrofluid as experimentally demonstrated by Pétrélis *et al.* [62]. It is interesting to note that the application of a magnetic field parallel to the plane of the interface instead of perpendicular to it reduces the deformation rather than enhancing it, as shown by Dorbolo *et al.* [63]. Indeed, as $\vec{B}_0$ is horizontal, the magnetic dipoles tend to align themselves horizontally and avoid vertical alignment.

Unlike an applied electric field to a conductor, an magnetic field applied to a ferrofluid adds pressures not only at the interface, but also within the fluid. The combined effects of these pressures modify the waves dynamics and enhance the deformation. Just as a conducting fluid under a sufficient electric field, a ferrofluid destabilises under a sufficient magnetic field by forming a Rosensweig instability.

2.4 Conclusion

The various equations of motion describing the fluid dynamics and the associated boundary conditions were presented. Particular attention has been paid to establishing the equations describing a motionless Newtonian fluid describing the shape that a steady volume of liquid, such as a

[26]The function of the dipole-dipole energy interaction is continuous with the angle between the magnetic moment and the direction of alignment. Moreover, this function is null when the angle is approximately equal to 54°.

bubble, assumes (see Eq. 2.9 and Eq. 2.13). These equations highlight the presence of a surface force, represented by the capillary pressure $P_\gamma = \gamma\ \mathcal{C}$ and three different body forces: the gravitational, electric and magnetic forces. These forces manifest themselves differently, at the interface between two different fluids or directly within them. The gravitational force induces an in-fluid pressure that directly depends on the fluid density and depth, the hydrostatic pressure $P_h = \rho g z$. Conversely, an electric force acting on a conducting liquid only induces a surface pressure depending on the applied electric field, the electric pressure $P_e = \varepsilon_0 E_n^2/2$. Finally, when a ferrofluid is submitted to a magnetic force, both surface and volume pressures appear, all function of the applied magnetic field through the magnetisation: the magnetic in-fluid pressure $P_{m,i}$ (Eq. 2.23), the magnetostrictive pressure $P_{m,s}$ (Eq. 2.22) and the magnetic surface pressure $P_{m,n}$ (Eq. 2.24).

To illustrate these forces, we have used a concrete situation consisting of waves at the surface of oceans and seas. In particular, the dispersion relations describing these waves (see Eq. 2.17 for the gravity/capillary, Eq. 2.20 for the gravity/capillary/electric and Eq. 2.25 for the gravity/capillary/magnetic) highlight the effect of the different forces. Indeed, while the capillary and gravity forces tend to suppress the interface deformation, the electric and magnetic ones tend to enhance it. As they reinforce the deformation, the electric and magnetic pressures can lead to interface instability. The critical electric and magnetic fields both naturally appear in the dispersion relation and respectively trigger the Taylor cones and the Rosensweig instability. Although these two instabilities manifest themselves in a qualitatively similar manner (namely vertical spikes emerging from the liquid), they are due to completely different phenomena. The Taylor cones are due to charges attraction and droplets emission from the tip of the cones in order to discharge, whereas the Rosensweig instability is due to dipole alignment and is not associated with any droplet emission.

These different illustrations show that body forces provide an excellent way to manipulate and reshape liquids without touching them. A droplet, for example, has a shape defined by its volume due to the competition between capillarity and gravity, but can be deformed thanks to electric or magnetic forces. The next chapter (Ch. 3) is devoted to pre-

senting the different shapes that a droplet can assume when subjected to different body forces. These shapes are due to the competition between capillarity and at least one body force and are rationalised on the basis of the equations developed in this chapter. The purpose of presenting the droplet shape is to provide a point of comparison for studying bubbles under the same conditions, as illustrated in Fig. 1.2. Indeed, droplets and bubbles are very similar from a surface point of view, but quite different from a volume one. Due to the surface and volume nature of the presented body forces, we therefore expect them to modify droplets and bubbles in similar or different ways depending on this nature. After presenting this seed point, the core of this thesis is devoted to describing how the bubbles shapes are deformed by the different body forces presented in this chapter.

3
Droplets

So far we have considered a volume of liquid so large that it forms a bath. At rest, its interface is flat due to gravity. When energy is imparted to this system, waves can be induced and if the amount of injected energy is sufficient, the liquid volume can split, forming tiny amounts of liquid called drops. Such drops are ubiquitous in nature and can form through the break up of a large amount of liquid (*e.g.* a liquid stream experiencing a Rayleigh-Plateau instability[1] [21]) or through the condensation of vapour (like dew on leaves and grass in the early morning). Furthermore, droplets can assume many shapes and undergo numerous deformations depending on their motion, size, the substrate on which they rest or the forces acting on them. However, if a droplet of a few centilitres is motionless, with absolutely no forces acting on it (as if it were free-floating inside the International Space Station, for example[2]), it would adopt a spherical shape due to capillarity and surface minimisation.

The deviation from this spherical shape is due to an external force. In this thesis, we are mainly interested in the deformation induced by different external forces, arising from gravity, electric or magnetic fields. In each case, the steady shape adopted by a droplets results from the

[1]Named after Lord John William Strutt Rayleigh (1842–1919), a British physicist who won the Nobel Prize [11] and Joseph Antoine Ferdinand Plateau (1801-1883) a Belgian physicist and mathematician [18].

[2]Visit www.youtube.com/watch?v=TLbhrMCM4_0 for an illustration.

equilibrium between at least the effect of one of these external forces and the capillarity. For example, the shape of a motionless droplet resting on a solid substrate results from the competition between gravity and surface tension, the former flattening the droplet, while the latter tends to keep it hemispherical.

The reaction of a droplet immersed in an electric field depends on the liquid of which it is made. In particular, if the liquid is a perfect conductor, all electric effects take place at the droplet surface. For a sessile conducting droplet resting on a conducting surface, the magnitude of the experienced deformation would then be obtained by balancing the capillary and electric pressures. This balance would hold as long as the effect of gravity can be neglected, resulting in an initial shape defined solely by capillarity and a deformation exclusively due to the electric constraints. In the same fashion, the maximum charge that a spherical droplet could hold before becoming unstable can be deduced from this balance.

In the case of a magnetic field, the liquid used to make the droplet also largely influences its response. For instance, ferrofluids react much more to magnetic fields than water. However, regardless of the liquid used, volume forces are always present in addition to surface ones whenever a magnetic field is applied. The deformations of such a ferrofluid droplet under a uniform magnetic field, for example suspended inside a matching density fluid, are described by the competition between the capillary and the magnetic pressure due to the dipole alignment within the magnetic field. The case of sessile droplets deformed by a permanent magnet is more complex due to the field gradient. If the magnet is held under the substrate, such a droplet can either be flattened by the combined effect of the magnetic gradient and gravity, or elongated by the magnetic field itself through dipole alignment. Both phenomena are present and the final shape of the droplet depends on both the magnetic field and the magnetic gradient values. However, whichever magnetic effect dominates, it counteracts capillarity that tends to keep the droplet spherical.

These force balances and the subsequent equilibrium shapes are conveniently described by dimensionless numbers. This chapter is dedicated to illustrating these shapes and the dimensionless numbers that charac-

terise them. Moreover, comments on the similarities and discrepancies between drops and bubbles are made to rationalise the observations presented in Fig. 1.2. More specifically, the first part of the chapter focuses on the description of the droplet shape under gravity and how this shape depends on the droplet size. Then, the influence of both the electric field and the charge on the motion and shape of the droplet is outlined. Under similar conditions, the droplet deforms in a completely different way, depending on both its permittivity and conductivity but also on those of its surrounding medium. Finally, in the last part of this chapter, the effect of a magnetic field on a ferrofluid droplet is addressed. In addition to deformation, the magnetic field may induce drop motions and divisions into daughter droplets. Furthermore, an experiment combining the effects of electric and magnetic fields is presented before a conclusion is drawn.

3.1 Sessile Droplet under a Gravity Field

Any raindrop that falls from the sky adopts a shape prescribed by its fall into the atmosphere until it hits the ground. From there, the droplet lands on a solid surface in a shape depending on its size. Indeed, while small droplets almost form a hemisphere, larger ones are flattened by gravity and tend to form puddles [30]. This behaviour is represented in Fig. 3.1. Four sessile droplets of increasing volume V_l [m^3] are presented. They rest on an aluminium plate with a base length a [m] and a height b [m]. While the small droplets adopt an almost perfect hemispherical shape (with $a/2 \approx b$), the larger ones form a puddle with no apparent relationship between a and b. This behaviour is highlighted by the chart on the right-hand part of Fig. 3.1 representing the typical height of a droplet as a function of its volume. Smaller droplets, hemispherical in shape, see their height scaling as the cube root of their volume, while larger ones reach a saturation height.

This shape can be described by the Bernoulli equation and the normal stresses balance at the liquid/air interface:

$$P_l + \frac{1}{2}\rho u^2 + \rho g z = \text{cst}, \tag{3.1}$$

$$P_l = P_0 + P_\gamma, \tag{3.2}$$

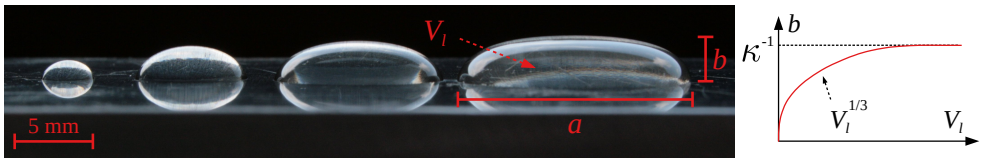

Figure 3.1: Pictures of four water droplets resting on an aluminium plate with the typical scale shown at the bottom left. The volume of water V_l, and thus the size of the droplet, is increased to illustrate the growing effect of gravity leading to a transition in shape. The typical size, defined as the base length a, ranges from 4 mm for the smallest droplet, which forms an almost perfect hemisphere, to 17 mm for the largest, which tends to form a puddle. The maximum height b saturates for the larger droplets causing a "plateau" to appear. To highlight this effect, a typical graph of b as a function of V_l is presented on the right-hand side of the figure. Initially, the height increases as the cube root of the volume (as predicted for a hemisphere) and eventually saturates at the capillary length κ^{-1} for larger volumes.

with P_l the pressure inside the liquid, ρ its density, u its speed, g the intensity of the gravitational field, P_0 the atmospheric pressure and $P_\gamma = 2\gamma/r$, the Laplace pressure for a spherical droplet of radius r [m] and surface tension γ. When the liquid droplet is at rest, its shape is described by the competition between gravity and capillarity. More precisely, gravity prescribes the shape of the larger droplets and surface tension defines the shape of the smaller ones (for more details, see Appendix A). The transition between these regimes occurs for a droplet with a characteristic size close to κ^{-1}, the capillary length, defined by the ratio between the two effects:

$$\kappa^{-1} = \sqrt{\frac{\gamma}{\rho g}}. \tag{3.3}$$

This characteristic length is linked to the famous Newton-Bond number

Liquid	γ [mN/m]	ρ [kg/m^3]	κ^{-1} [mm]	
Water	72 [30]	1 10^3	2.5	
Mercury	485 [30]	13.6 10^3 [64]	2	
Silicone oil	20 [21]	0.97 10^3	1.5	
Denkov's soap	21.6 [14]	1.03 10^3 [14]	1.5	Ch. 6
Ferrofluid soap	30 [65]	1.5 10^3 [65]	1.5	Ch. 7

Table 3.1: Typical values of surface tension γ, density ρ and capillary length κ^{-1} at room temperature of some common fluids as well as those used in this thesis. Denkov's soap is a surfactants mixture based on the stock solution formulated by Denkov *et al.* [66] (see Appendix B for more details) which is used to study the deformation of soap bubbles under electric field. Finally, ferrofluid soap is also a surfactant solution based on the one proposed by Elias *et al.* [65] (see also Appendix B for more details) and used to study the deformation of soap bubbles under magnetic field.

(or simply Bond number) Bo $= \rho g r^2/\gamma$ [67][3][4], which balances the capillary and hydrostatic pressures. Droplets with a characteristic length smaller than κ^{-1} tend to form a hemisphere (surface tension prevails), whereas drops with a characteristic length larger than κ^{-1} tend to form a puddle under gravity. As a numerical example, water exhibits $\kappa^{-1} \approx 2.5$ mm. Therefore, water droplets of volume V_l take on a hemispherical shape if $r = \sqrt[3]{3V_l/2\pi} \ll \kappa^{-1}$ and a puddle shape if $r \gg \kappa^{-1}$ (which is consistent with the observations reported in Fig. 3.1). Typical values of surface tension γ, density ρ and capillary length κ^{-1} for usual fluids as well as for the soaps used in this thesis are given in Table 3.1. The surface tension is given assuming an air/liquid interface. Further explanations about the origin of the capillary length, as well as the influence of the substrate, are given in Appendix A.

[3]Named after Wilfrid Noel Bond (1897–1937), an English physicist and engineer [11] and Dorothy A. Newton, his co-author [67] about whom little is known.

[4]This dimensionless number could just as easily be called Eötvös number, after Lóránd Baron von Eötvös (1848-1919), a Hungarian physicist [11], or Newton number.

3.2 Droplets Under an Electric Fields

When charges are transferred to droplets, their motion are no longer solely determined by the gravity field but also by the electric one. This situation occurs in many natural phenomena. For example, in the early days of climatology, Benjamin Franklin suggested that rain may be due to the attraction of oppositely charged droplets [68]. Moreover, numerous studies underline the central role of charged droplets in the establishment of strong electric fields in thunderstorms [68, 69, 70] or in the creation of preferential paths for lightning strikes [71, 72]. One of the first experimental observations of the influence of an electric field on the droplet displacements was performed by Lord Rayleigh [73] who applied a moderate electric field to droplets from a jet after it had separated due to a Rayleigh-Plateau instability. He observed that in the absence of an electric field, uncharged droplets bounce off each other, but noted that charged droplets attract each other and eventually coalesce, resulting in a jet that is no longer scattered (see [4] pages 53-57 for a wonderful illustration of this phenomenon). Later, these early observations were complemented by systematic studies about droplet collisions. These works showed that bouncing is only one of the possible interactions between two uncharged water drops as they collide [74, 75]. More recently, Brandenbourger *et al.* [76] have analysed the effect of electric charges on the collisions and trajectories of drops in a microgravity environment. They observed that oppositely charged drops attract each other, possibly preventing them from bouncing, while drops with the same sign of charge repel each other and are therefore less likely to collide.

When charged (see [77] for a clever way to do it) millimetric droplets can also be transported and manipulated precisely by means of an electric field. Among others, Brandenbourger *et al.* [78] proposed to use an horizontal electric field to control the motion of a charged silicone oil droplet bouncing on a vertically vibrating bath. This method allows the droplet to be manipulated while avoiding any contact with the substrate by regenerating the air layer that separates them. This absence of contact between the bath and the droplet is advantageous as it greatly reduces the risk of altering the droplet contents while preserving the possibility of directing the droplet's trajectory.

Beside their ability to move droplets, as already mentioned, electric fields can also directly influence their shape. Indeed, when an object (whether initially charged or not) is subjected to an electric field, its positive charges move in the electric field direction, while negative ones go in the opposite way. This separation induces an internal field, called polarisation, tending to cancel the original field. When the charges are bound, this cancellation is partial, as in dielectrics. Conversely, in perfect conductors, charges are free and, consequently, the polarisation field completely cancels the external electric field, leading to a zero field inside the drop. For such conducting droplets, all charges are at the interface, there is no electric volume force and electric effects occur only at the fluid surface. Therefore, the stable shape of a conducting droplet is fully determined by the Bernoulli equation (see Eq. 3.1 with the speed pressure term being null) and the balance of stresses normal to the surface that are defined by the following formulæ[5]:

$$P_l + \rho g z = \text{cst}, \tag{3.4}$$

$$P_l + \frac{\varepsilon_0}{2} E_n^2 = P_0 + P_\gamma. \tag{3.5}$$

The second term of Eq.3.5 is called the electric pressure P_e and is due to the surface charges resulting in a surface electric field E_n perpendicular to the surface. Once established, this field acts on the surrounding surface charges, inducing the electric pressure $P_e = \varepsilon_0 E_n^2/2$ [79]. Considering Eq. 3.5, the capillary pressure and the electric one are the two key ingredients to determine the shape of such a droplet. Moreover, from a surface point of view, droplets and bubbles are very similar and since both acting elements take place at the surface, the reaction induced by an electric field on droplets and bubbles should be very similar. As they have already been extensively studied, charged droplets are therefore a good starting point to apprehend charged bubbles and, through their possible differences, to probe which bubbles peculiarities are essential to describe their dynamics under electric fields.

The influence of the electric field on the shape of a conducting droplet floating within a dielectric medium was also illustrated by Lord Rayleigh,

[5]Assuming that the external medium has a permittivity close to that of vacuum.

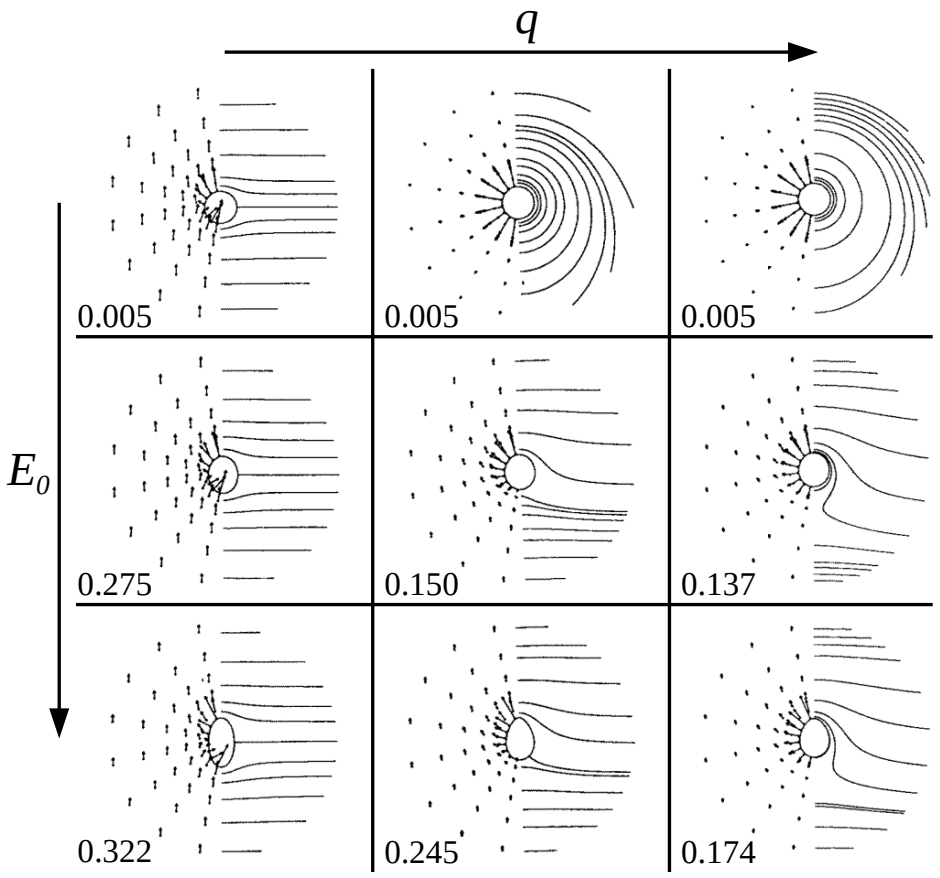

Figure 3.2: Drawings of conducting drops under a vertical electric field pointing upward. The electric field is represented on the left-hand side of each drawing, while the equipotentials are shown on the right-hand side. On the one hand, each column represents a droplet with a different carried charge. From left to right: $\tilde{q} = 0$, $\tilde{q} = 8$ and $\tilde{q} = 12$, with $\tilde{q} = q/\sqrt{2\varepsilon_0\gamma r_0^2}$, the dimensionless charge. On the other hand, each row shows the state of the droplet when the applied field E_0 increases. From top to bottom: stable droplet with an almost zero field, stable droplet under a moderate field, droplet at its stability limit. The value of the dimensionless applied field, namely the square root of $\mathrm{Bo}_{e,d}$, is indicated at the bottom left of each drawing. Each drawing is taken from [80] and has been edited.

who calculated the maximum charge that an initially spherical droplet can hold [81]. He showed that the droplet destabilisation is related to a dimensionless number, which he called the fission ratio,

$$\mathrm{X} = \frac{q^2}{64\pi^2\varepsilon_0\gamma r^3} \tag{3.6}$$

with the carried charge q [C] and the droplet radius r. This dimensionless number results from the balance between the two pressures at the surface of the charged droplet: the electric one, $P_e = q^2/(64\pi^2\varepsilon_0 r^4)$, and the capillary one, $P_\gamma = 2\gamma/r$. Indeed, while the electric pressure elongates the droplet due to charges repulsion, the capillary pressure holds it in a spherical shape. When $\mathrm{X} < 1$, the capillary pressure is higher than the electric one and the droplet has a stable spherical shape. If $\mathrm{X} \geqslant 1$, the electric pressure overpasses the capillary one and the droplet becomes unstable, deforms into a spheroid and emits thin charged jets along its major axis. This phenomenon was confirmed experimentally by Duft *et al.* [82, 83].

Basaran *et al.* used a numerical approach to further study the shape of a charged droplet with [80] and without [84] an electric field. They also predicted the stability of these shapes thanks to the bifurcation theory [85]. In particular, they found that the deformation of a charged droplet into an oblate spheroid is stable beyond the Rayleigh limit in the absence of an electric field [84]. In contrast, when immersed into an electric field, the charged droplet loses its equatorial symmetry and adopts an egg shape with the egg tip pointing in the direction of the electric field [80] (see Fig. 3.2). In another article, Wagoner *et al.* [86] numerically studied the shape and stability of a droplet subjected to a uniform electric field and having a lower conductivity and permittivity than the surrounding fluid. Depending on the viscosity ratio between the droplet and the surrounding fluid, the authors found two types of shapes adopted by an initially spherical droplet when the electric field intensity increases: dimples and lenses (see Fig. 3.3). They observed that lens shaped drops (prettily called "Saturnian droplet" by Marin [87], see Fig. 3.3 (c)) can undergo an instability similar to the Taylor cone (but involving completely different mechanisms): the equatorial streaming, already experimentally observed by Brosseau *et al.* [88].

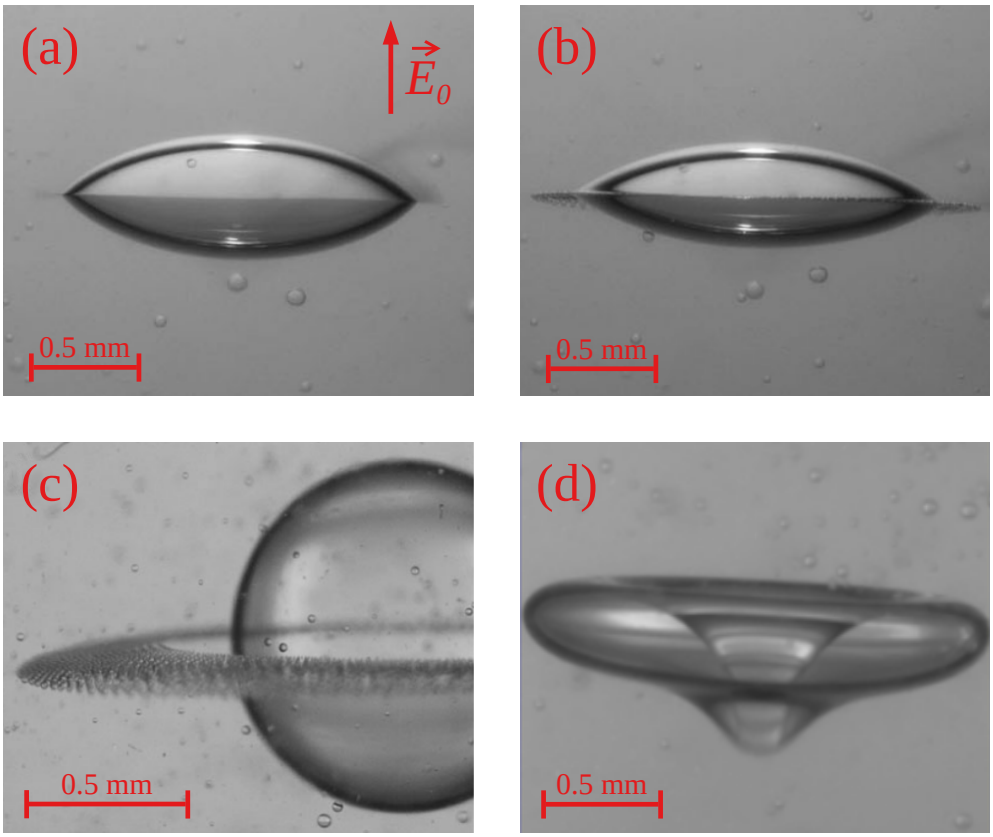

Figure 3.3: Pictures of drops made of a liquid having a lower conductivity than the surrounding medium under a vertical applied electric field $\vec{E}_0$. Depending on the viscosity ratio between the droplet and the surrounding medium η_{in}/η_{ext}, the droplet can adopt two different shapes: a lens if $\eta_{in}/\eta_{ext} < 0.1$ and a dimple otherwise. (a-b) Images of a droplet having a viscosity lower than that of the surrounding medium under an electric field $E_0 = 790$ V/mm. The droplet took the shape of a lens 0.5 s after the electric field was turned on, and 0.2 s later, starts to emit tiny droplets from its rim. (c) Saturnian droplet ($\eta_{in}/\eta_{ext} < 0.1$) obtained by applying a short electric pulse of $E_0 > 300$ V/mm. (d) Dimple of the droplet whose viscosity is higher than that of the surrounding medium after the application of a field $E_0 > 300$ V/mm. The pictures come from [88] and have been edited.

These deformations of droplets by the application of an electric field (or even their disintegration, if the critical field is reached) are used in multiphasic systems to enhance the mass and heat transfer rates between phases. Indeed, in such a system, consisting of a dielectric continuous liquid phase and a dispersed one made up of conducting liquid droplets, both transfer rates are proportional to the interfacial area [89]. Therefore, the use of an electric field to deform (or even disintegrate) the dispersed phase can serve to increase this area and hence both transfer rates [89]. Similarly, an increase in interfacial area is also observed when an electric field is applied to a multiphasic system with a dispersed phase made of gas bubbles [89, 90].

When resting or suspended on a substrate, the shape of the droplet is affected, as is its response to electric charges. In order to make an informed comparison with sessile or floating bubbles, the effect of the substrate must be explored. The case of a droplet hanging at the tip of a liquid-filled tube charged upon the application of a high voltage was first studied by Zeleny [91, 92, 93]. When electric charges are imparted to a droplet, it deforms from a hemispherical to a hemi-spheroidal shape. Above a critical threshold, instability is triggered and the subsequent emission of microscopic liquid jets is observed. This phenomenon is known as electrospray [93]. Later, Taylor [36] found that the spheroidal approximation remains valid only at the early stage of the deformation. Just before the instability, he observed that the shape of the droplet is close to a cone. This led him to deduce a new stability law [36]. Thanks to this discovery, the instability is still known as the Taylor's cone. Both the Taylor's cone and the resulting electrospray (or electrospinning) have been studied for their ability to generate micrometric droplets of controlled size, ionised mists [94, 95, 96] and nanofibres [97]. The large amount of applications ranges from high-resolution printing [98] to space propulsion [99] via droplets encapsulation [100], wound healing [101] or even chocolate processing for the food industry [102]. The use of electrospray in mass spectrometry of large macromolecules even led Fenn [103] to the 2002 Nobel Prize in Chemistry.

In his article on the stability of a charged sessile droplet, Taylor also proposed a stability limit for a closely related system: an initially uncharged sessile (or pendant) droplet under an electric field. This con-

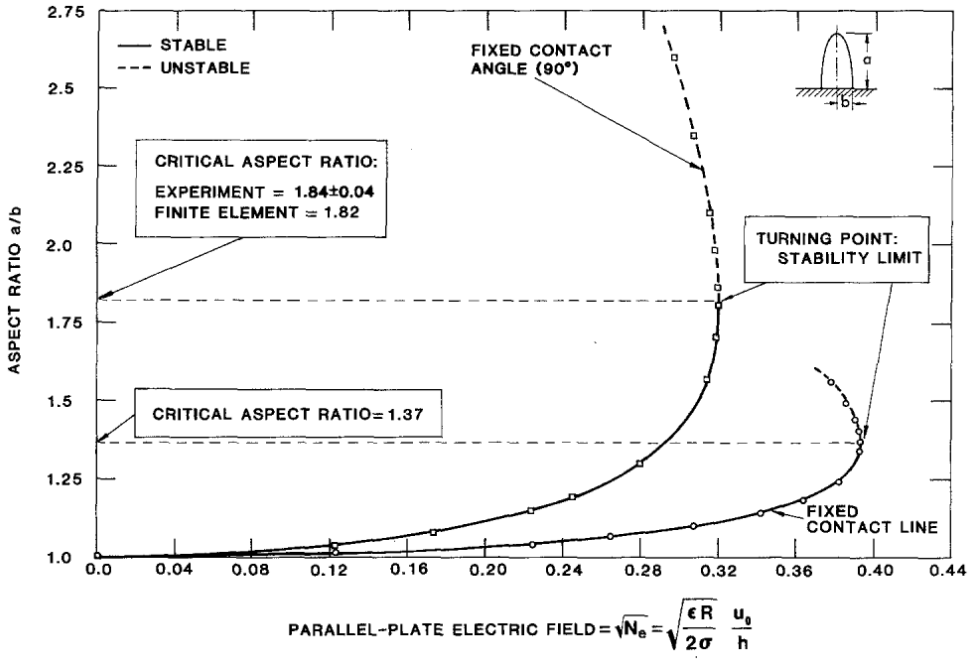

Figure 3.4: Chart, taken from [104], showing the aspect ratio b/r of a droplet (a/b in their notation) as a function of the dimensionless applied field, namely the square root of $\mathrm{Bo}_{e,d}$ ($\sqrt{\mathrm{Ne}}$ in their notation, ε being the permittivity of the exterior medium, r the initial droplet radius, σ the surface tension and u_0/h the applied electric field). The two curves correspond respectively to a droplet with a fixed contact angle and another with a fixed contact line. The solid and dashed part of the lines represent respectively the stable and unstable shapes.

figuration is the same as that studied in Ch. 6 with a droplet instead of a bubble. He assumes that the resulting polarisation causes the droplet to deform into a prolate spheroid and rationalises this deformation [36]. Later, Basaran *et al.* applied the same method as in Ref. [84, 80] to further study this deformation [104]. They showed that the aspect ratio of the droplet (the height of the droplet b divided by its base radius r) can be linked to the intensity of the applied uniform electric field E_0 (see Fig. 3.4) through the electrical Bond number, balancing the electrostatic and capillary pressures:

$$\mathrm{Bo}_{e,d} = \frac{\varepsilon_0 E_0^2 r_0}{2\gamma} \tag{3.7}$$

In the case of small deformations, for a hemispherical droplet with an initial radius r_0 and a fixed contact angle in a dielectric medium of permittivity ε_0, the law writes as follows

$$\frac{b}{r} = 1 + \frac{9}{4}\mathrm{Bo}_{e,d}. \tag{3.8}$$

A law linking $\mathrm{Bo}_{e,d}$ and the critical aspect ratio of a droplet, corresponding to the static aspect ratio of a droplet under conditions just below those needed to trigger the instability, has been found both experimentally and analytically by Beroz *et al.* [12]. Incidentally, the pictures used to illustrate the similarities between droplets and bubbles under an applied electric field in Fig. 1.2 (a) are from this work. These experiments were performed for a hemispherical conducting pendant droplet pinned on a conducting surface and subjected to a uniform electric field. They eventually came up with the law

$$\frac{r^3}{V_l} = \frac{\pi}{2}\mathrm{Bo}_{e,d} \tag{3.9}$$

for the droplet critical aspect ratio, where V_l is the initial volume of the drop.

3.3 Droplets Under a Magnetic Fields

As explained in Ch. 2.3.2, ferrofluids have only attracted attention relatively recently. Indeed, ferrofluids are colloidal suspensions that have

to be synthesised, as they are not found in nature. Thanks to the colloidal magnetic particles of which they are composed (maghemite in our case), ferrofluids are paramagnetic liquids with a response to magnetic field of the order of that found in ferromagnetic materials (this behaviour is called superparamagnetic). This response takes the form of both surface and volume forces, conversely to a perfectly conducting droplet subjected to an electric field where only a surface force is at work. Indeed, as they are made up of permanent magnetic moments $\vec{m}$, an applied magnetic field tends to align these moments and the ferrofluid itself may experience a volume force through the magnetic field gradient or magnetostrictive effects.

Manipulation with a simple permanent magnet of ferrofluid droplets illustrates the effect of the force driving the magnetic moments towards the higher field strengths [13]. When the permanent magnet is approached from below, the ferrofluid droplet deforms and, if the field gradient is strong enough, splits, forming a self-assembled pattern. If the magnet is moved horizontally, the deformed droplet or pattern follows it, thus remaining in the area of strong magnetic field.

The magnetic effects induced on a ferrofluid have also been studied by Rosensweig [56], who derived a generalised Bernoulli equation for the steady flow of an incompressible Newtonian ferrofluid[6]. This equation can be used to determine the stable shape of a ferrofluid droplet when the fluid velocity and the associated pressure are null. It can be written as follows

$$P_l + \mu_0 \int_0^{\tilde{H}} \left[\nu \frac{\partial M}{\partial \nu}\right]_{\tilde{H}^*,T} \mathrm{d}\tilde{H}^* + \rho g z = \mathrm{cst}. \tag{3.10}$$

The first and last terms are the usual terms of Bernoulli equation associated respectively with the pressure in the fluid and the hydrostatic pressure (see Eq. 3.1 with the speed-related pressure being equal to zero). The second term is the magnetostrictive pressure $P_{m,s}$ with M the magnetisation, $\tilde{H}$ the internal field related to the magnetic field B and ν the specific volume.

At the ferrofluid interface, in addition to this Bernoulli equation, the

[6]With other assumptions, see Ch. 5 in Ref [56] for more details.

following boundary condition must be satisfied

$$P_l + \mu_0 \int_0^{\tilde{H}} \left[\nu \frac{\partial M}{\partial \nu}\right]_{\tilde{H}^*,T} \mathrm{d}\tilde{H}^* + \mu_0 \int_0^{\tilde{H}} M \mathrm{d}\tilde{H}^* + \frac{\mu_0}{2} M_n^2 = P_0 + P_\gamma \quad (3.11)$$

with the last three terms on the left-hand side of the equation representing the magnetic effects. Additionally to the magnetostrictive pressure, the third term represents the overpressure inside the fluid due to the interaction between the magnetic moments $P_{m,i}$. The fourth term stands for the continuity of the normal magnetic field at the interface as well as the absence of free current inside the ferrofluid. It is called the normal magnetic traction $P_{m,n}$ with M_n, the component normal to the interface of the magnetisation.

The presence of volume and surface forces suggests that ferrofluid bubbles and droplets may deform differently when subjected to the same magnetic field. Indeed, whereas a droplet is composed entirely of liquid, a bubble concentrates most of it at its foot, in its meniscus. Consequently, a droplet is expected to deform entirely due to magnetic volume forces, while, for a bubble, only its meniscus is supposed to be reshaped by a magnetic field. We will see later that this is indeed the case. Nevertheless, the effects of magnetic fields on droplets have already been extensively studied and should help determine which magnetic effect is dominant under which conditions. As shown in the equations 3.10 and 3.11, magnetic effects may arise from three different phenomena each represented by a different pressure. In this thesis, as the ferrofluid is assumed to be incompressible, the magnetostrictive term has no influence on the flow. The only effect of this term is to increase the thermodynamic pressure inside the fluid by a constant amount and, provided we are not interested in compressibility phenomena, it can be omitted in the analysis [56].

When floating inside a non-magnetic fluid of matching density, a ferrofluid droplet is elongated by a magnetic field. In a series of articles , Bacri *et al.* [105, 106, 107] observed the behaviour of micrometric ferrofluid droplets under a magnetic field. To carry out these experiments, they used a biphasic aqueous solution in which one of the phases is highly concentrated in magnetic grains. This concentrated phase appears as micrometric magnetic droplets within the non-magnetic phase

and, when submitted to a magnetic field, they elongate in the magnetic field direction, shaping into ellipsoids. As they are suspended in a less concentrated phase of matching density, there is no effective gravity and the ferrofluid droplets' shape is completely prescribed by the surface tension and the alignment of the magnetic moments with the external field. The authors showed that the aspect ratio of ferrofluid droplets is fully determined by a dimensionless number comparing the magnetic and capillary effects. This magnetic Bond number reads [106]:

$$\mathrm{Bo}_{m,d} = \frac{\mu \tilde{H}_0^2 r_0}{2\gamma}, \tag{3.12}$$

with μ the permeability of the surrounding fluid and $\tilde{H}_0$ [A/m] the external applied field. The authors also observed the effect of the permeability ratio between the surrounding fluid and the droplet $\mu/(\mu_d - \mu)$, with μ_d the droplet permeability. For high ratio values, the evolution of the shape is monotonic, whereas for smaller ones, the growth of the aspect ratio becomes non-monotonic and the curve describing it as a function of $\mathrm{Bo}_{m,d}$ adopts an "S-shape". This curved shape induces a metastable aspect ratio of the droplet as well as hysteresis effects [106, 107]. On their side, Ivanov *et al.* [108] used the deformation of ferrofluid droplets present inside a ferrofluid emulsion to explain the non-monotonic behaviour of this emulsion permeability.

Later, Afkhami *et al.* [109] showed that millimetric droplets of ferrofluid suspended inside a viscous fluid of the same density can be described by the same Bond number (see Fig. 3.5). Numerous theoretical and numerical studies have confirmed the results obtained by Bacri *et al.* [110, 111]. Yet, Afkhami *et al.* observed that, for high magnetic field intensities, the experimental deformations deviate from those theoretically predicted. They attributed this discrepancy to a change in surface tension. However, Rowghanina *et al.* [112] found numerically that the spheroidal approximation remains valid only at the early stage of deformation, as Taylor did for a conducting droplet under electric field, inducing an irrepressible sense of *déjà vu* throughout the history. They showed that, considering that the poles of the droplet become sharp at high field intensities, the aspect ratio can be predicted with a unique surface tension. This deviation from an ellipsoidal shape had already

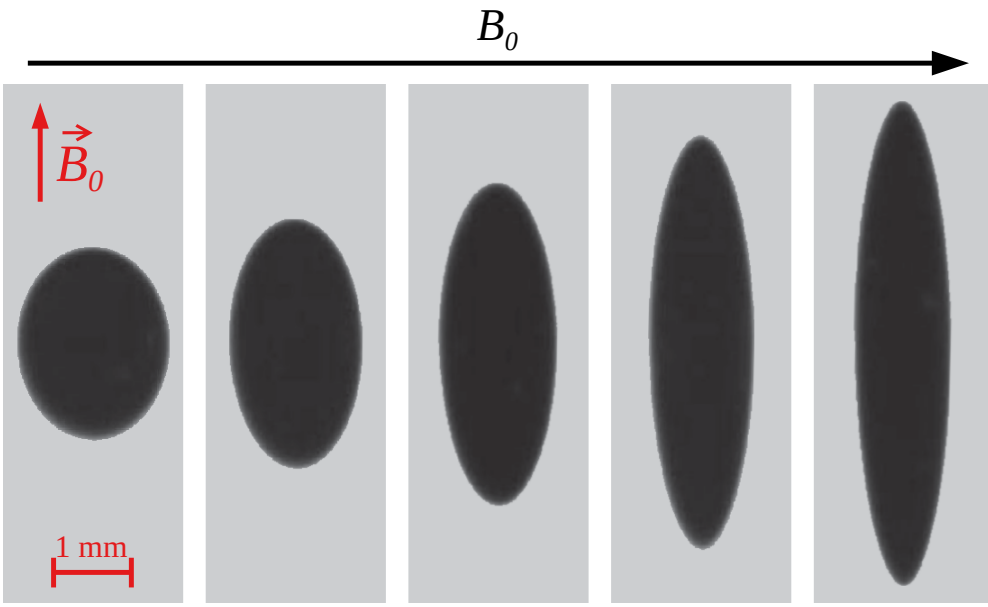

Figure 3.5: Pictures depicting the deformation of a ferrofluid droplet under an increasing external magnetic field $\vec{B}_0$ and, therefore, $\mathrm{Bo}_{m,d}$. The intensity of the external magnetic field B_0 varies from about 7.58 mT for the leftmost image, to 203.99 mT for the rightmost one. These pictures come from [109] and have been edited.

been experimentally point out by Bacri *et al.* [106], thus reinforcing the hypothesis of the change in shape.

The effect of a rotating magnetic field on ferrofluid droplets under the same conditions (in a non-magnetic fluid of matching density) has been investigated by Lebedev *et al.* [113]. They observed the following sequence of deformation with an increasing field intensity. First, from an initial spherical shape, the droplet flattens in a direction perpendicular to the rotation plane of the magnetic field, its shape becoming approximately an oblate spheroid. Then, another transition takes place and the droplet assumes the shape of an ellipsoid whose two major semi-axes are in the rotation plane. Finally, after a brief non-stationary state, the droplet develops peaks at its periphery, in the rotation plane. In

addition to these deformations, they observed that the droplet rotates in the same plane as the magnetic field. The angular velocity of this rotation increases with the intensity of the magnetic field and strongly depends on the droplet shape.

Rigoni *et al.* [114] studied the inverted system composed of non-magnetic aqueous droplets inside a ferrofluid solution (see Fig. 3.6). This system is the magnetic counterpart of the one studied by Wagoner *et al.* [86] and Brosseau *et al.* [88], consisting of dielectric droplets suspended in a more conductive medium. After applying a uniform magnetic field, they recorded the droplets deformation into a spheroid shape and noted that the deformation increases with time at constant magnetic field. They explain this by the absorption of surface-active species during the deformation process, inducing a lowering of the apparent surface tension. Furthermore, in addition to the deformation, they also detected that two aqueous droplets under a magnetic field attract each other and eventually coalesce. The behaviour presented here should be similar to that of bubbles fully immersed in a ferrofluid and not subjected to gravity.

In the same way as for the electric field, the presence of a substrate modifies the way the droplet is deformed. As our object of study in Ch. 7 is the sessile ferrofluid bubbles under a magnetic field, it is necessary to study this influence. As mentioned above, Timonen *et al.* [13] studied the deformation and division of such droplets resting on a superhydrophobic substrate. Later, Rigoni *et al.* [115] complemented this initial study by showing that the phenomenology of droplets deformation induced by a magnet is richer than what previously observed Timonen *et al.* [13]. They actually found that a ferrofluid droplet can be either flattened by the magnetic attraction resulting from a magnetic field gradient, or be elongated by a uniform magnetic field (see Fig. 3.7). The latter phenomenon is conveniently described by a dimensionless number that compares the pressure jump due to capillarity and magnetisation at the droplet interface. This number, which they called S, is directly linked to the magnetic Bond number[7] $\mathrm{Bo}_{m,d} = \mu\tilde{H}_0^2 r_0/2\gamma$ (Eq. 3.12) and

[7]Indeed, the magnetisation M is directly linked to the applied field $\tilde{H}_0$ through the magnetisation curve of the ferrofluid and the demagnetising factor due to the droplet shape.

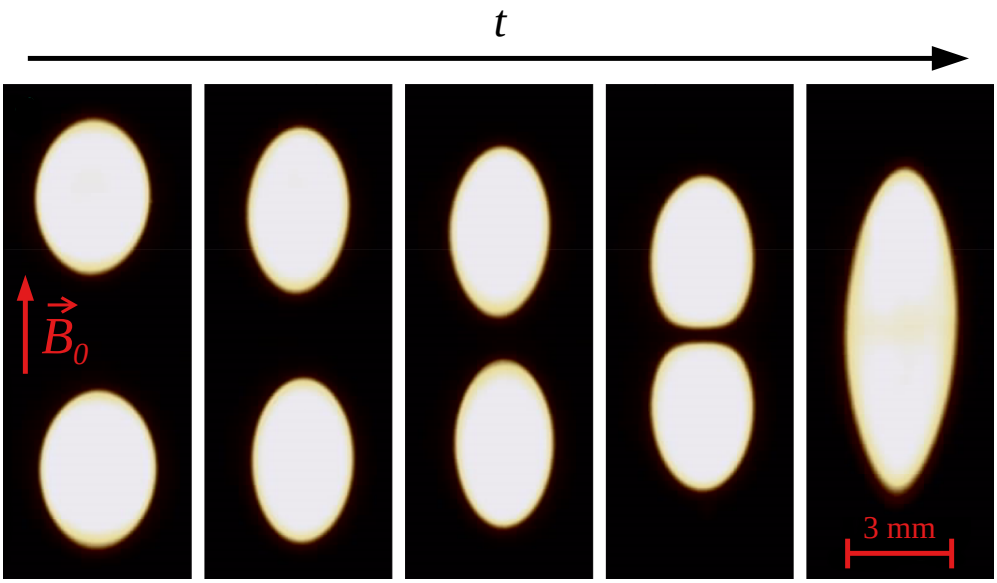

Figure 3.6: Pictures illustrating the deformation, attraction and coalescence of two water droplets inside a ferrofluid over time. The applied external magnetic field is constant and has an intensity of several hundredths of a Tesla. Due to the surfactant adsorption, the deformation is a very slow process, with a characteristic time of about 30 min. Comparatively, in the situation depicted in the figure, the attraction is relatively fast since it takes approximately 150 s for the droplets to make contact. Therefore, only the first part of the deformation process could be observed on this pictures sequence. Finally, the coalescence process can take several tens of minutes depending on the applied field. These pictures come from [114] and have been edited.

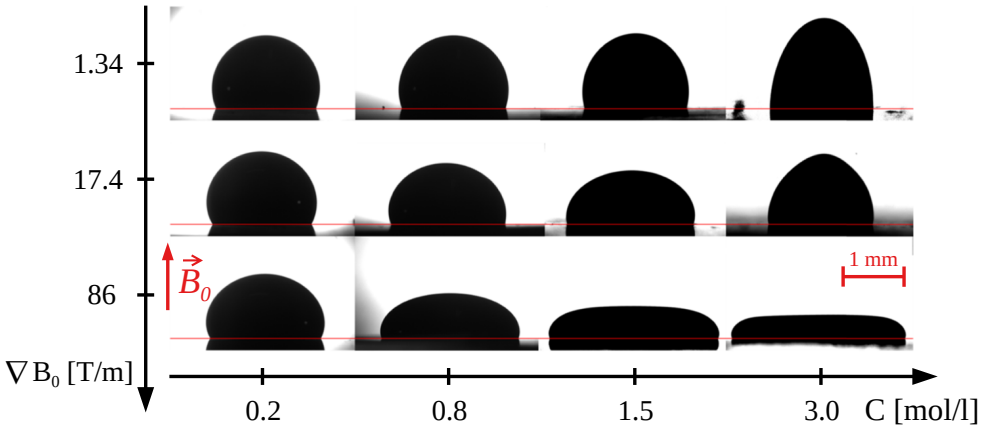

Figure 3.7: Pictures illustrating the deformation of sessile ferrofluid droplets under the application of the non-uniform magnetic field induced by a permanent magnet $\vec{B}_0$. The different columns represent different magnetic gradients and thus different values of Bo_{g^*}, while the columns stand for various ferrofluid solutions each with a different maghemite concentration. As the magnetisation directly depends on the maghemite concentrations, a variation of the concentration also induces a variation of S (for more details, see [115]). These pictures come from [115] and have been edited.

is expressed as follows

$$\mathrm{S} = \frac{\mu_0 M^2 V^{1/3}}{\gamma}. \tag{3.13}$$

The flattening is described thanks to an effective Bond number Bo_{g^*}, in which the gravitational acceleration has been replaced by the effective acceleration combining the gravitational and magnetic ones. This dimensionless number compares the effects of the two volume forces, which both flatten the droplet, and the effects of capillarity. It can be defined as follows

$$\mathrm{Bo}_{g^*} = \frac{\rho g^* V^{2/3}}{\gamma}, \tag{3.14}$$

where $g^* = g + M\nabla B_0/\rho$ [m/s^2] the effective acceleration intensity. Rigoni *et al.* [116] also shows that the same two dimensionless num-

bers (Eq. 3.13 and Eq. 3.14) well describe the separation of a ferrofluid droplet into daughter ones. Latikka *et al.* [117] investigated this separation into daughter droplets and noted the presence of satellite and subsatellite droplets after the division. They also studied the effect of the substrate as well as the impact of the ferrofluid composition on the self-assembled pattern induced by the separation. Finally, they proposed tensiometry methods and mechanisms to manipulate, split or merge ferrofluid droplets.

Ferrofluid droplets resting on solid interfaces also exhibit exotic phenomena [118, 119]. For example, Jamin *et al.* [120] observed the warping of a ferrofluid droplet by a planar sheet, called capillary origami. Under the effect of a magnetic field, they succeed in modifying the warping through the droplets deformation. Additionally, the self-assembly of ferrofluid droplets bears a striking similarity to the Bose-Enstein condensate [121]. In both cases, magnetic interactions are responsible for the pattern emergence. Finally, it is possible to combine electric and magnetic fields in order to obtain brand "new" effects. King *et al.* [122], for example, applied an electric field to the magnetically induced self-assembled pattern made by a conducting ferrofluid droplet (see Fig. 3.8). Electric and magnetic fields jointly act to produce an array of Taylor cones that begin to emit tiny charged ferrofluid droplets. This combination allows the electrospray emitters to be highly concentrated, enhancing the overall liquid ejection.

3.4 Conclusion

The effects of gravitational, electric, or magnetic fields on a droplet were presented. Particular attention was paid to the effect of external forces caused by these fields on the droplet shape. The droplet steady shape can be described by a generalised Bernoulli equation (see respectively Eq. 3.1 for a droplet solely deformed by gravity, Eq. 3.4 for a conducting droplet under an electric field and Eq. 3.10 for a ferrofluid droplet subjected to a magnetic field). The boundary conditions at the liquid/air interface must also be modified in order to account for electric and magnetic stresses (see Eq. 3.2 for the boundary conditions when only gravity is present, and Eq. 3.5 as well as Eq. 3.11 for a conducting

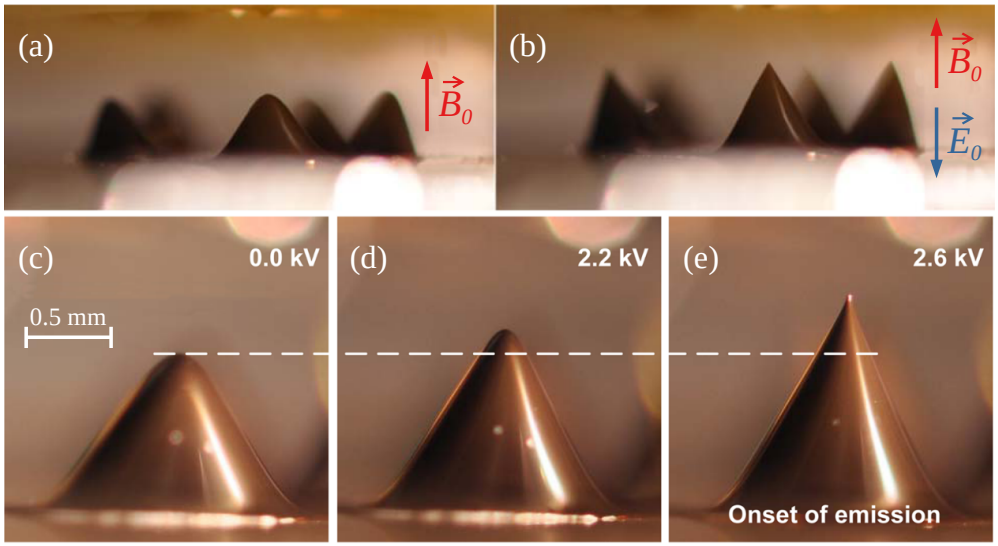

Figure 3.8: Images of the enhancement by an electric field $\vec{E}_0$ of a peak instability induced by a magnetic field $\vec{B}_0$. (a) Peaks instability (or Rosensweig instability) due to a non-uniform magnetic field generated by a permanent magnet $B_0 \approx 30$ mT. (b) Further increase of the peak sharpness by an applied uniform electric field $E_0 \approx 553$ V/mm, inducing the emission of microscopic droplets (Taylor cone). (c-e) Highlighting of a particular peak to emphasise the effect of the electric field. The applied potential sustaining the uniform electric field is indicated in the upper right corner of each picture. These pictures come from [122] and have been edited.

droplet in an electric field and a ferrofluid droplet in a magnetic field, respectively). This set of equations, consisting of the Bernoulli equation and the boundary conditions, is sufficient to describe the droplet shape under the above-mentioned fields. Since the droplet shape results from competition between capillarity and at least another pressure due to these external fields, the droplet deformations might be conveniently described in terms of dimensionless numbers highlighting these competitions (κ^{-1}, linked to Bo, X, $\mathrm{Bo}_{e,d}$, $\mathrm{Bo}_{m,d}$ and Bo_{g^*}).

The origin of the pressure responsible for the deformation of the droplet depends on the field used to generate it and can be either a surface or an in-fluid pressure. For example, the well-known hydrostatic pressure $P_h = \rho g z$ is the in-fluid pressure induced by the Earth's gravity. Conversely, an electric field applied to a conducting droplet causes only an electric pressure $P_e = \varepsilon_0 E_n^2/2$ at its surface. Finally, both a surface $P_{m,n} = \mu_0 M_n^2/2$ and an in-fluid pressure $P_{m,i} = \mu_0 \int_0^{\tilde{H}} M \mathrm{d}\tilde{H}^*$ are generated as soon as a ferrofluid droplet is subjected to a magnetic field. The superficial or in-fluid nature of these pressure sources is a key element in the thinking that guides this thesis.

Since droplets have attracted a lot of attention in the past, we would like to use them and their deformations under different fields as a starting point to better understand how bubbles react under similar fields (see Fig. 1.2). Firstly, from the shape point of view, a bubble is indeed very similar to a droplet unaffected by gravity, seeking a spherical shape when suspended in a medium of matching density, or a hemispherical one when resting on a solid substrate. Furthermore, when a conducting liquid is used to make a bubble or droplet, the electric effects due to an applied electric field take place only at their surface. Therefore, since only surface effects are present and are equivalent, a sessile bubble is expected to deform in a similar fashion as a hemispherical droplet. This similarity is illustrated in the first row of Fig. 1.2 where a droplet and a bubble are both made of a conducting liquid and subjected to an electric field. Yet, it should be noted that a bubble forms a thin hemispherical liquid shell enclosing an air pocket instead of a whole liquid hemisphere and consequently has two air/liquid interfaces. This suggests that bubbles should be twice as sensitive as droplets to surface effects and therefore their behaviour are expected to be qualitatively,

but not quantitatively, similar.

Secondly, from a volumetric point of view, droplets and bubbles are quite different. Indeed, the ratio between the liquid volume inside a droplet and its surface is much larger than that of a bubble. Moreover, the liquid shell forming the bubble contains only a small amount of the liquid used to create it. The vast majority of this liquid is concentrated at the junction between the bubble and the substrate, in the meniscus. As a result, spherical bubbles are less affected by volume forces and these forces' effects occur mainly within the bubble meniscus. A striking illustration of this phenomenon is the fact that the bubble shape is hardly deformed by gravity. Indeed, the shape of sessile bubbles remains hemispherical until they reach the size of a metre, unlike droplets which are flattened by gravity when their characteristic size is of the order of a millimetre (see Fig. 3.1). Yet gravity still impacts the bubble, but more locally, by constraining, together with capillarity, its meniscus shape. Another manifestation can be observed when a bubble made of ferrofluid is submitted to an applied magnetic field. In this case, the resulting deformation arise from a combination of volume and surface effects. As the majority of the ferrofluid accumulates within the meniscus, the latter is expected to be more affected by the magnetic field than the rest of the bubble. In contrast, the entire droplet is deformed by a magnetic field, causing the bubble to deform quite differently from the droplet. This divergence is illustrated in the second row of Fig. 1.2 where a droplet and a bubble are both made of ferrofluid and subjected to a magnetic field.

The effects of the different fields on the droplets shape having been detailed, we can now use this as a starting point to describe how a bubble reacts under the same conditions. The remainder of the manuscript is devoted to explaining and understanding the observations made on the phenomena presented in Fig. 1.2, representing the outline of this thesis. The next chapter, Ch. 4, is dedicated to the exposition of the bubbles particularities and the questions arising from them. The main objective of this manuscript is to answer these questions. Then, in Ch. 5, the "natural" bubble shape, namely under a gravity field, is presented both for bubbles resting on a solid substrate and for bubbles floating on a liquid pool. Finally, the next two chapters, respectively Ch. 6 and

Ch. 7, present the answers to the questions defined in Ch. 4 and focus respectively on the description of the shape of a bubble under an electric and a magnetic field.

4
Draw me a bubble

In Ch. 2, we took time to describe the different equations ruling fluid motions and the various pressures that are related to body forces and that influence these movements. This preliminary effort was important, as the conclusions we drew will serve as a compass to determine the relevant elements needed to describe the effects of body forces on bubbles. Moreover, in Ch. 3, we reviewed the effects of these forces on droplets and used the conclusions of Ch. 2 to highlight the dimensionless numbers translating the competitions defining the droplets shapes. As explained in Ch. 1, these observations serve as a starting point, a map, and, with the help of our compass, they constitute the right toolkit to undertake our scientific journey in the best possible conditions.

Thanks to the developments made, we can now precise the main objectives of this thesis which are related to two questions: how does a bubble deform under the action of an electric or a magnetic force and where do these forces manifest their effects within the bubble? First, to understand how a bubble deforms, it is necessary to find out which forces dominate the dynamics and how they compete to impose the steady shapes of a bubble, in other words, to identify which dimensionless numbers describe these phenomena. Second, once these competitions are extracted, the function that relates them to their respective steady shape can be obtained. In particular, we want to know whether a linear function can grasp the observed behaviour. Third, if so, the

field at which the shape begins to deviate from the linear prediction can be obtained, and we can properly define what are the "weak fields" in our cases. These three steps form the basic core of physical understanding and the next stage is to determine the physical significance of the weak fields limit. However, to achieve this particular step, much more complex tools are needed (involving numerical simulations or precise modelling of the local properties of the bubble) and we therefore stick to the first three, which we believe already give a very good understanding of the physical phenomena we want to describe. This allows us to provide a general guide on how to control, manipulate and deform bubbles using fields. The Ch. 6 and 7, respectively focusing on the effect of an electric and a magnetic force on the bubble shape, are therefore dedicated to follow these three steps to answer the question of how a bubble deforms under these respective fields. Conversely, in Ch. 5, devoted to gravity, we only define the competitions involved since $\vec{g}$ is held constant.

The question of where bubbles deform does not really need to be precise, but it can be motivated. Indeed, unlike droplets that are impacted in their entirety by body forces, bubbles are locally affected. This exceptional property is the reason why bubbles are a wonderful way to probe the surface or volume nature of a body force and is a consequence of two of its unique aspects. The first is that the bubble is a biphasic object with a unique interplay between its liquid and gaseous phases, as we have already pointed out in Ch. 1. When a force is applied to a bubble, it can affect one or both phases depending on their nature. In our case, the bubbles are blown with air and we can therefore assume that this phase is only affected by gravity. Conversely, the liquid phase we use is a soap mixture that can be based on a conducting liquid or a ferrofluid, allowing it to be impacted not solely by gravity but also by electric or magnetic forces.

The second crucial aspect of the bubble is its multi-scale feature. Indeed, whereas the gaseous phase appears in only one characteristic length through air volume V_g [m^3] (from the millimetre for the smallest, to the metre for the largest), the liquid one is multi-sized. First, the liquid shell defining the bubble volume has two characteristic lengths: its radius R_b [m], which is fixed by the gas volume, and its thickness e_b [m],

which is micrometric [123]. Then, the meniscus, forming the junction between the bubble and its substrate, has a height h_m [m] typically of the order of one millimetre in size. These two parts form the liquid distribution of the bubble and present a diametrically opposed volume to surface ratio: while the thin liquid shell envelops the entire bubble and therefore has a surface close to that of the bubble, the meniscus contains almost the whole liquid volume, but has a much smaller surface. Finally, there is a last scale at which the phenomena that allow the very existence of the bubble take place: the nanometre. Indeed, the amphiphilic or soap molecules (see Appendix B), which permit a bubble to live for more than a few microseconds (see Appendix C), organise themselves at the scale r_t [m] which is nanometric. By their nature, they agglomerate at the surface of the liquid or form micelles inside it. These different characteristic scales are illustrated in the upper part of Fig. 4.1.

Now that all the pieces are in place, we can contemplate the plans they draw. The biphasic nature of the bubble as well as the multi-scale feature of the liquid phase grant us to specifically target certain parts of the bubble by submitting it to different kinds of force. First, gravity acts on both the liquid and gas phases. As described in the next chapter (more precisely in Section 5.1), it prescribes the shape of the meniscus and even starts to influence that of the larger bubbles due to the weight of the liquid shell. Yet, gravity has an even more notable impact on floating bubbles due to buoyancy (see Section 5.2): it allows floating bubbles to assume shapes ranging from immersed spheres to emerged hemispheres. However, gravity is not the only force involved in these phenomena. All the shapes mentioned here are the result of a competition between gravity, which is a volume force, and surface tension, which is a surface one. The latter tends to minimise the surface and induces, together with gravity, the steady shape we are studying.

Electric and magnetic forces, for their part, directly affect only the liquid, merely deforming the gaseous phase through liquid manipulation. The unique liquid distribution formed by the meniscus and the shell as well as the different volume to surface ratios associated with them are the main reasons why the bubble is a perfect object to probe the surface or volume nature of a body force. Indeed, if a force mainly acts on the surface, such as the electric one on a conductor, it primary deforms the

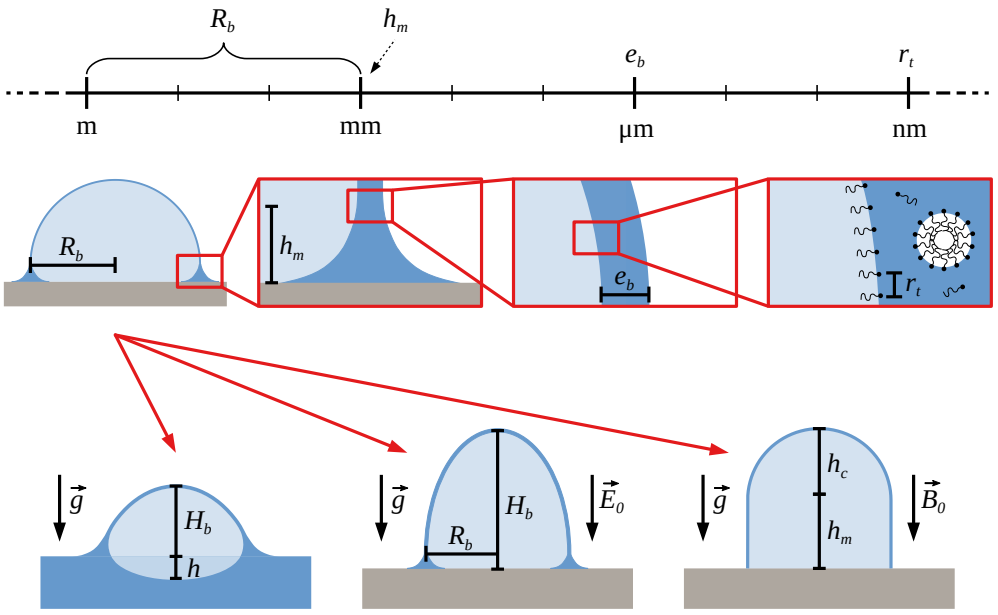

Figure 4.1: Miniature of the central double figure. It illustrates the different length scales involved in bubbles in its upper part: the bubble radius R_b (millimetre to metre), the meniscus height h_m (millimetre), the film thickness e_b (micrometre) and the typical length r_t at which soap molecules interact (nanometre). On its lower part, the different shape modifications due to gravity (more precisely buoyancy), electric or magnetic fields are represented with the corresponding chapter. First, the shape of a floating bubble, represented by its emerged height H_b [m] and its immersed depth h [m], is due to a competition between buoyancy and capillarity (see Ch. 5). Second, under an electric field, the shape of a sessile bubble is described by the ratio H_b/R_b and fixed by the balance between the electric and capillary pressures (see Ch. 6). Finally, under a magnetic field, the deformation is characterised by h_m as well as the height of the spherical cap h_c [m] and results from the equilibrium between the hydrostatic and magnetic pressures (see Ch. 7).

liquid shell (see Ch. 6) and, if another directly acts inside the volume, such as the magnetic one on a ferrofluid, it principally reshapes the meniscus (see Ch. 7). As with gravity, in both cases there are forces that counteract the modifications imposed by the electric and magnetic forces. In the former, it is surface tension, and the steady shape therefore results from a competition between two surface forces. In the latter, it is gravity and, in this case, the competition occurs between two volume forces. The different manipulations that can be made on the shape of the bubble by the different body forces are represented in the lower part of Fig. 4.1.

The glimpse provided by the rough plans we have just drawn is promising and confirms that the journey we want to undertake is worthwhile. Indeed, as the question in the title of this chapter suggests, it is not so straightforward to draw a bubble as can be seen in Fig. 4.1, because of its multi-scale and biphasic properties. Moreover, depending on the fields to which it is subjected, a bubble can take on quite different shapes: each of those fields acts mainly on one of its constituent parts. This particularity not only allows to act specifically on one element of a bubble but also to highlight the nature of the forces used to manipulate it. The reflections that underlie these conclusions provide insights into how a bubble reacts under an electric or magnetic field. On the one hand, since bubbles and droplets have a similar surface, they should undergo similar deformations under an electric field. However, we do not know to what extent these similarities are valid. On the other hand, bubbles and droplets have a distinct liquid distribution, so their deformation under magnetic field should be different. The first draft we have drawn here therefore needs to be refined to rationalise the deformations experienced by the bubbles and the rest of the thesis is devoted to this task.

5

Bubbles under a Gravity Field

Before we begin to describe the influence of gravity on the shape of a bubble, a clarification is needed. Generally speaking, bubbles are pockets of gas enclosed inside a more condensed medium. They can be encountered either in a liquid medium (as in sparkling beverages, beer or champagne), in a solid medium (ice or glass), or even inside a gaseous medium. For bubbles inside both condensed media, there is only one interface between the gas and the condensed phase (like a droplet in air). Conversely, as developed in the last chapter, bubbles inside a gaseous medium have their inner gas surrounded by a thin liquid film, forming a shell and inducing two liquid/air interfaces between the two distinct gaseous phases. The confusion between these two different configurations, which appears in many papers on the influence of fields on bubbles, is certainly not misleading in everyday life since, in sparkling beverages, bubbles are created within the liquid bulk and rise from this liquid to its interface to fizz or float. Nevertheless, in this thesis we are interested in soap film bubbles filled with air and surrounded by the same gas. The term "bubble" is then restrained to these objects. More precisely, in this chapter, we focus on the steady shape of bubbles resting at the interface between air and solid or floating at the interface between air and liquid. They are called sessile bubbles and floating bubbles respectively and each part of this chapter is devoted to the description of one of them before ending with a conclusion.

5.1 Sessile Bubbles

When air is blown into a puddle of soapy solution, a bubble is created and it rests on the solid surface on which the puddle was located, namely its substrate. A sketch of such a sessile bubble is drawn in the central part of Fig. 5.1. The main part of the bubble is a hemispherical liquid shell of thickness e_b that can be estimated to be a few microns or less [123][1] and a radius R_b. This curved liquid shell induces an excess of pressure $P_g = 4\gamma/R_b$ [N/m^2] on the internal air volume V_g. This Laplace pressure is equal to twice the one exerted on the liquid inside a droplet of the same radius R_b due to the presence of the two interfaces[2]. This excess pressure is precisely what allows the bubble to maintain a quasi-spherical shape by preventing the liquid film from collapsing under its own weight. Nevertheless, as there is only one interface between the outside air and the liquid, the liquid film is only subjected to an overpressure $P_l = 2\gamma/R_b$.

Underneath the hemispherical shell, there is an accumulation of liquid that forms the junction between the solid substrate and the main part of the bubble. This junction is called a meniscus and its height is denoted by h_m. The shape of this meniscus is the consequence of the competition between the hydrostatic pressure due to its weight and the capillary one related to its curvature. At equilibrium, both pressures must be equal and therefore the local curvature and height are linked [30]. Using a method similar to the one used to determine the shape of the meniscus formed by a liquid bath along a solid wall (see pages 48-50 of Ref. [30] for example), h_m can be estimated to be of the order of magnitude of the capillary length κ^{-1}, taking into account that the contact angle at the meniscus top is null since the bubble forms a hemispherical shell there. However, the liquid volume contained in the meniscus is finite and must therefore be taken into account when determining the actual shape of the meniscus. The liquid pool being an infinite reservoir of liquid, the h_m determined with a bath actually appears as the upper limit of h_m. This calculation gives us, nevertheless, the right order of

[1] In a first approach, we consider e_b as constant over the whole bubble film.

[2] The assumption $R_b \gg e_b$ is made here, implying that both interfaces contribute equally to the total excess pressure.

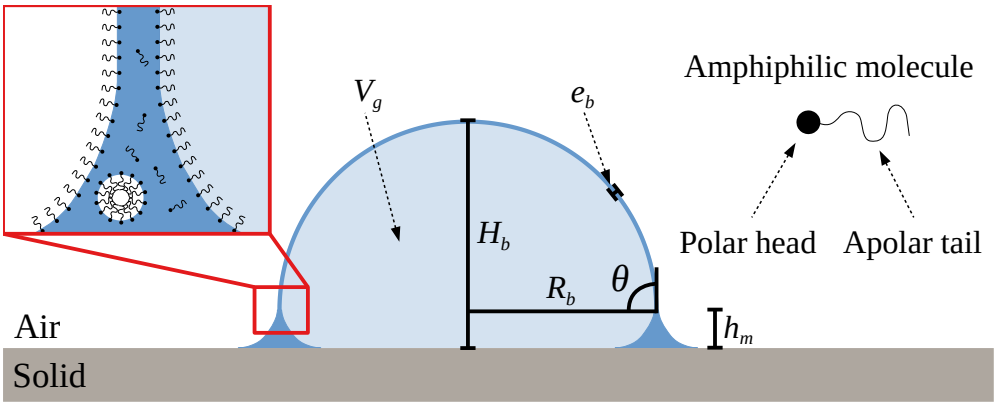

Figure 5.1: Sketch of a bubble resting on a solid substrate. The main part of the sketch highlights the internal air volume V_g and the different lengths involved: the radius R_b, the film thickness e_b, the meniscus height h_m and the total bubble height H_b. Moreover, the contact angle at the top of the meniscus θ is also shown. An enlargement of the situation inside the liquid film is represented on the left side of the sketch. Many of the surfactant molecules aggregate at the interface, stiffening it, or form micelles within the mass. Finally, a schematic amphiphilic molecule, with its polar head and apolar tail, is drawn on the right-hand side of the sketch (further explanations about amphiphilic molecules and their configuration are given in Appendix B).

magnitude.

At the junction between the meniscus and the rest of the bubble, the liquid film stands almost vertically before bending to form the hemispherical shell. The contact angle θ [°] between the liquid shell and the top of the meniscus is then very close to 90°. The total height of the bubble H_b is defined as the sum of the meniscus height h_m and the radius of the hemispherical shell measured at the meniscus top R_b. It should be noted that the hemispherical shape remains as long as h_m is small compared to H_b, as shown by Teixeira *et al.* [7]. When the size of the meniscus becomes comparable to that of the bubble, it has an increasing influence on the contact angle, changing the shape from a hemisphere to a spherical cap. Arscott [124] also showed that the wettability of the

resting surface changes the contact angle of the bubble. However, in our case, the liquid wets the substrate and the angle is then close to 90°, as predicted in Ref. [124].

The natural tendency of the bubble to form a spherical cap arises from the fact that the amount of liquid in a bubble is pretty small, allowing to define the overall shape of the bubble solely on the basis of capillary effects. In order to determine to what extent this assumption holds, the hydrostatic pressure due to the weight of the liquid film must be compared to the capillary pressure. This allows us to define an equivalent to the capillary length, but for bubbles [6]: $\varkappa^{-1} = \kappa^{-2}/e_b$ [m]. For a bubble made of Denkov's soap (see Appendix B for a description of the soap and see Table 3.1 for its properties) with $e_b \sim 1$ µm, the proportionality factor between $\varkappa^{-1}$ and κ^{-1} is equal to $\kappa^{-1}/e_b \sim 10^3$. As κ^{-1} is typically millimetric, the effect of gravity on the overall shape is thus expected only for bubbles with a radius of the order of a metre. Experimental verification of the gravity effects on very large bubbles, as well as further theoretical considerations, were carried out by Cohen *et al.* [6]. Yet, it should be noted that the described shape is only valid when the bubble is in a stationary state. For example, if it deflates, the bubble does not always keep this hemispherical shape, but may adopt other shapes, such as a spherical cap. The adopted shape depends not only on the liquid viscosity from which the bubble is made but also on the deflation speed as shown by Clerget *et al.* [125].

In the case of our experiments, all the bubbles had, at least, a typical length of two orders of magnitude smaller than $\varkappa^{-1}$, and always exhibit $h_m \ll H_b$. The shape of the liquid cap is therefore neither affected by gravity nor by the meniscus. Moreover, to confirm that bubbles have a shape close to that they adopt when the steady state is reached, we measured the shape of the bubble over time without any applied field. The experimental set-up we used is presented in Fig. 5.2. It is identical to the one used to measure the deformations induced by an electric field presented in Ch. 6 (see Fig. 6.2) without the elements necessary to apply an electric field. The solid substrate was therefore a rectangular aluminium plate (70 mm × 100 mm surface and 5 mm thickness) and the camera (Thorlabs USB model) used to acquire the images was controlled by a Python program. A micro pipette was used to release a 20 µl

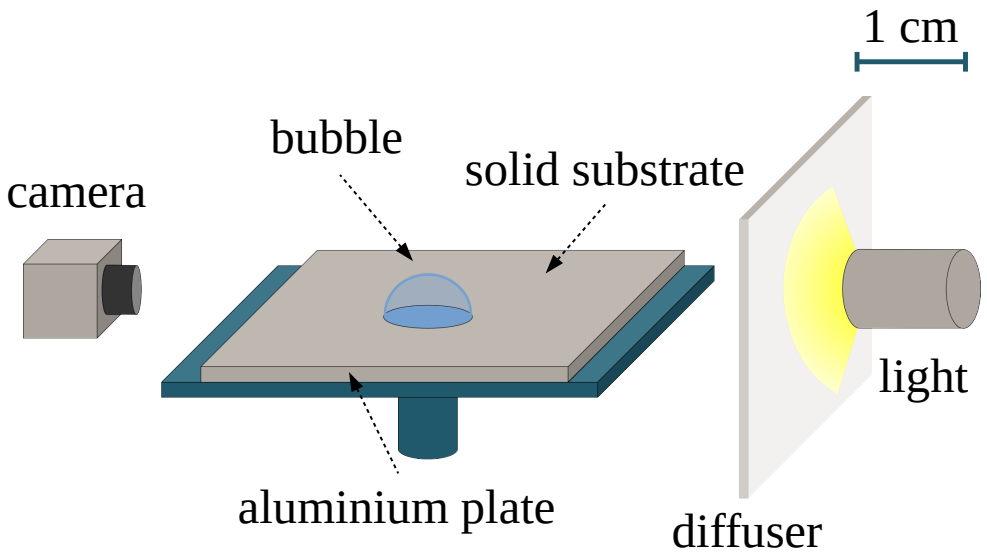

Figure 5.2: Sketch of the experimental set-up used to measure the characteristic time taken by a sessile bubble to reach its steady state. The set-up is the same as the one used to measure the deformations induced by an electric field (see Fig. 6.2) without the devices employed to apply the electric field. The solid substrate is a rectangular aluminium plate. The scale of the sketch is indicated in the upper right-hand corner.

droplet of soapy solution onto the solid substrate, and then the bubble was inflated using a syringe pump. The time required to inflate the bubble and start the experiment was approximately 10 s.

Due to its cylindrical symmetry, the shape of a sessile bubble can be represented by its dimensionless aspect ratio $\mathrm{Ar}(t) = H(t)/R(t)$ with the height of the bubble $H(t)$ [m] and its radius $R(t)$ [m]. In Fig. 5.3, the $\mathrm{Ar}(t)$ of a bubble resting on an aluminium plate is illustrated as a function of t. The gas volume in the bubble is equal to 1 ml and the changes in its shape are best fitted by an exponential function (black line in Fig. 5.3):

$$\mathrm{Ar}(t) = \mathrm{Ar}_s + D_s e^{-(t/\tau_c)}, \tag{5.1}$$

with $\mathrm{Ar}_s = H_b/R_b$ the steady aspect ratio, D_s the dimensionless defor-

mation, which is the difference between Ar_s and the initial aspect ratio $\mathrm{Ar}(0)$ and $\tau_c \simeq 3$ min the characteristic time of the deformation process. This deformation is therefore a slow process compared to a typical experimental step (namely 10 s). Moreover, as the amplitude of this deformation is small, we consider that its influence on the bubbles shape can be neglected and that sessile bubbles always have a hemispherical shape. That is to say, $H(t)$ as well as $R(t)$ are quite close to their steady values H_b and R_b, respectively.

The error bar shown in Fig. 5.3 represents an estimate of the typical error on the Ar_s measurements in the worst-case scenario. This error is inferred from the errors on H_b and R_b, which are related to the pixel resolution. It corresponds approximately to the size of a pixel whose real length is close to 10 µm. The errors on H_b measurements are linked to the bubble base and apex detection. As the apex is deduced by adjusting a circle to the top of the bubble edge, its detection has a subpixel accuracy. The base detection, obtained by the reflection of the bubble on the aluminium plate, is fairly accurate for sessile bubbles (namely two or three pixels). The standard error on H_b is therefore determined by the base detection and can be estimated, at worst, at 50 µm. The errors on R_b estimates are due to the meniscus and bubble edge detection. Since they are even more accurate than the base detection, the error on R_b is smaller than that on H_b. This corresponds to a characteristic relative error of one percent or less for both H_b and R_b. Consequently, the relative error on Ar_s can be deducted to be of the same order of magnitude as that on H_b or R_b.

Returning to the stationary shape, there are several possible reasons why the bubble shape changes over time. Firstly, the initial drainage following the bubble creation [126] could impact the bubble shape. Indeed, when a bubble is blown from a soapy solution, much of the liquid inside the cap is drained back to the meniscus, potentially modifying the bubble shape. However, this drainage has a very short characteristic time (namely 10^{-2} s for a bubble of $R_b \sim 5$ mm) compared to τ_c. Another phenomenon is thus at work. It could be the creeping of the contact line occurring when the bubble expands on the substrate. Indeed, when the bubble initially spreads, the contact line might get pinned, resulting in a constraint on the bubble shape. During the bubble lifetime, the contact

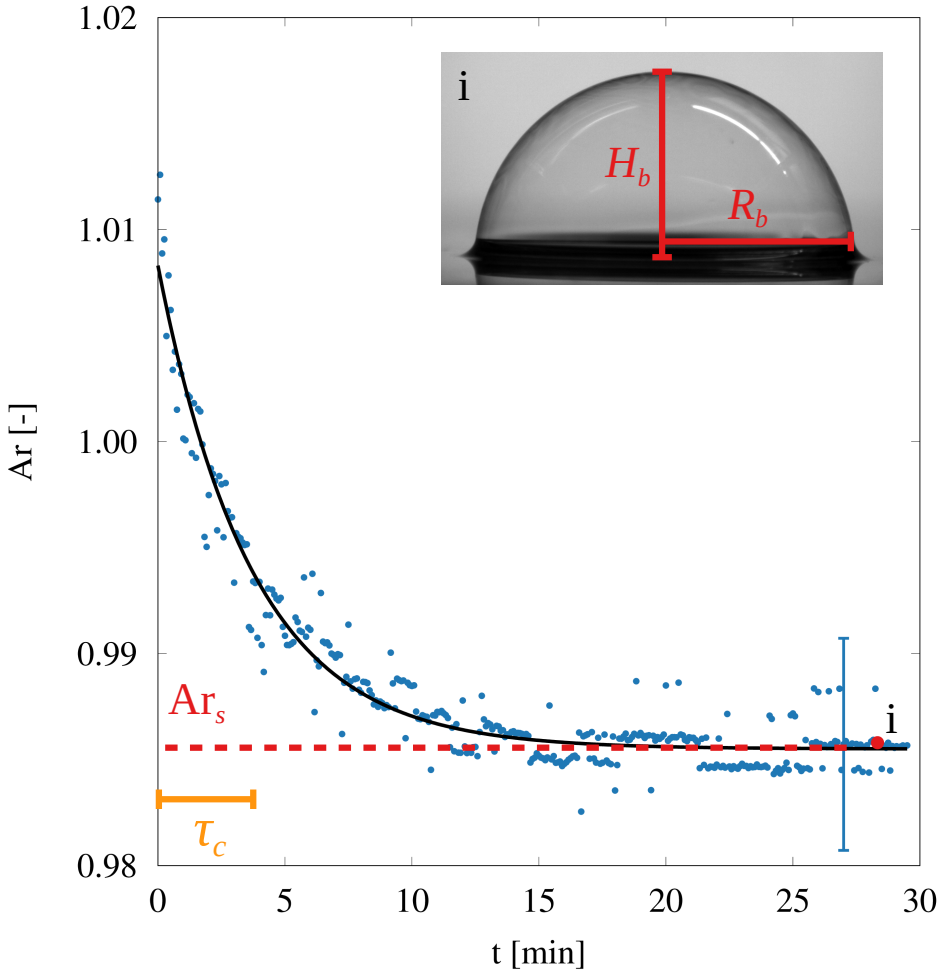

Figure 5.3: Dimensionless aspect ratio Ar_s of a sessile bubble as a function of time. The bubble rests on an aluminium plate and has an internal gas volume of $V_g = 1$ ml. The black curve is the fitting function described by Eq. 5.1 used to obtain the steady shape, characterised by the steady dimensionless aspect ratio Ar_s, the amplitude D_s and characteristic time τ_c of the deformation. The picture (i), shows the steady shape of the sessile bubble. A typical error bar, corresponding to the worst-case scenario, is indicated at the end of the curve.

line may recover some freedom, allowing the bubble to reshape, until the next stop. This process may be repeated, inducing a stick/slip motion called creeping, whose associated movements, that allow the shape adaptation, are a slow process (~ 1 min). This phenomenon could therefore explain the very slow deformation presented in Fig. 5.3. To get rid of this creeping effect, the pinning of the contact lines must be suppressed and one way to achieve this is to entirely remove the contact lines by substituting the solid substrate with a liquid bath.

5.2 Floating Bubbles

As they are "lighter" than the liquid of which they are made, bubbles are easily found at the interface between liquids and air. Even though they have a natural tendency to float on the liquid surface, they present both an emerged and an immersed part. Moreover, floating bubbles own a meniscus that is completely free to move across the pool due to the absence of contact lines. Therefore, there can be no creeping effect and the bubble steady shape is achieved after the initial drainage following the bubble creation. A sketch of a floating bubble is represented in Fig. 5.4 with the different lengths involved. Since the bubbles presented here are too small to have their emerged part flattened by gravity, we consider that they form a spherical cap of volume V_f [m^3] which can be characterised by its height H_b and its radius of curvature R_c [m]. In practice, R_c is obtained thanks to the radius taken at the meniscus top R_b and the contact angle θ measured at the same place through the relation $R_c = R_b/\sin(\theta)$. As previously, the meniscus height is denoted h_m and the thickness of the emerged film e_b. The latter is assumed constant throughout the film. The immersed part of volume V_i [m^3], on the other hand, does not have a constant curvature due to the hydrostatic pressure exerted on it. Its shape is rather complex, so we assume that it can be characterised through its deepness h and a constant radius of curvature R_i [m]. The overall validity of this hypothesis is debatable, but can be justified by the bubble shape, as described in the following.

Unlike sessile bubbles that naturally tend to form a hemisphere, the shape of floating bubbles is strongly impacted by their size. Indeed, as represented by the three sketches in Fig. 5.5, the shape of a floating

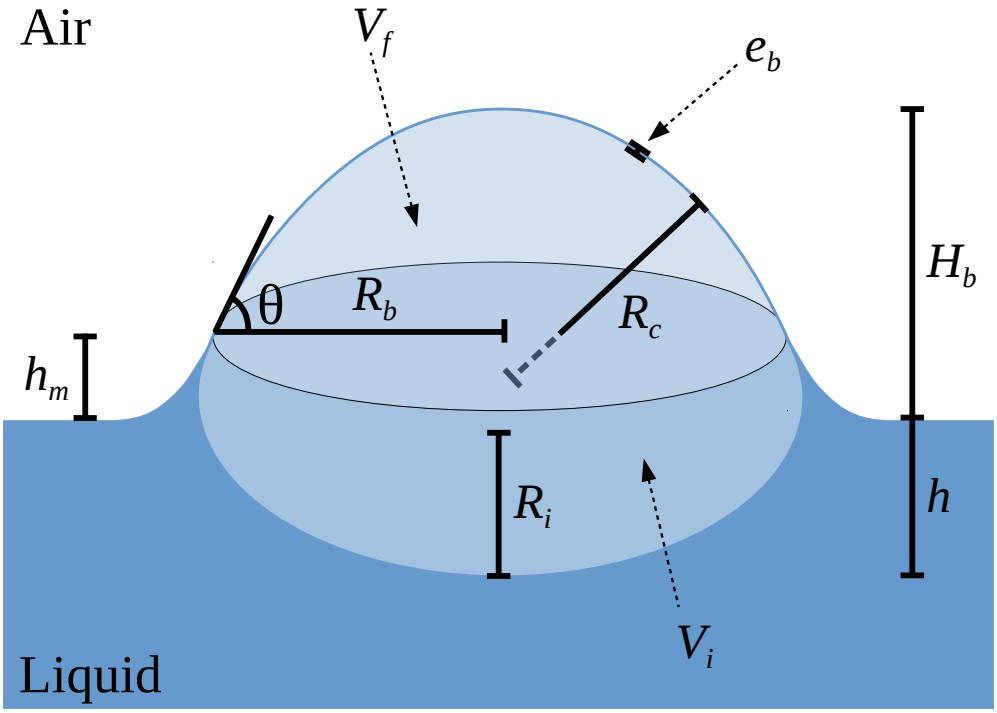

Figure 5.4: Sketch of a bubble floating on its own liquid. The emerged volume V_f, height H_b and radius of curvature R_c as well as their immersed counterparts V_i, h and R_i are drawn. Moreover, the thickness of the emerged part e_b and the meniscus height h_m are also given. Finally, the radius R_b and the contact angle θ at the meniscus top are indicated as the emerged part is a spherical cap inducing the relation $R_c = R_b/\sin(\theta)$.

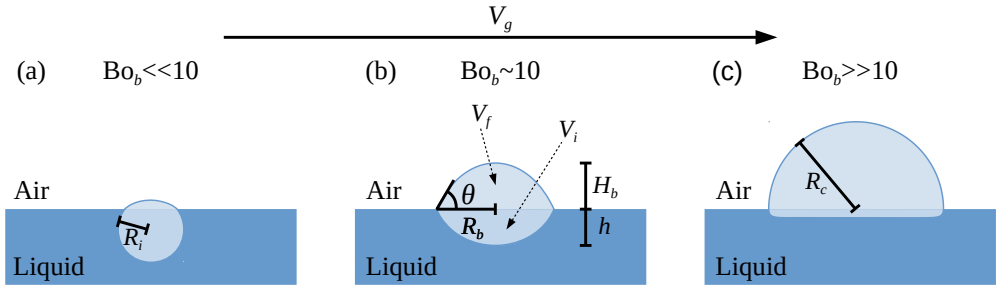

Figure 5.5: Sketches of bubbles floating on their own liquid. The typical size, and thus the total volume V_g and the buoyancy Bond number Bo_b, increase from left to right. The main geometric quantities are represented in each sketch. The meniscus is omitted to keep the three sketches clear. (a) Small bubbles are almost entirely immersed. The immersed part forms a truncated sphere of radius R_i while the emerged part is a spherical cap of radius $R_c \approx 2R_i$. (b) Intermediate bubbles have a comparable emerged and immersed part. It is assumed that they are formed by two spherical caps of similar radius of curvature such that $R_c \approx R_i$. (c) Larger bubbles are almost completely emerged and are then similar to sessile bubbles forming a hemisphere of radius $R_c \approx R_b$ and contact angle $\theta \sim 90°$. The immersed part is close to a flat interface leading to $R_i = \infty$.

bubble drastically changes as its size increases. It transits from an almost entirely immersed sphere to an almost fully emerged hemisphere. Floating bubbles can therefore be sorted into three categories according to their size. Each sketch in Fig. 5.5 represents a simplification of the adopted shape. For each of the three categories, the meniscus is omitted for clarification.

This separation into three size categories was originally proposed by Teixeira *et al.* [8]. They rationalised the influence of size through the buoyancy Bond number Bo_b, describing the competition between the gravitational energy due to buoyancy E_b [J] and the capillary energy E_c [J] when the bubble is fully immersed. Since $E_b \sim \rho g R_c^4$ and $E_c \sim \gamma R_c^2$,

the buoyancy Bond number is

$$\mathrm{Bo}_b = \rho g R_c^2/\gamma. \tag{5.2}$$

This formulation is obviously reminiscent of Bo and the relevant characteristic length is therefore also the capillary length κ^{-1}. For large Bo_b ($\mathrm{Bo}_b \gg 10$), buoyancy completely overcomes capillarity and the bubble emerges almost entirely. Conversely, for small Bo_b ($\mathrm{Bo}_b \ll 10$), capillarity completely dictates the behaviour of the bubble, which slightly emerges from the pool surface with a shape that closely resembles a sphere. An intermediate regime, for moderate Bo_b ($\mathrm{Bo}_b \sim 10$), characterises bubbles with enough gravitational energy to emerge from the bath, but not enough to allow us to completely neglect the surface minimisation effect due to capillarity. Each of these regimes has a characteristic shape which can be obtained from their typical size and some approximations which are detailed in the following.

The first category consists of large bubbles ($\mathrm{Bo}_b \gg 10$) that emerge almost entirely from the liquid and form a hemisphere with a radius $R_c \approx R_b$ and a contact angle $\theta \sim 90°$. The majority of their immersed part is flat (see Fig. 5.5 (c)), because of the hydrostatic pressure. Indeed, inside the bubble the gas undergoes an excess of pressure $P_g = 4\gamma/R_c$ compared to the external air medium. In addition, the immersed interface is subject to two other pressures: the hydrostatic pressure exerted by the liquid $P_h = \rho g z$ at a depth z and the Laplace pressure $P_\gamma = \gamma \mathcal{C}(z)$ due to the local curvature $\mathcal{C}(z)$. As the bubble is at the equilibrium, the pressure is constant throughout the internal gas and, at the immersed interface, the pressure balance is written as follows

$$P_0 + 4\frac{\gamma}{R_c} \sim P_0 + \rho g z + \gamma\, \mathcal{C}(z). \tag{5.3}$$

As the immersed interface penetrates deeper into the liquid bath, the hydrostatic pressure increases while the curvature of the interface decreases. Then, the former eventually equals P_g as the latter becomes null. The depth h and the curvature radius are therefore linked by the relation:

$$\sqrt{hR_c} \sim 2\kappa^{-1}. \tag{5.4}$$

This means that for sufficiently large bubbles, the depth h becomes very small and the immersed part is fairly well approximated by a flat interface ($R_i \to \infty$). Therefore, the ratio between the emerged part and the immersed one V_f/V_i tends towards infinity. In this case, floating bubbles behave similarly to sessile ones.

The second group is composed of small bubbles ($\mathrm{Bo}_b \ll 10$) that emerge only slightly from the surface ($V_f/V_i \to 0$). They resemble an immersed sphere of radius R_i (see Fig. 5.5 (a)). Since the depth h and both radii of curvature R_i and R_c are small, the hydrostatic pressure is negligible compared to the capillary pressures. The equilibrium at the immersed interface can therefore be written as follows

$$P_0 + 4\frac{\gamma}{R_c} \sim P_0 + 2\frac{\gamma}{R_i}, \tag{5.5}$$

leading to a ratio between the radii of curvature $R_c/R_i \approx 2$ [127]. Champagne bubbles, which have $R_i = 0.5$ mm, are a typical example of this behaviour [127]. Moreover, in the case of small bubbles, an expression linking the contact angle θ and the bubble size can be found [126]. Indeed, for an almost entirely immersed bubble of radius $R_c/2$, the vertical equilibrium between buoyancy and capillary forces acting on the emerged part can be written as follows

$$\rho g \frac{4\pi}{3}\left(\frac{R_c}{2}\right)^3 \sim 2\pi\gamma R_c \sin^2(\theta), \tag{5.6}$$

with $2\pi R_c \sin(\theta)$ the perimeter of the junction between the liquid bath and the emerged part. In the limit of small θ values, Eq. 5.6 can be rewritten to obtain the contact angle:

$$\theta \sim \frac{1}{2\sqrt{3}}\,\frac{R_c}{\kappa^{-1}} \tag{5.7}$$

The third class is an intermediate regime ($\mathrm{Bo}_b \sim 10$) made of bubbles of moderate size (see Fig. 5.5 (b)). The bubbles used in our experiment belong to this intermediate regime as illustrated in Table 5.1. This table shows, for each bubble size, the measured buoyancy Bond number $\mathrm{Bo_b}$ as well as the measured emerged height H_b adimensionalised by R_c,

V_g [ml]	$\mathrm{Bo_b}$ [-]	Ar_f [-]	Ar_f [-] [8]	h/R_c [-] [8]
1.00	15.46	0.80	0.76	0.22
0.50	12.61	0.75	0.73	0.26
0.25	9.92	0.70	0.69	0.31

Table 5.1: Comparison between our measured aspect ratios $\mathrm{Ar}_f = H_b/R_c$ and the theoretical ones obtained by Teixeira *et al.* [8] for the three different internal volumes V_g considered in the experiment presented in Ch. 6 and Ch. 7. The corresponding measured buoyancy Bond number Bo_b and the predicted immersed parts of the bubble represented by h/R_c, are also given.

namely the aspect ratio Ar_f. The measured aspect ratio is compared to the theoretical ones obtained by Teixeira *et al.* [8]. Finally, the predicted dimensionless immersed height h/R_c is given in the last column of the table. As Ar_f and h/R_c show, neither the emerged nor the immersed part of these bubbles can be neglected to determine their shape and reactions under the different fields.

As none of their parts can be neglected, these intermediate bubbles generally have a complex overall shape. However, it has already been pointed out that the emerged part forms a spherical cap, whereas the shape of the immersed one can be reasonably assumed thanks to the reflections we have just made. Indeed, the transition between small and large bubbles is continuous[3] and the ratio V_f/V_i must increase from 0 to ∞ while the ratio R_c/R_i must decrease from 2 to 0 as the bubble size increases. Therefore, for a given bubble size, these two ratios eventually become equal to one, meaning that the immersed and emerged parts become almost identical (see Fig. 5.5 (b)). Moreover, the shapes of the intermediate-sized bubbles presented in Ref. [8] are roughly symmetrical about an horizontal plane situated just below the top of the meniscus. All these considerations allow us to assume that the immersed part of

[3]This is actually the case: the variations of the different measurements used to characterise the bubble shape presented by Teixeira *et al.* [8] vary continuously with $\mathrm{Bo_b}$.

the intermediate bubbles is a spherical cap of radius $R_i \approx R_c$ and volume $V_i \approx V_f$.

As presented in the description of the three floating bubbles regimes, the gas volume V_g (through the Bo_b) of these bubbles is a key parameter in determining their shape and reaction when submitted to different fields. Indeed, on the one hand, small bubbles ($\mathrm{Bo}_b \ll 10$) have a shape that closely resembles an immersed sphere of radius R_i, and their surface energy is therefore mainly related to this immersed part. On the other hand, large bubbles ($\mathrm{Bo}_b \gg 10$) form almost a floating hemisphere of radius R_c, and their surface energy is principally defined by this emerged part. Finally, intermediate bubbles ($\mathrm{Bo}_b \sim 10$) have a complex shape because they have comparable immersed and emerged parts. However, both parts can be assumed as forming a spherical cap, the emerged one being characterised by its radius R_c and height H_b while the immersed one by it radius R_i and depth h. The surface energy of these intermediate bubbles is consequently linked to both interfaces and thus their reaction under fields as well. The separation into three bubbles regimes also allows us to justify the hypothesis made to describe the immersed shape at the beginning of this section. Indeed, for small, intermediate and large Bo_b, the immersed part of the bubbles forms respectively a truncated sphere, a spherical cap and a plateau, all of which can be characterised by a depth h and a constant radius of curvature R_i.

Although the shapes presented are stationary, the flows inside the liquid shell forming the bubble are not. Indeed, the liquid is drained towards the bubble base thanks to both gravity and capillarity, eventually leading to the bubble death. Although not the main focus of this thesis, the phenomena inducing this drainage are crucial to understand the bubble life and death. Appendix C is therefore dedicated to a brief description of the mechanisms that allow a bubble to live. Moreover, Appendix D explains under which conditions a bubble can self-heal a puncture in its liquid shell and under which it cannot, inevitably leading to its death.

5.3 Conclusion

The shapes assumed by both sessile (see Fig. 5.1) and floating bubbles (see Fig. 5.4) have been presented. The shape of a sessile bubble is mainly determined by the surface tension of its constituting liquid. It forms an almost perfect hemisphere, the only difference being the presence of the meniscus at the bubble base. Conversely, the floating bubble shape is fixed not only by its surface tension but also by the buoyancy acting on it. Three regimes can be identified according to the bubble size (see Fig. 5.5), ranging from small and almost completely immersed bubbles, to large and almost completely emerged ones. In the limit of very large bubbles, the shape is similar to that adopted by a sessile bubble. Yet, for a given liquid in a given gravity field, the shapes of both floating and sessile bubbles are completely prescribed by their characteristic emerged radius R_b.

Another major difference between sessile and floating bubbles is the presence of contact line. As shown in Fig. 5.3, it takes several minutes for a sessile bubble to reach its steady shape, even without any field other than gravity. This is probably due to the creeping of the contact lines which is typically a very slow process. In this regard, floating bubbles, although having a more complex shape, benefit from the absence of contact lines between their meniscus and the liquid pool. Indeed, the absence of creeping allows floating bubbles to reach their steady state much more quickly.

Now that the natural shapes of bubbles under gravity have been presented, we can focus on explaining how these initial shapes are deformed by the application of another external field. First, Ch. 6 is dedicated to describing the effects of an electric field on both sessile and floating bubbles. After, we explore how a magnetic field deforms sessile bubbles in Ch. 7. In these two chapters, the shape adopted by the bubble under gravity is taken as the initial shape of the bubble.

6
Bubbles under Electric Fields

When a bubble made of a perfectly conducting liquid is subjected to an external electric field, the resulting effects occur at its surface. The superficial nature of the reaction is highlighted by the observations presented in Fig. 1.2, which show that droplets and bubbles deform similarly when submitted to an electric field. Indeed, bubbles and droplets are similar regarding their surface and as the electric field induces a purely surface force, this analogy seems consistent. However, as mentioned in Ch. 4 and shown in Ch. 5, the resemblance between bubbles and droplets is only valid up to a certain extent. Firstly, the presence of a meniscus at the bubble base means that neither the surface at the junction with the substrate nor the wetting is similar. Secondly, the dual air/liquid interfaces that makes up the liquid shell, both contributing to the Laplace pressure, results in a completely different liquid distribution, with almost no liquid inside the liquid shell. Thirdly, bubbles can be found on both solid and liquid substrates, with floating bubbles adopting different shapes than those assumed by sessile ones. These three points, developed in the last chapter, show that the similarity between droplets and bubbles is limited and that to say that they should deform similarly when submitted to an electric field is only justified up to a certain point. Thus, although the analysis done on droplets is a good starting point, the deformations induced by an electric field on bubbles still need to be rationalised.

To this end, in the first part of this chapter, the principal similarities and differences between bubbles and droplets behaviours under an external electric field are outlined. After this first part, the experimental set-up and the methods used to study the deformation are described. First, we used this experimental set-up to explore the time dependence of the bubble height under electric field to properly define a steady state. Then, these steady heights are measured as a function of the applied electric field for both sessile bubbles and floating ones. The particularities thus highlighted allow a better understanding of how the mobility of the contact line, as well as the immersed part of the floating bubble, influence the deformation. In the next section, particular attention is paid to the meniscus and its effect on the overall bubble shape. Then, the liquid bath depth is considered by observing the deformation of a partially immersed bubble, which is viewed as a floating but frustrated bubble. Finally, a conclusion is drawn.

6.1 Bubble Particularities

As already pointed out in Section 3.2, the effect of an electric field on a bubble or a droplet strongly depends on the liquid conductivity. However, in Section 2.3.1, it was explained that the conducting or dielectric nature of a liquid is not absolute, but depends both on the characteristic time of the experiment and on its intrinsic properties through the electric relaxation time $\tau_e = \varepsilon/\sigma$. Water, for instance, has a permittivity $\varepsilon \approx 80\ \varepsilon_0$ and a conductivity $\sigma \approx 5.5\ 10^{-6}$S/m, giving $\tau_e \sim\approx 1.29\ 10^{-4}$ s. Assuming that the typical experiment time is much larger than τ_e, the effect of an electric field applied to a bubble or a droplet made of water is limited to the surface. Moreover, for a bubble, provided that the fluid is a perfect conductor, the electric field is external with all free charges situated on its outer interface, similarly to a droplet. Therefore, together with capillarity, the electric pressure P_e prescribes the pressure equilibrium at the interface under such a field. Consequently, Eq. 3.4 and Eq. 3.5 are suitable to describe the steady shape of the bubbles under an electric field. To wit,

$$P_l + \rho g z = \text{cst}, \tag{6.1}$$

$$P_l + \frac{\varepsilon_0}{2} E_n^2 = P_0 + P_\gamma. \tag{6.2}$$

with $P_\gamma = 2\gamma/R_b$, for a bubble of radius R_b and $P_e = \varepsilon_0 E_n^2/2$. It should be noted that the pressure difference between the liquid shell and the gas inside the bubble is simply $P\gamma = 2\gamma/R_b$. Indeed, as the bubble is made of a conducting liquid, there is no charge in the inner interface and therefore the boundary condition becomes the Laplace's equation.

These equations are also used to describe droplets, and thus there are similarities between the behaviour of bubbles and droplets under electric fields. For example, Pelesz's experiments [128] on pendant bubbles indicate that the maximum carried charge is well predicted by the fission ratio X defined for droplets by Eq. 3.6. Moreover, an analogous experiment to that proposed by William Gilbert in 1600 on droplets can be reproduced on bubbles. Take a balloon and rub it forcefully against the hair of a willing colleague or comrade to charge it. When the balloon is properly charged, you have what he calls an "electric", namely a dielectric charged by triboelectricity, and you can bring it close to a bubble lying on a dry surface to observe the bubble deforming into a cone. In this home-made experiment, the non-uniform electric field produced by the balloon deforms the bubble in the same way as the rubbed amber does to the droplet in the Gilbert's experiment[1].

This kind of deformation can be properly reproduced in laboratory, on both sessile and floating bubbles, with a uniform field generated by a plane capacitor, as shown by Taylor *et al.* [9], Basaran *et al.* [104] and Macky [10]. As observed in our home-made experiment, a bubble, consisting of a conducting liquid, initially forms a spherical cap (see Fig. 6.1 (a)) and, when subjected to an electric field $\vec{E}_0$, tends to elongate in the field direction, deforming into an ellipsoidal cap (see Fig. 6.1 (b)). When a critical field $\vec{E}_T$ [V/m] is reached, the electric force acting on the fluid particles overpasses the cohesive force due to surface tension and the bubble starts to eject charged liquid. Simultaneously with this discharge, the bubble undergoes a drastic change in shape transiting

[1] A video, illustrating this home-made experiment, is available at the following link: www.youtube.com/watch?v=HO3Iz1AnjkQ. I would like to take this opportunity to thank my fellow volunteer for agreeing to share her hair and be a part of this demonstration.

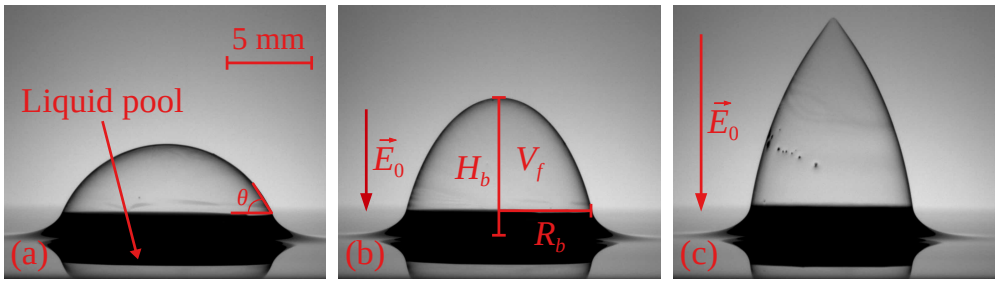

Figure 6.1: Pictures of a bubble floating on a soap pool submitted to an external uniform electric field. Picture (a) shows the bubble on a liquid pool when the intensity of the electric field $E_0 = 0$. (b) Deformation of a bubble induced by the applied uniform electric field. The bubble adopts a hemi-spheroidal shape when $E_0 < E_T$ with E_T the intensity needed to trigger the instability. (c) When $E_0 > E_T$, the instability occurs, the bubble becomes pointy and starts to eject droplets towards the upper plate in order to discharge. This behaviour is called the Taylor's cone. The height H_b and the radius R_b of the bubble are measured, as well as the emerged volume V_f and the initial contact angle θ (namely when the bubble suffer only the gravity field) of the bubble.

from an ellipsoid to a cone (see Fig. 6.1 (c)). The resulting instability is known as the Taylor's cone. Naturally, this behaviour is very similar to that observed for small droplets under similar conditions [36], certainly justifying why bubbles have been considered as a particular case of droplets with two interfaces [104, 12] since these initial studies. Nevertheless, they have their own peculiarities as observed by Hilton *et al.* [129].

The substrate also has a great impact on the bubble deformations. Indeed, although the substrate nature can change the initial shape of a droplet (see Fig. A.1), the sessile bubble used always has an initial contact angle at the top of the meniscus of $\theta \sim 90°$. However, when deformed, bubble may be frustrated due to contact line hysteresis, potentially like sessile droplets. Until now, studies of sessile bubbles have dealt with the mobility of the contact line by pre-wetting the solid surfaces, which only allows partial control of its pinning [104, 9, 10]. To

completely remove the influence of the pinning of the contact line, we decided to replace the solid substrate by a liquid pool. Macky [10] has already done similar experiments with floating bubbles, but the resulting effect of the substrate remained unsettled. This is mainly because the pool of soapy solution was considered a convenient way to feed the Taylor cone in liquid (in order to study it longer) rather than a relevant parameter of the experiment.

It should be noted that a soap film can also adopt other configurations, a bubble being only one of them. These other configurations make it possible to study the electric field influence on soap films of different initial shapes. For example, a flat liquid film subjected to a perpendicular electric field showed major differences with its equivalent system composed of a single interface [46]. Moreover, Moulton *et al.* [130] showed that the shape of a soap film membrane initially forming a catenoid can also be modified by an electric field when assembled as a cylindrical capacitor. In this particular experiment, a voltage was applied between a metallic rod situated along the radial axis of the catenoid and the catenoid itself, which was grounded. This causes the soap film to be attracted by the central electrode upon application of an electric field.

6.2 Materials and Methods

To study the deformation induced on a bubble by an applied uniform electric field, a plane capacitor consisting of two rectangular aluminium plates (70 mm $\times$ 100 mm in surface and 5 mm in thickness) was used. The bottom electrode of the capacitor, which was grounded, was also used as a substrate for the bubble. This electrode could also be immersed in a liquid bath contained in a Petri dish of 70 mm radius and 10 mm depth filled to the brim. The bath was made of the same mixture as the bubbles. This set-up enabled us to perform experiments on sessile bubbles resting on a dry aluminium plate as well as on bubbles floating on a soap pool. The distance between the immersed electrode and the liquid surface, labelled e [m], was controlled by modifying the position of this electrode in the bath. A high voltage DC power supply (PS375 Stanford research systems) was used to apply a voltage between

the plates. This generator can reach a maximum voltage of 20 kV and was controlled using a Python program through a GPIB bus. This program was also used to acquire images from a camera (Thorlabs USB model). The top plate was supported by a Perspex frame, allowing the distance between the liquid surface and the top electrode to be varied ($d = 15,\ 20$ and 25 mm) as well as the distance between electrodes $d_t = d + e$ [m] (in absence of a bath, $d_t = d$ as $e = 0$ mm). Sketches of the experimental set-up are presented in Fig. 6.2.

The bubble, as well as the bath, are made of Denkov's soapy solution, as described in Appendix B. The permittivity of this mixture is estimated to be close to that of pure water, namely $\varepsilon \approx 80\ \varepsilon_0$, and its conductivity is at least equal to that of the same pure water $\sigma > 5.5\ 10^{-6}$S/m. Therefore, the Denkov mixture has a characteristic electric relaxation time $\tau_{e,l} = \varepsilon/\sigma < 1.29\ 10^{-4}$ s. Since the surrounding gas is air ($\tau_{e,g} = \varepsilon_0/\sigma_g \sim 10^3$ s) and the time characterising the experiment $t_{step} \sim 10^1$ s, the bubble and the soap pool could be regarded as perfect conductors while air was considered a perfect dielectric. Consequently, the actual bottom electrode of the capacitor in the floating bubble experiments was defined by the surface of the liquid pool and, therefore, the capacitor thickness was d.

To perform experiments on a solid substrate, a 20 µl droplet of soapy solution was released onto the bottom electrode using a micro pipette and the bubble was then inflated thanks to a syringe pump. To study floating bubbles, air was injected directly below the surface. The time required to inflate the bubbles and start the experiment was roughly 10 s. This protocol made it possible to control the gas volume in the bubble ($V_g = 1,\ 0.5$ and 0.25 ml) and thus its typical size. Nevertheless, the final volume was not perfectly reproducible due to leakage and air compressibility. The exact volume was therefore obtained by image analysis after the bubble generation. In the case of floating bubbles, the apparent volume, which is the emerged volume V_f, differs from V_g since a part of the bubbles was immersed. These measures, plus the height and radius of the bubble, respectively labelled H_b and R_b, were performed by an home-made Python program detecting the edge and the meniscus of the bubbles. Note that R_b was measured at the top of the meniscus (see Fig. 6.1 (b)).

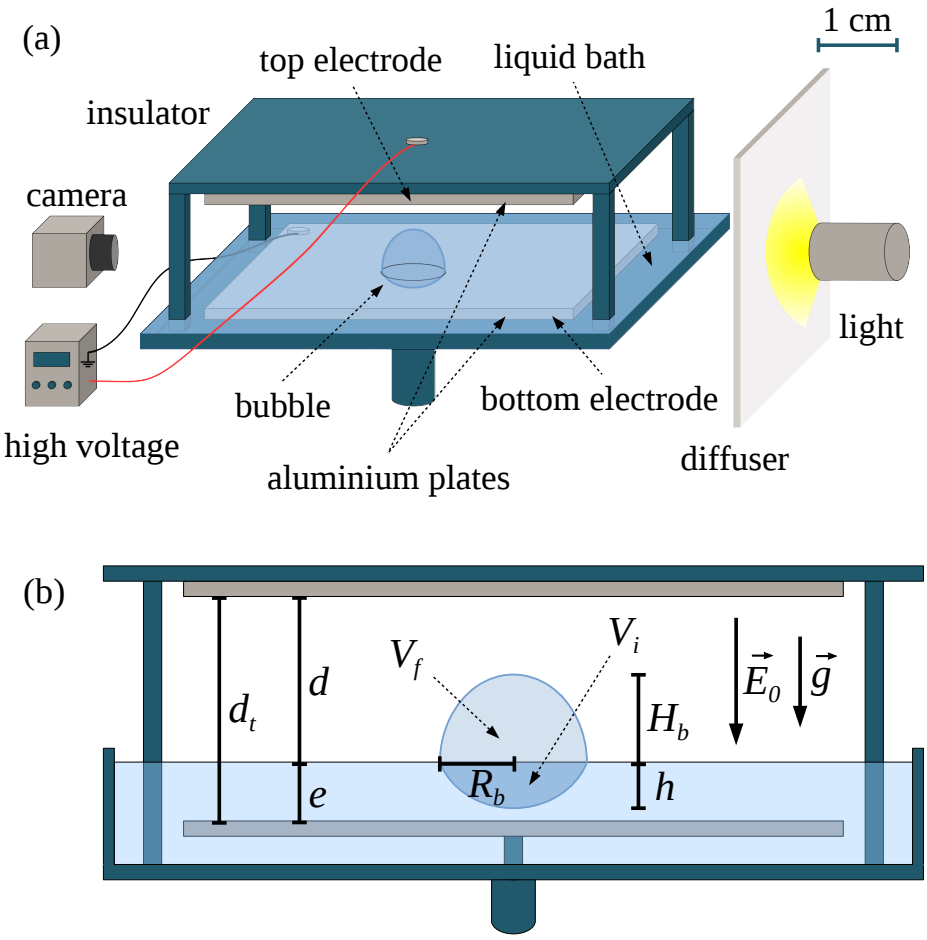

Figure 6.2: Sketches of the experimental set-up used for the experiments performed on floating bubbles. (a) Summary of the components of the experimental set-up. (b) Drawing of the geometrical measurements of the experiment: the liquid depth e between the immersed electrode and the liquid surface, the size of the capacitor d, the distance between electrodes d_t, the electric field $\vec{E}_0$, the gravity field $\vec{g}$, the penetration depth h, the height H_b and radius R_b (measured at the top of the meniscus) of the bubble as well as its emerged and immersed volume V_f and V_i. The scale of both sketches is the same and is indicated in the upper right-hand corner.

The home-made Python program used to measure the different characteristic lengths defining the bubble shapes applies the following procedure. After cropping, the edge of the bubble was detected by thresholding the image. Another threshold was applied to the initial image to identify the meniscus. Using the bubble and meniscus edges, the meniscus height h_m was measured together with the height of the spherical cap siting atop of the meniscus h_c through the total bubble height H_b (the sum of h_m and h_c being equal to H_b). The bubble radius at the top of the meniscus R_b was also measured. In addition, the apex coordinates and the curvature at this point were obtained by adjusting an even fourth degree polynomial to the highest part of the edge. Finally, on floating bubbles, the angle at the top of the meniscus θ_b [°], which is modified by the application of an electric field, was measured by adjusting a third degree polynomial around the meniscus top on either side of the bubble. The right and left angles were then extracted and, assuming they were close (namely, the difference between them was less than a few percents), the average value was used to define θ_b. On sessile bubbles, the angle being close to 90°, the third degree function did not give a satisfactory accuracy[2] and the angle was assumed to be equal to 90°. In particular, this procedure was used to obtain the initial contact angle θ (namely when no electric field was applied). An example of a typical image on which the lengths detected by the procedure have been drawn is presented in Fig. 6.3.

In addition to these characteristic lengths, the surface area S_f [m^2] and volume V_f of the floating bubble were calculated assuming cylindrical symmetry. More precisely, the bubbles were separated into a right and a left part according to the position of the apex as it represents the horizontal midpoint according to the cylindrical symmetry. The left and right parts were then cut into slices of one pixel in height, each slice forming a trapezium. By applying cylindrical symmetry, each trapezium forms a truncated cone of one pixel height from which the lateral area and volume were calculated. Finally, these lateral areas and volumes were summed over the entire height of the bubble. The values obtained on either side of the apex were then compared to validate the

[2]Indeed, the edge rises almost vertically and cannot be captured by a function.

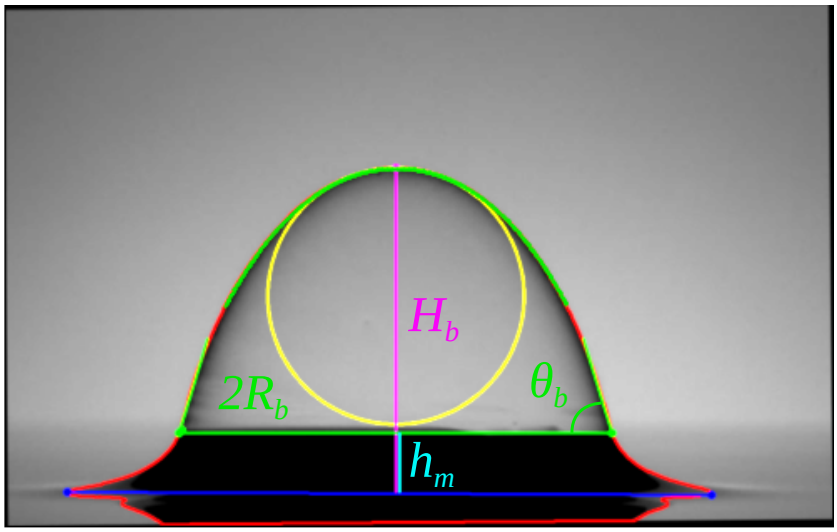

Figure 6.3: Picture of a bubble ($V_g = 0.5$ ml) used by the Python routine to extract its various characteristic lengths. The electric field to which the bubble is subjected has an intensity $E_0 = 450$ V/mm and is generated by a plane capacitor of size $d = 20$ mm. This picture is the same as that presented in inset (ii) of Fig. 6.5. The detected edge of the bubble is drawn in red, its base in blue and its total height H_b in pink. The meniscus height h_m is shown in cyan and the length $2R_b$ as well as the angle θ_b, both measured at the top of the meniscus, in green. The upper part of the edge used to determine the position of the apex and the curvature at this point is highlighted in dark green and the resulting circle is drawn in yellow.

detection of the edges and the apex. Assuming that they were close (*i.e.* , the difference between them was less than a few percents), the averaged value was used to define the surface S_f and volume V_f of the bubble.

The typical errors on the measurements of H_b and R_b have the same origin as the one already described in Section 5.1. However, in the case of floating bubbles, the base detection is less accurate (namely about ten pixels) and the resulting error on H_b is estimated to be, in the worst-case scenario, equal to 100 µm. Conversely, the edge detection and the resulting error on R_b remain unchanged (*i.e.* less than 50 µm). This results in a characteristic relative error of a few percents or less for both H_b and R_b and, therefore, a maximum relative error on their ratio of the same order of magnitude. The errors on h_m can be inferred in the same way. They depend on both base and meniscus detection, the latter being more accurate than the former. Consequently, the resulting error on h_m has the same origin as that on H_b and is estimated to be of the same order of magnitude. Finally, the precision of the surface area S_f and the volume V_f measurements is of the order of a few percents for both and the error on θ_b (and in particular on θ) is estimated to be of the order of 2°.

The experiments were performed by increasing the voltage ϕ [V] by steps of ϕ_{step} [V] every duration t_{step} from ϕ_{min} [V] to ϕ_{max} [V] and by recording the successive deformations with a camera. All experiments were realised at least twice. As a plane capacitor was used, an increase in voltage resulted in a growth of the intensity of the applied uniform electric field $E_0 = \phi/d$ inside the capacitor. A systematic error arises from the uncertainty in d (estimated to be equal to 0.5 mm) which affects equivalently all absolute values of E_0, but has no effect on the overall appearance of the curves. A picture of the bubble was taken at the end of each step, *i.e.* just before the voltage changes. A 20 s delay was imposed before each experiment in order to minimise the temporal effects due to the initial ageing of the bubble. The DC power supply controlled the voltage with an accuracy of the order of 1 V and allowed a maximum current of 525 µA. It took approximately 1 s to reach the voltage setpoint independently of the variation of the voltage and the voltage itself. A sketch of the time process is drawn in Fig. 6.4.

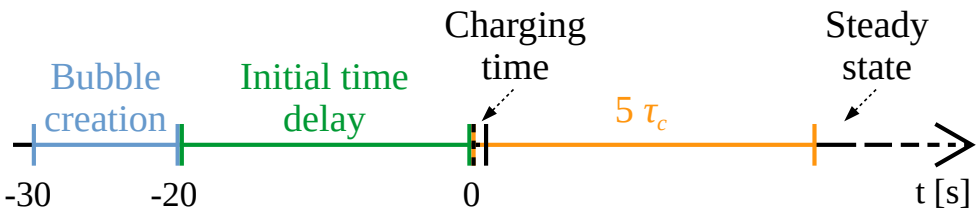

Figure 6.4: Sketch of the typical time process of an experiment. In the present case, the experiment depicted in Fig. 6.5 was used as an illustration. The starting point for all experiments is the bubble creation, shown in blue, which takes roughly 10 s. After creation, a delay of 20 s, depicted in green, is imposed to minimise the effects of initial ageing. The generator is switched on at $t = 0$ s and the experiment begins. It takes approximately 1 s to reach the voltage setpoint (in black). A time equal to $5\tau_c$ of the experiment presented in Fig. 6.5 is represented in yellow to give a comparison point. This time corresponds to the one required to reach at least 90% of the deformation, which is defined as the beginning of the steady state.

6.3 Steady State

When a voltage is applied, it takes some time for the bubble to stabilise and reach a new steady state. In order to estimate this duration, we applied a high voltage and we tracked the height of the bubble $H(t)$ over time. The height $H(t)$ is defined as the semi-major axis of the hemi-spheroid formed by the bubble. This experiment was performed with a floating bubble of $V_g = 0.5$ ml inside a capacitor of $d = 20$ mm. At $t < 0$ s, the DC power supply was switched off and the voltage between the liquid pool and the top plate was null. At $t = 0$ s, the generator was switched on and, within the next second, the top plate was brought to 9 kV (a voltage very close to that required to trigger the Taylor cone). In Fig. 6.5, H is reported as a function of time in a spatio-temporal diagram. The shapes of the bubble in the initial and final situations are respectively shown as insets (i) and (ii). The time required to reach a steady height H_b is modelled thanks to a characteristic time τ_c. Since the

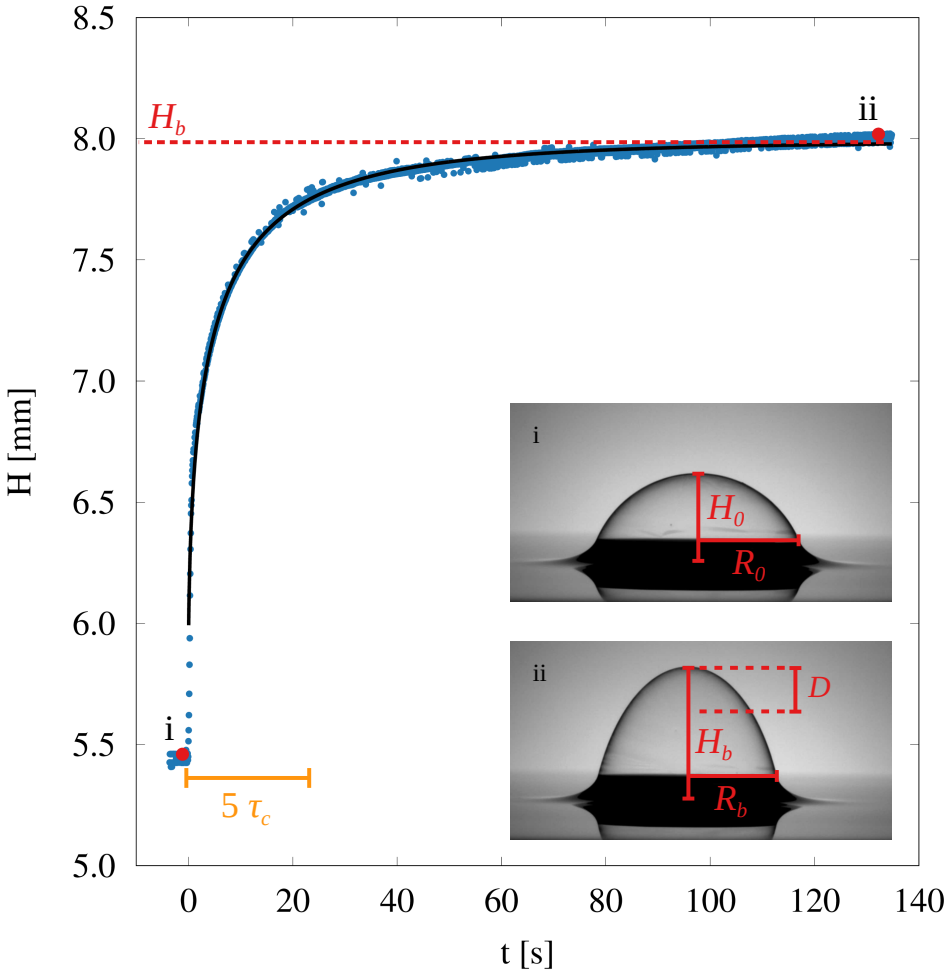

Figure 6.5: Height of the floating bubble H as a function of time. The size of the capacitor was $d = 20$ mm and the volume of the bubble was $V_g = 0.5$ ml. At the time $t = 0$ s the DC power supply was set on and the top plate reached the preset voltage. Here, only one step is needed to go from 0 kV (see picture (i)) to 9 kV (see picture (ii)). The black line is the fitting function, described by Eq. 6.3, used to obtain the characteristic time τ_c, the deformation D and the steady height H_b. The τ_c for this experiment was found equal to 4.7 s.

pressure constraints depend on the bubble shape, this characteristic time τ_c was obtained by fitting (black line in Fig. 6.5) a stretched exponential function [131]:

$$H(t) = H_b - De^{-\sqrt{(t/\tau_c)}}. \tag{6.3}$$

We note D [m] the amplitude of the bubble deformation (*i.e.* the difference between H_b and the initial height H_0) and $\tau_c \simeq 5$ s. Both the characteristic time and the deformation depend on the change in voltage and on the initial voltage itself. We ensured that at least 90% of the deformation was achieved, so that H_b was reached, by waiting at least $5\tau_c$ between two changes in the setpoint (defined by t_{step}). In Fig. 6.5, we present the maximum change achieved before reaching the Taylor cone threshold. This preliminary experiment allows us to choose the value of t_{step} to guarantee $t_{step} > 5\tau_c$. Therefore, the quasi-static bubble shapes were recorded in the following experiments. Indeed, in these experiments, the changes were $\phi_{step} = 100$ V, which is smaller than that illustrated in Fig. 6.5. Under these conditions, the condition $\tau_c < 1$ s, and thus by choosing $t_{step} = 10$ s, $t_{step} > 5\tau_c$ was almost always satisfied. Therefore, the steady height H_b and radius R_b of the bubbles were measured at the end of each time step.

In Fig. 6.6, two typical measurements of $H_b(E_0)$ (when ϕ, and therefore E_0, were increased by steps as explained in Section 6.2) are reported: one on a dry surface (red points) and the other on a liquid pool (blue points). The voltage was increased in 100 V steps every 10 s from $\phi_{min} = 0$ V to $\phi_{max} = \phi_T$ [V], a voltage close to that of the onset of the Taylor cone. In both cases, $V_g = 0.25$ ml and $d = 25$ mm. Pictures (i) and (ii) in Fig. 6.6 show the bubbles when $E_0 = 20$ V/mm in both situations. Pictures (iii) (resp. (iv)) illustrate the deformation of the bubble resting on a solid when $E_0 = 460$ V/mm (resp. floating on a liquid when $E_0 = 520$ V/mm). Two major differences can be noticed. Firstly, the bubble height H_b is substantially smaller for a floating bubble, even without any applied field. Secondly, to obtain the same deformation D on a floating bubble, it is necessary to apply a stronger field (that is to say, a stronger voltage).

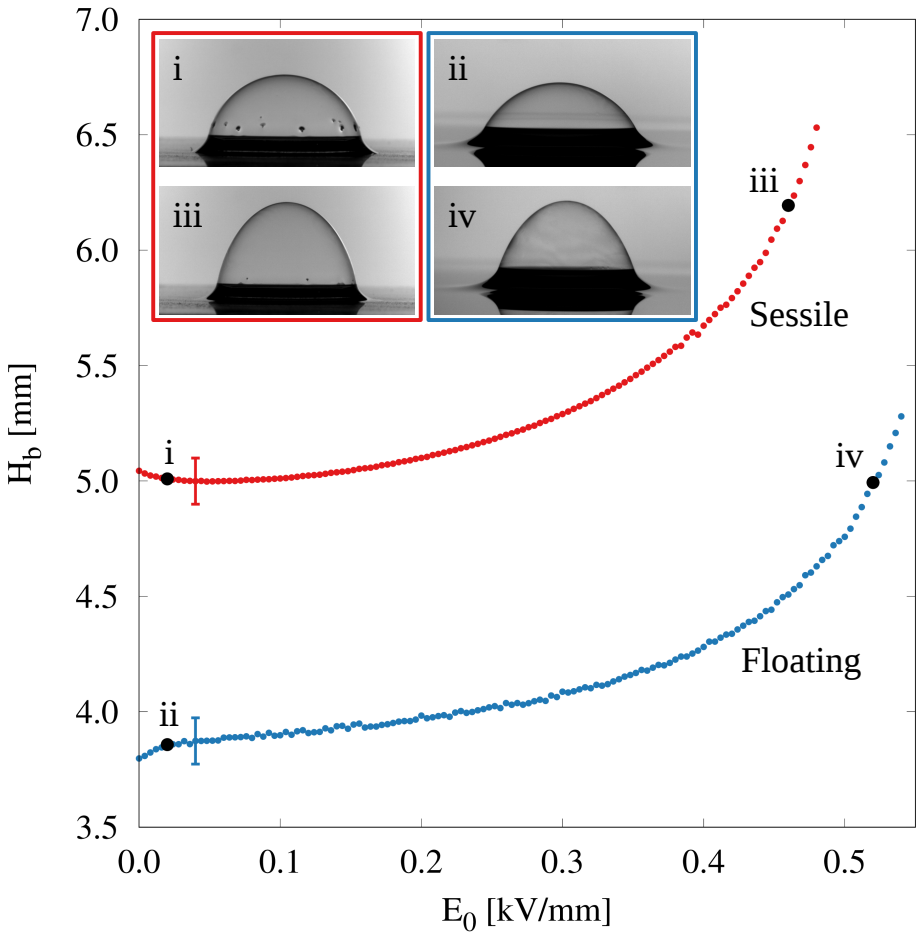

Figure 6.6: Stationary height of the bubbles H_b at different intensity values of the applied field E_0. Both curves correspond to bubbles of $V_g = 0.25$ ml and to a capacitor of $d = 25$ mm. The red and blue points represent respectively a bubble on a solid and liquid substrate. Pictures (i) and (ii) illustrate the shape of a bubble under $E_0 = 20$ V/mm for a solid (i) and a liquid (ii) substrate. Pictures (iii) and (iv) show the deformation of bubbles resting respectively on a solid under $E_0 = 460$ V/mm and floating on a liquid under $E_0 = 520$ V/mm. A typical error bar, corresponding to the worst-case scenario, is indicated on each curve.

6.4 Sessile Bubbles under Electric Field

Thanks to their cylindrical symmetry, the shape of sessile bubbles can be fully characterised by two geometrical parameters. We have chosen the stationary height H_b and the stationary radius measured at the top of the meniscus R_b (see Fig. 6.5). Moreover, the energy in the system comes from two contributions: the electrostatic energy due to the presence of the bubble in the electric field and the surface energy due to capillarity. As the bubble adopts a hemi-spheroidal shape, the two contributions are respectively proportional to $E_e \sim \varepsilon_0 E_0^2 R_b^3$ [J] and $E_c \sim 2 n_f \gamma R_b^2$, with n_f the number of interfaces. Consequently, H_b can be expressed in terms of five dimensional governing parameters, which are R_b, γ, n_f, ε_0 and E_0. Four of them have independent dimensions and the dimension of the fifth can be expressed as a product of the others. If the dimension of ε_0 is chosen as the dependent one, it can be formulated as follows

$$[\varepsilon_0] = [\gamma][n_f][R_b]^{-1}[E_0]^{-2}. \tag{6.4}$$

The dimension of H_b can also be expressed as a product of the dimensions of the same four dimensional parameters. Therefore, the following relation can be written according to dimensional analysis and Buckingham Π-theorem [132]:

$$\mathrm{Ar}_s = f_s(\mathrm{Bo}_{e,s}) \tag{6.5}$$

with $\mathrm{Ar}_s = H_b/R_b$ the aspect ratio and $f_s(\mathrm{Bo}_{e,s})$ a function of $\mathrm{Bo}_{e,s}$ the energy ratio, *i.e.* the electrical Bond number which can be written as

$$\mathrm{Bo}_{e,s} = \varepsilon_0 E_0^2 R_b / 4\gamma. \tag{6.6}$$

The factor 4 in $\mathrm{Bo}_{e,s}$ comes from E_c and must be taken into account since we have two interfaces ($n_f = 2$) and a cylindrical symmetry. This definition is similar to that of Basaran [104].

In Fig. 6.7, the aspect ratio Ar_s is plotted as a function of $\mathrm{Bo}_{e,s}$ in the dry case. Three capacitor sizes and three internal volumes are presented. On top of that, data obtained by Basaran *et al.* [104] are represented (black bullets). Both results are very similar even though we used smaller bubbles (three to five times smaller) and capacitors (three to six times smaller). This good agreement between all the results over

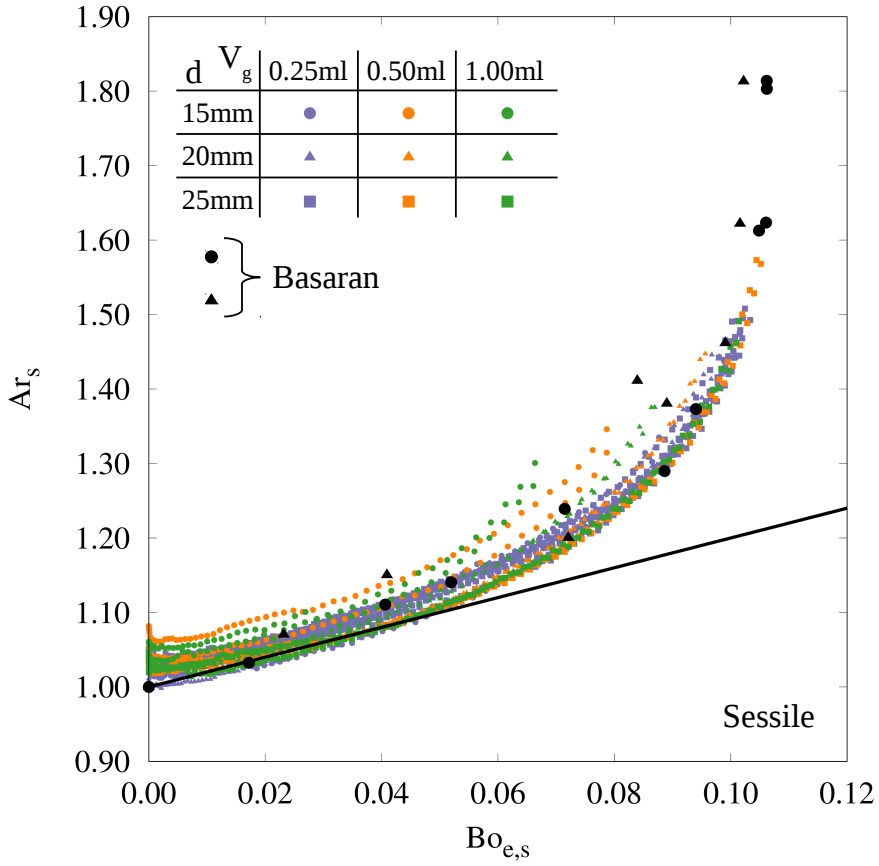

Figure 6.7: Aspect ratio of sessile bubbles $\mathrm{Ar}_s = H_b/R_b$ resting on a dry solid plate plotted as a function of the energy ratio $\mathrm{Bo}_{e,s} = \varepsilon_0 E_0^2 R_b/4\gamma$. Three sizes of capacitors d were used: $d = 15$ mm (solid circles), 20 mm (solid triangles) and 25 mm (solid squares), as well as three internal volumes V_g: $V_g = 0.25$ ml (in lilac), 0.50 ml (in orange) and 1.00 ml (in green). The black bullets represent the data presented in Ref. [104] for a capacitor of $d = 85.5$ mm and an approximate internal volume of $V_g = 35.14$ ml (solid circles) or $V_g = 30.05$ ml (solid triangles). The black straight line corresponds to the law for small deformations adapted from Eq. 3.8. On this and the following graphics, the error bars are smaller than the bullets.

a wide range of parameters indicates that the shape of sessile bubbles is fairly well grasped by $\mathrm{Ar}_s(\mathrm{Bo}_{e,s})$. In addition, the energy ratio $\mathrm{Bo}^*_{e,s}$ required to trigger the bubble instability (*i.e.* to initiate the Taylor cone) is the same in all cases. Finally, the small deformations are well predicted by the law $\mathrm{Ar}_s = 1 + 9/4\ \mathrm{Bo}_{e,s}$, adapted from Eq. 3.8 [104] (black solid line in Fig. 6.7).

6.5 Floating Bubbles under Electric Field

As mentioned in Section 6.3, there are two major differences between a bubble resting on a dry solid plate and a bubble floating on a liquid bath when subjected to an electric field. This is essentially due to the pinning of the contact line and the partial immersion. This is discussed on the basis of Fig. 6.8, which presents the aspect ratio $\mathrm{Ar}_s = H_b/R_b$ for floating (in green, orange and lilac) and sessile (represented with red circles for all sets of parameters) bubbles as a function of $\mathrm{Bo}_{e,s}$. The first difference is that the bubble height H_b, and therefore the aspect ratio Ar_s, are substantially smaller for floating bubbles, even without any applied field. The second is the necessity to apply a higher field, and thus to reach higher $\mathrm{Bo}_{e,s}$, to obtain the same deformation D on floating bubbles.

The aspect ratio measurement must be adapted to the case of floating bubbles. Indeed, as explained in Section 5.2, the characteristic radius of curvature is R_c, which differs from R_b due to the initial contact angle $\theta \sim 60°$. Since the capillary energy directly depends on R_c, the energy ratio for floating bubbles is rewritten as $\mathrm{Bo}_e = \varepsilon_0 E_0^2 R_c/4\gamma$ and, accordingly, the aspect ratio $\mathrm{Ar}_f = H_b/R_c$ as well. Furthermore, as presented in Section 5.2, the initial aspect ratio $\mathrm{Ar}_f(E_0 = 0)$ directly depends on the buoyancy Bond number Bo_b of the bubble, and thus on its size. These initial aspect ratios have already been rationalised by Teixeira *et al.* [8] and are summarised in Table 5.1.

All the bubbles used in our experiments have a size corresponding to a moderate $\mathrm{Bo}_b \sim 10$ and therefore belong to the intermediate regime presented in Section 5.2. This means that both the immersed and emerged parts of the bubbles have an impact on the bubble shape and cannot be neglected. The immersed part of the bubble represents

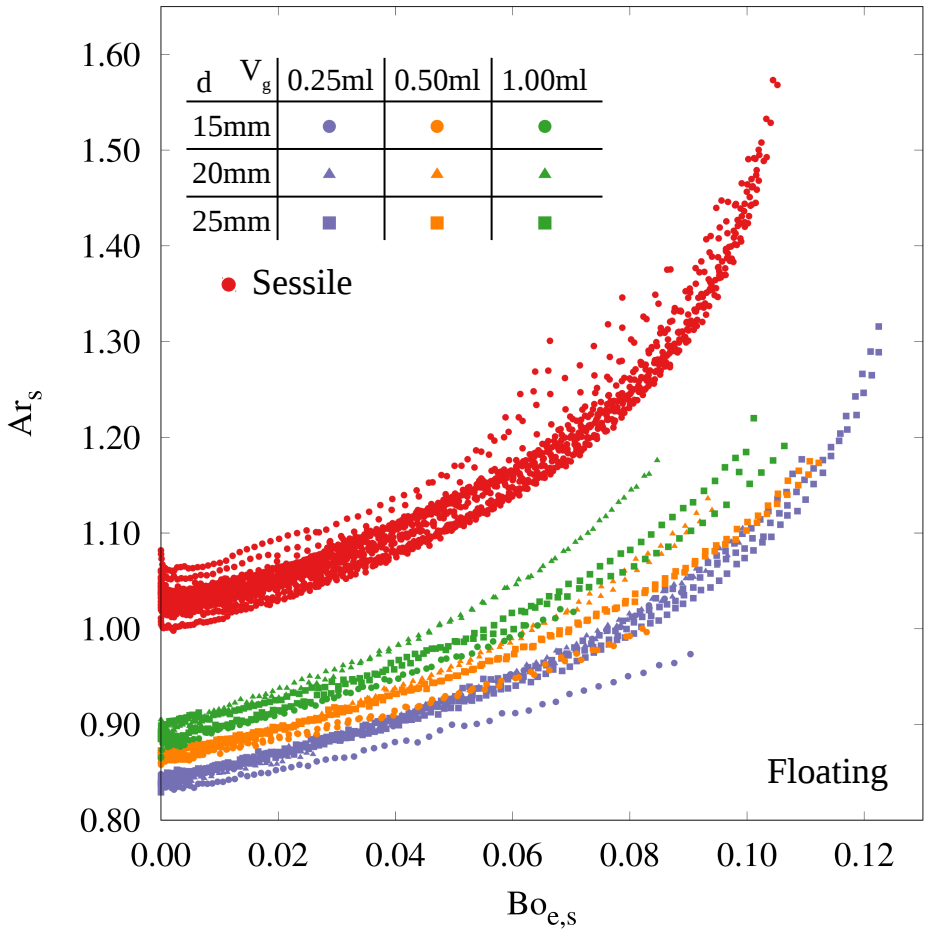

Figure 6.8: Aspect ratio of floating bubbles $\mathrm{Ar}_s = H_b/R_b$ as a function of the energy ratio $\mathrm{Bo}_{e,s} = \varepsilon_0 E_0^2 R_b/4\gamma$. The same three sizes of capacitors d had been used: $d = 15$ mm (solid circles), 20 mm (solid triangles) and 25 mm (solid squares), as well as the same three internal volumes V_g: $V_g = 0.25$ ml (in lilac), 0.50 ml (in orange) and 1.00 ml (in green). The results for bubbles resting on a solid substrate, namely for the three V_g and three d considered, are drawn for the sake of the comparison (red solid circles).

about 31% for a bubble of $V_g = 0.25$ ml ($\mathrm{Bo}_b \approx 9.92$) to 22% for a bubble of $V_g = 1$ ml ($\mathrm{Bo}_b \approx 15.46$) (see Table 5.1).

Due to the presence of an immersed interface, the energies responsible for the behaviour of the system must be reconsidered. Indeed, for a bubble on a dry solid, there are only two interfaces that contribute equally to the capillary energy ($n_f = 2$ for a sessile bubble). For floating bubbles, there is an additional interface between the liquid pool and the immersed part of the bubble. In general, this interface has its own radius of curvature R_i. Consequently, if we assume that the immersed interface is well described by a unique R_i, the capillary energy is given by $E_c \sim (2n_f\gamma/R_c)V_f + (2n_i\gamma/R_i)V_i$. In this expression, the parameters describing the immersed part of the bubble R_i, V_i and n_i (with $n_i = 1$) correspond respectively to those of the emerged part R_c, V_f and n_f (with $n_f = 2$). Although the shape of the emerged part is a spheroidal cap and $V_f \sim R_c^3$, this is generally not the case for the immersed part. However, as shown by Teixeira *et al.* [8], the shape of the immersed part of a floating bubble is completely described by Bo_b. Hence, if γ, ρ and g are constant, the immersed shape of the bubble is a complex function of R_c. Therefore, the capillary energy of a floating bubble can be written as follows

$$E_c \sim 2\gamma R_c^2(2 + \xi(R_c)), \tag{6.7}$$

where $\xi(R_c) \sim V_i/(R_i R_c^2)$ is a dimensionless function describing the relative importance of the immersed part compared to the emerged one.

As explained in Section 5.2, the shape of the intermediate sized bubbles is almost symmetric around a horizontal plane just below the top of the meniscus. Consequently, ξ is approximately equal to one (as $R_i \approx R_c$ and $V_i \approx V_f$) and we assume that each interface brings the same amount of capillary energy, which is reasonably approximated by $E_c \sim 2n\gamma R_c^2$, with $n = n_f + n_i = 3$ the total number of interfaces.

Let us now consider the electrostatic energy due to the presence of the bubble in the electric field. It is similar for solid and liquid substrates. Indeed, $E_e = -\vec{P}.\vec{E_0}/2$ with $\vec{P}$ [C m] the dipole moment due to the electric field $\vec{E_0}$. The charges are located on the outer faces of both floating and sessile bubbles since they act as perfect conductors and therefore behave like Faraday cages. Consequently, there is no field in the bubbles and no charge along the inner faces. Moreover, $\vec{P} = \alpha\vec{E_0}$,

with α [C^2 m/N] the polarizability. On the one hand, for a conducting hemisphere, $\alpha = 3\varepsilon_0 V_f$ with $V_f = V_g$ the volume of the hemisphere. On the other hand, for a very thin conducting spherical cap ($\mathrm{Ar}_f \ll 1$ and $\varepsilon \gg \varepsilon_0$), $\alpha = \varepsilon_0 V_f$ [133][3]. The floating bubble shape lies between the hemisphere and the thin spherical cap, but their aspect ratio close to one (see Table 5.1) should make α close to that of a hemisphere. At first sight, E_e can then be assumed independent of the shape. Therefore, the electrostatic energy is well approximated by $E_e \sim \varepsilon_0 E_0^2 R_c^3$.

With the knowledge of these specificities linked to the liquid substrate, a new dimensional analysis can be performed to describe the shape of both floating and sessile bubbles. In addition to the five initial dimensional governing parameters used previously (see Eq. 6.4), we now add those detailed in the last paragraphs. This leads to defining H_b as a function $f(R_c, \gamma, n, \varepsilon_0, E_0, g, \rho)$. Only five of these seven parameters have independent dimensions. Besides ε_0, the dimension of any other parameter can be expressed as a product of the dimension of the remaining ones. If the dimensions of ε_0 and ρ are chosen as dependent, they can be formulated as follows

$$[\varepsilon_0] = [\gamma][n][R_c]^{-1}[E_0]^{-2}[g]^0, \tag{6.8}$$

$$[\rho] = [\gamma][n][R_c]^{-2}[E_0]^0[g]^{-1}. \tag{6.9}$$

The dimensions of H_b can also be expressed as a product of the dimensions of the same five dimensional parameters. Then, according to dimensional analysis and the Buckingham Π-theorem [132], the following relation holds

$$\mathrm{Ar}_f = f(\mathrm{Bo}_b, \mathrm{Bo}_e) \tag{6.10}$$

with $\mathrm{Ar}_f = H_b/R_c$ the aspect ratio and $f(\mathrm{Bo}_b, \mathrm{Bo}_e)$ a function of both Bo_b, the buoyancy Bond number obtained from Eq. 6.9 (and equivalent to Eq. 5.2) and Bo_e, the electrical Bond number define by Eq. 6.8. The Bond numbers, Bo_b and Bo_e, which respectively describe the competition between the gravitational and capillary energies and the competition between the electric and capillary energies, can be written as

[3]The assumption on the particle size in Ref. [133] is satisfied because the external electric field is constant.

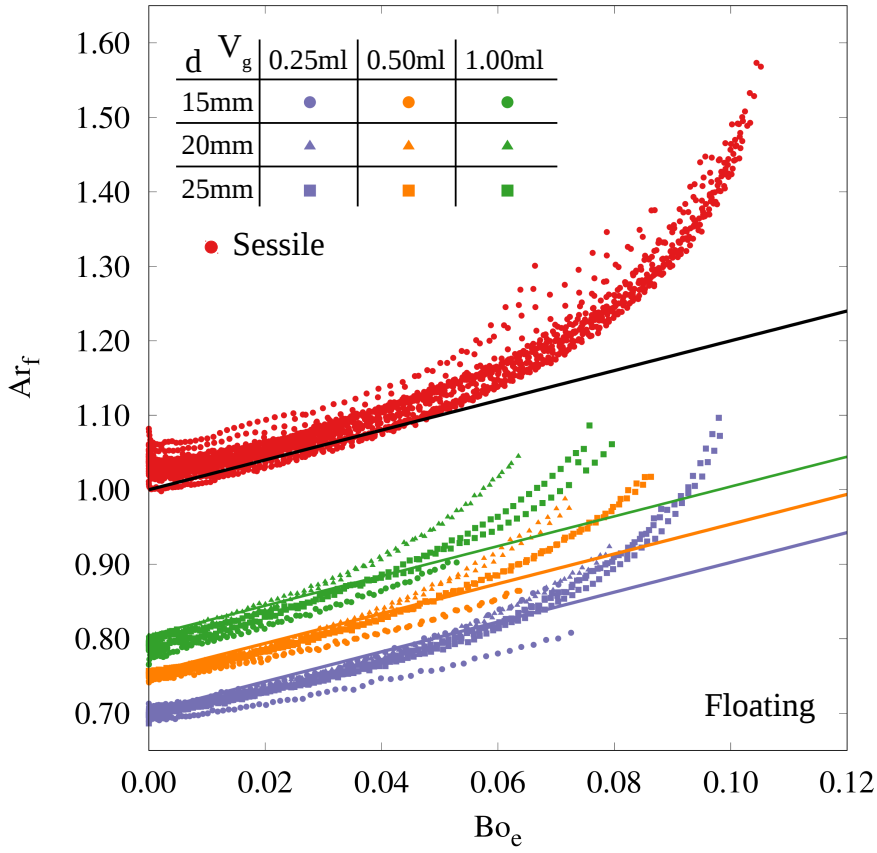

Figure 6.9: Aspect ratio of the floating bubbles $\mathrm{Ar}_f = H_b/R_c$ drawn as a function of the energy ratio $\mathrm{Bo}_e = \varepsilon_0 E_0^2 R_c/2n\gamma$. The same three sizes of capacitors d were used: $d = 15$ mm (solid circles), 20 mm (solid triangles) and 25 mm (solid squares), as well as the same three internal volumes V_g: $V_g = 0.25$ ml (in lilac), 0.50 ml (in orange) and 1.00 ml (in green). The straight lines correspond to Eq. 6.13 describing the small deformations. The colour of each line is related to the corresponding V_g and the only fitting parameter for each curve is the aspect ratio in absence of field. The results for bubbles resting on a solid substrate (red solid circles) as well as the corresponding law (black straight line) are drawn for the sake of comparison.

follows

$$\mathrm{Bo}_b = g\rho R_c^2/\gamma, \tag{6.11}$$

$$\mathrm{Bo}_e = \varepsilon_0 E_0^2 R_c/2n\gamma. \tag{6.12}$$

It should be noted that $n = 1$ in Bo_b (and has therefore been omitted) because Bo_b takes into account a fully immersed bubble.

Although the function $f(\mathrm{Bo}_b, \mathrm{Bo}_e)$ is complex in general (*i.e.* for floating bubbles at any Bo_b), observations made on the energies suggest that the function may be simpler in specific cases (*i.e.* for floating bubbles of intermediate Bo_b). To ascertain this insight, the data from Fig. 6.8 are presented in Fig. 6.9 as a relationship between Ar_f and Bo_e, for both bubbles resting on solid (in red) and floating on liquid (in green, orange and lilac) substrates. As expected, the initial aspect ratio depends only on the size of the bubble, which is represented in Eq. 6.10 by the Bo_b. A linear law inspired by (3.8) is best adjusted with:

$$\mathrm{Ar}_f(\mathrm{Bo}_b, \mathrm{Bo}_e) = A(\mathrm{Bo}_b) + \frac{9}{4}\mathrm{Bo}_e, \tag{6.13}$$

where $A(\mathrm{Bo}_b) = \mathrm{Ar}_f(\mathrm{Bo}_b, \mathrm{Bo}_e = 0)$, the only free fitting parameter, is related to the initial aspect ratio. The corresponding laws, with $n = 3$, are drawn in Fig. 6.9 for each size of floating bubbles in the corresponding colour. For sessile bubbles, the $\mathrm{Ar}_f = 1 + 9/4\ \mathrm{Bo}_e$ law with $n = 2$ (similar to that used in Fig. 6.7) is also represented by a solid black line for comparison. The $\mathrm{Ar}_f(\mathrm{Bo}_b, 0)$ found are in fairly good agreement with those predicted [8] (see Table 5.1). Moreover, for the range of bubble sizes studied, the changes in aspect ratio due to E_0 are similarly described, for both floating and sessile bubbles, by the newly defined energy balance Bo_e. This is particularly clear when sessile bubbles (in red) and floating bubbles of $V_g = 0.25$ ml (in lilac) are compared in Fig. 6.9. For example, the energy ratio required to trigger the Taylor cone, Bo_e^*, is the same in both cases. This value is defined as that at which Ar_f begins to diverge. Furthermore, the linear correlation given by Eq. 6.13 leads to good approximations of our results when the deformations are small.

In Fig. 6.10, the variation of the aspect ratio $\Delta\mathrm{Ar}_f = \mathrm{Ar}_f(\mathrm{Bo}_e, \mathrm{Bo}_b) - \mathrm{Ar}_f(\mathrm{Bo}_b, 0)$ is drawn as a function of Bo_e for both sessile (in red) and

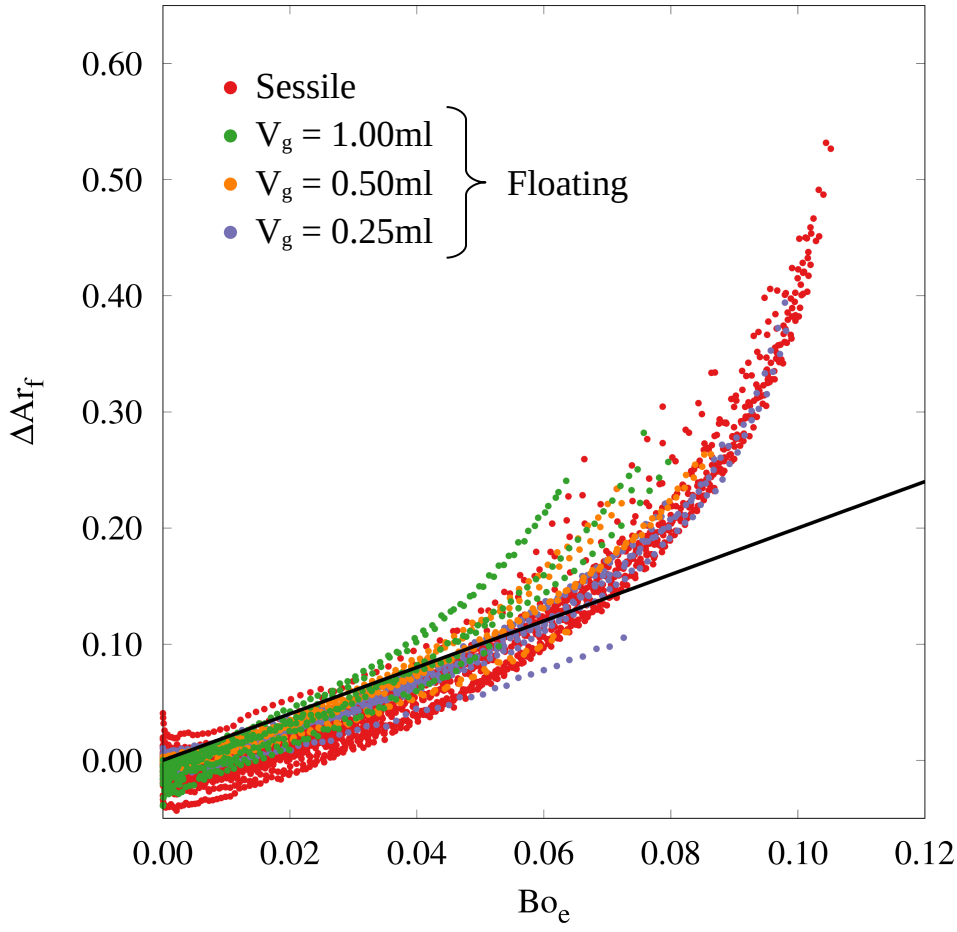

Figure 6.10: Variation of the aspect ratio $\Delta \mathrm{Ar}_f = H_b/R_c - \mathrm{Ar}_f(\mathrm{Bo}_b, 0)$ of sessile (in red) and floating (in green, orange and lilac) bubbles drawn as a function of the energy ratio $\mathrm{Bo}_e = \varepsilon_0 E_0^2 R_c/2n\gamma$. The same three internal volumes V_g: $V_g = 0.25$ ml (in lilac), 0.50 ml (in orange) and 1.00 ml (in green) were used. The straight line corresponds to the law (6.15) describing small deformations.

floating (in green, orange and lilac) bubbles. The $\Delta \mathrm{Ar}_f$ are obtained by subtracting the $A(\mathrm{Bo}_b)$ corresponding to each data set. In so doing, all the data collapse on a single master curve allowing us to write:

$$\mathrm{Ar}_f(\mathrm{Bo}_b, \mathrm{Bo}_e) = A(\mathrm{Bo}_b) + f_s(\mathrm{Bo}_e) \tag{6.14}$$

with $A(\mathrm{Bo}_b)$ a function of Bo_b, which fully describes the initial shape of the bubbles (obtained by adjusting Eq. 6.13) and $f_s(\mathrm{Bo}_e)$ a function of Bo_e which describes how these initial shapes are modified by the electric field (see Eq. 6.5).

Eq. 6.13 corresponds to a function represented by Eq. 6.14 and can be rewritten to be plotted in Fig. 6.10 as follows

$$\Delta \mathrm{Ar}_f(\mathrm{Bo}_e) = \frac{9}{4}\mathrm{Bo}_e. \tag{6.15}$$

Eq. 6.15 approximates all data for small deformations, as shown by the solid black line in Fig. 6.10. Consequently, the deformation of both sessile and floating bubbles under an applied uniform electric field is in general described by a function of the form defined by Eq. 6.10. This function (6.13) is determined in the linear, or weak fields, regime (*i.e.* for $\mathrm{Bo}_e < 0.05$) in the case of the experiments described in this thesis (namely for floating bubbles of intermediate Bo_b and $\xi \approx 1$.)

6.6 Effect of the Field on the Meniscus

The description of the bubble shape under an electric field presented above stated that the initial shape of the bubbles is a spherical cap. However, as presented in Section 5.1, there is an accumulation of liquid at the bubble base forming the meniscus. Due to this meniscus, the initial bubble shape slightly departs from the perfect spherical cap. Even if the shape is well described under the spherical cap assumption, the meniscus has an important impact on the charge distribution and thus on the electric field required to obtain this given shape.

Like the initial shape, the meniscus is greatly influenced by the substrate as well as by the bubble size (via the Bo_b as shown by Teixeira *et al.* [8]). However, unlike the shape, the meniscus itself does not seem

to be directly influenced by the electric field. Measurements made on floating bubbles indicate that it has a constant height (predicted as a function of Bo_b [8]) whatever the electric field. On the contrary, for sessile bubbles, the meniscus height slightly decreases as the electric field increases. This was expected as the deformation of a hemispherical bubble is necessarily accompanied by an increase in its surface. Consequently, liquid is needed to fuel the interface creation. This is not observed for floating bubbles since the required liquid is pumped into the liquid tank. This observation is related to that made by Macky [10] on the lifetime of a bubble undergoing a Taylor cone. The absence of a direct effect on the meniscus height can be understood through the charge distribution at the interface. Indeed, as Harris *et al.* numerically showed in [134], the charge distribution in the vicinity of the top of the meniscus (and therefore near the base of the hemisphere or spherical cap formed by the bubble) is vanishing for any electric field.

Although it carries only a small amount of charge, the meniscus has an effect on the general charge distribution of the bubble. Indeed, Basaran *et al.* [104] numerically demonstrated the effect of the dimensionless droplet size parameter (namely the signed distance between the centre of the sphere formed by the droplet and the bottom electrode) on the critical electrical Bond number Bo_e^*. In our experiments, for floating bubbles of $V_g = 0.25$ ml, the Bo_e^* is close to 0.12 (see Fig. 6.8). Yet, in [104], the predicted value of Bo_e^* is almost equal to 0.26 , for a droplet with a droplet size parameter equal to -0.5 (which corresponds to the shape of a $V_g = 0.25$ ml bubble). This is more than twice what was observed during the experiments. Consequently, the good agreement between our experimental results and those presented in [104] illustrated in Fig. 6.7, indicates that the deformation of bubbles under electric field is correctly predicted, but for smaller Bo_e than theoretically expected. The corrections to the capillary energy cannot explain this discrepancy, but the presence of the meniscus could. In order to validate this insight on the origin of the difference, we can draw inspiration from the study carried out by Harris *et al.* [134] on the effect of a nozzle on a hanging droplet. Indeed, they showed that the nozzle increases the total charge carried by the droplet even when d is kept constant and when the charge directly carried by the nozzle itself is

small. As a consequence, the value of Bo_e^* decreases. Comparatively, the meniscus also carries a small amount of charge, but its shape is more complex than that of a cylindrical nozzle. Yet, although a direct and quantitative parallel is impossible due to the difference in shape, a qualitatively similar effect of the meniscus on the total charge carried could be conjectured. Accordingly, the presence of a meniscus at the base of the bubbles should reduce the Bo_e^* and explain the discrepancy between the numerical predictions [104] and the experimental results presented here.

The complete determination of the function describing the deformation of the bubbles under the effect of an applied uniform electric field should thus involve an analysis similar to that proposed in Ref. [134], but with a meniscus-shaped nozzle. However, unlike cylindrical nozzles, the meniscus has a shape imposed by the Bo_b [8]. This means that it is not necessary to add another element (and its related dimensionless number) to fully describe the system. Hence, the dimensional analysis and Eq. 6.10 remain valid albeit the meniscus effect is added to the study.

6.7 Frustrated Bubbles

Up to there, the liquid pool depth e was sufficiently large not to influence the bubble shape. Varying e may reveal a transition between floating and sessile bubbles and therefore, highlight the effect of the immersed interface on the bubble deformation by partially suppressing it. Indeed, as floating bubbles have an immersed part, they also have a natural penetration length h into the liquid as represented in Fig. 6.2 (b). If the depth e becomes smaller than h, then the bottom electrode reaches the immersed interface and substitutes a part of this interface with a flat surface (solid if the liquid dewets the surface, liquid otherwise). The bubble becomes frustrated. Consequently, a smaller amount of energy is required to oppose the capillary energy. Therefore, at a given electric field, the deformation D should be larger. As explained in Section 6.2, the depth e was controlled by changing the position of the bottom electrode. For smaller fluid layer thicknesses, *i.e.* $e \leq 0.20$ mm, the bubbles tend to move on the surface of the bath and have to be immobilised us-

ing, for example, a nylon thread (since the threads are mostly immersed in the pool, they have no visible effect on the bubble dynamics).

Since the penetration depth of the bubble is no longer prescribed by Bo_b, but by an independent dimensional parameter e, a third dimensionless number is needed to describe the system. If the dimensionless penetration depth e/R_c is chosen, the shape of the bubble is fully described by

$$\mathrm{Ar}_f = f_f(\mathrm{Bo}_b, \mathrm{Bo}_e, e/R_c) \tag{6.16}$$

with $\mathrm{Ar}_f = H_b/R_c$ the aspect ratio and $f_f(\mathrm{Bo}_b, \mathrm{Bo}_e, e/R_c)$ a function of $\mathrm{Bo}_b = g\rho R_c^2/\gamma$, the buoyancy Bond number defined by Eq. 6.9, $\mathrm{Bo}_e = \varepsilon_0 E_0^2 R_c/2n\gamma$, the electrical Bond number defined by Eq. 6.8 and e/R_c the dimensionless penetration depth.

Fig. 6.11 illustrates the aspect ratio Ar_f as a function of the energy ratio Bo_e. Bubbles of $V_g = 0.25$ ml, with a predicted $h = 1.38$ mm [8], which was the largest achieved out of the three considered volumes, were measured using a capacitor of $d = 25$ mm. The blue and red points correspond to the two limiting cases: deep liquid bath and solid surface, respectively. Measurements are sorted into three groups and are represented by a colour gradient between blue and red. The bluest category corresponds to that which is closest to floating bubbles: $e \geq 1.25$ mm. Conversely, the reddest category represents the group with the lowest liquid depth: $e \leq 0.20$ mm. Finally, the third category corresponds to $e \approx 0.50$ mm.

The non-frustrated bubbles, with $e \geq 1.25$ mm, deform exactly like those in a deep liquid bath. Indeed, the bubbles from this category have a h smaller than or close to e and thus no significant change in shape is observed. In contrast, the bubbles on which the effect of frustration is most noticeable are those belonging to the group with $e \leq 0.20$ mm. Firstly, the adjusted initial aspect ratio A, observable in Fig. 6.11, becomes larger as the liquid depth decreases. Indeed, since the bottom electrode presses the lower part of the bubble, its immersed volume is reduced. Consequently, as the total volume V_g is constant, the emerged volume increases, and so does the aspect ratio. Secondly, in order to obtain the same deformation as for a non-frustrated bubble, smaller values of E_0 and consequently of Bo_e are needed. This is especially visible in the energy ratio required to initiate the Taylor cone Bo_e^* (defined as

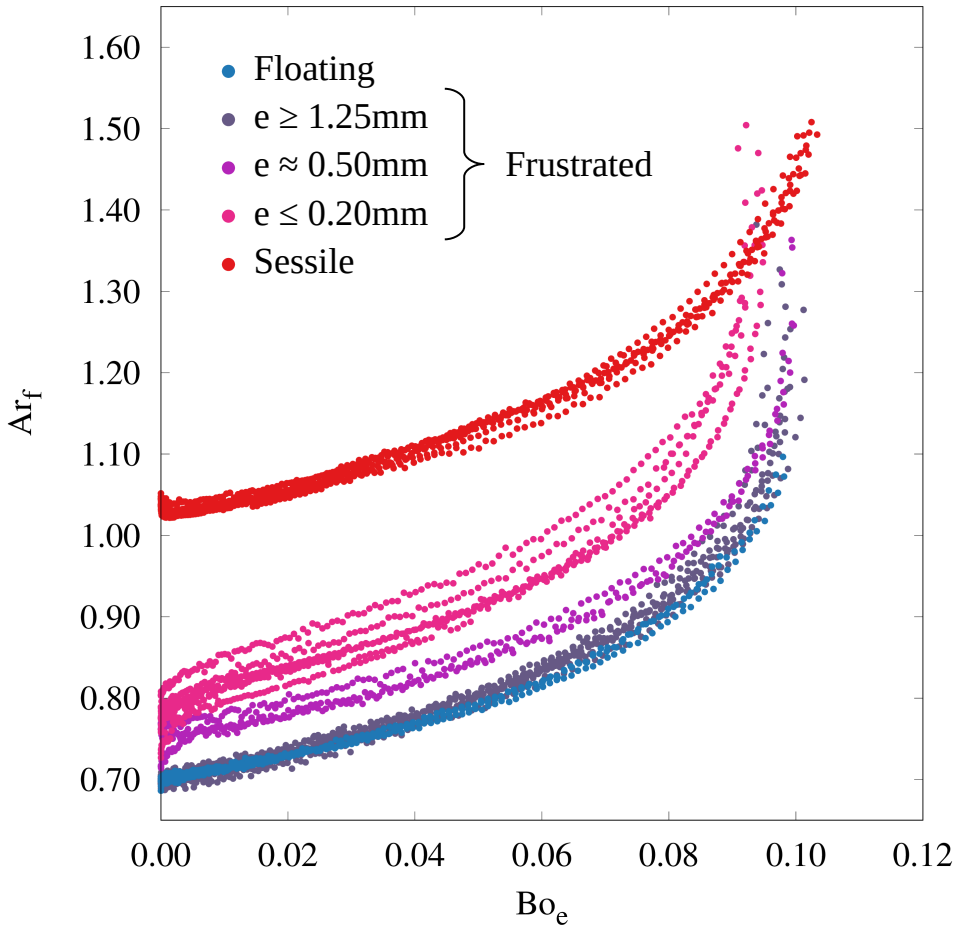

Figure 6.11: Aspect ratio of the frustrated bubbles $\mathrm{Ar}_f = H_b/R_c$ drawn as a function of the energy ratio $\mathrm{Bo}_e = \varepsilon_0 E_0^2 R_c/2n\gamma$ for different liquid depths e. The size of the capacitor is fixed at $d = 25$ mm and the internal volume at $V_g = 0.25$ ml. The blue and red circles correspond respectively to the liquid and solid results in the same situation. The different results are sorted into three categories and are represented by a colour gradient between blue and red. From the bluest to the reddest: $e \geq 1.25$ mm, $e \approx 0.50$ mm and $e \leq 0.20$ mm.

the value at which Ar_f begins to diverge). This effect is mainly due to an overestimation of the capillary energy. Indeed, the contribution of each interface to the capillary energy is estimated assuming spheroidal cap shapes. However, a substantial part of the immersed interface is replaced (in case of dewetting, which appears to be the case) or flattened (otherwise) by the flat bottom electrode. Consequently, the capillary energy due to this interface is smaller. The total capillary energy calculation does not take this into account and is thus overestimated and so Bo_e is underestimated. Although the presence of a thin liquid film cannot be completely excluded without further investigations, frustration of bubbles seems to lead to the dewetting of their lower part. This is especially noticeable when the frustrated bubbles blow up. Despite it does not affect the energy calculation, the presence of the thin film should nevertheless directly influence the mobility of the contact line. This is still an open question and further investigations are needed to address it.

In Fig. 6.11, the bubbles from the intermediate group ($e \approx 0.50$ mm) have an adjusted initial aspect ratio A between that of the most frustrated bubbles and that of the non-frustrated ones. However, for $\mathrm{Bo}_e \rightarrow \mathrm{Bo}_e^*$, the values of Ar_f are close to those of non-frustrated bubbles at a given Bo_e. Moreover, they have the same Bo_e^*. This transition from a behaviour between the most frustrated and non-frustrated bubbles to another similar to that of non-frustrated bubbles is likely due to the decrease of the immersed surface influenced by the flat solid electrode. Indeed, when the bubble is deformed by an electric field, besides the increase in height H_b, there is also a shrinkage of R_b and thus a decrease in R_c. This leads to the decreasing of the fraction of the immersed surface frustrated by the bottom electrode. Therefore, the approximate contribution of the immersed interface to the capillary energy approaches the exact one.

If we analyse the behaviour of frustrated bubbles, we observe that, no matter how small e is, the frustrated bubbles behave more like floating bubbles than sessile ones. Indeed, the adjusted initial aspect ratio A of the most frustrated bubbles differs from that of a sessile bubble. This means that even a small liquid thickness e is enough to change from a hemispherical shape with $\theta = 90°$ (characteristic of sessile bubbles) to

a spherical cap shape with $\theta \sim 60^\circ$ (characteristic of floating bubbles of $V_g = 0.25$ ml). This is due to the mobility of the contact line of the floating bubbles, which is pulled outwards by the surrounding liquid. The behaviour of these frustrated bubbles illustrates the strong impacts of the immersed interface on the energy ratio and the mobility of the contact line on the adjusted initial aspect ratio A. Besides the intrinsic differences between sessile and floating bubbles, our study confirms that the energy formulation and the aspect ratio must be adapted to take into account the immersed interface and the contact line mobility of a floating bubble.

6.8 Conclusion

The deformations of soap bubbles under a vertically applied uniform electric field induced by a plane capacitor were measured when the bubble rests on a solid substrate or floats on a pool of its own soap (see Fig. 6.6). As mentioned in the previous chapter, sessile and large floating bubbles ($\mathrm{Bo}_b > 100$ [8]) are hemispherical and have a flat bottom interface when no electric field is applied. The aspect ratio of sessile bubbles under weak fields evolves according to a linear law represented by Eq. 3.8 from [104] (see Fig. 6.7). This linear relationship holds for $\mathrm{Bo}_e < 0.05$, which defines the weak fields limit. Due to their similar initial shape as well as the negligible influence of their immersed part, large floating bubbles should be described in an equivalent way. However, the floating bubbles belonging to the intermediate regime ($2 < \mathrm{Bo}_b < 100$ [8]) initially form a spherical cap with an angle at the top of the meniscus close to $\theta \sim 60^\circ$. Moreover, the presence of a third curved interface between the soap bath and the floating bubble must be taken into account in the energy calculation. By modifying the definition of the aspect ratio and that of the capillary energy to consider the initial bubble shape and the third interface respectively, the floating and sessile bubbles are similarly described when deformed by an applied uniform electric field (see Fig. 6.9). In particular, all deformations under weak fields (*i.e.* $\mathrm{Bo}_e < 0.05$) are predicted by a law inspired by Eq. 3.8 (see Fig. 6.10). We also discussed the role of the meniscus: its presence greatly influences the overall charge distribution on the bubble, notably

modifying the critical electrical Bond number Bo_e^*, even if the electric field has no direct influence on it. Finally, to prove the robustness of our analysis, the influence of the immersed interface was further explored by controlling the liquid depth to frustrate the floating bubbles (see Fig. 6.11).

These conclusions confirm the validity of the intuition based on the superficial nature of the forces involved and the resulting parallel between the behaviour of bubbles and droplets under uniform vertical electric fields. Indeed, beyond the qualitative similarity of shape presented in Fig. 1.2, the law represented by Eq. 3.8 from [104] predicted the aspect ratio of both bubbles and droplets under weak fields, with the amendments just described. However, these adjustments are precisely the expression of the bubble specificities. In particular, the mobility provided by the presence of the soap pool has a crucial impact on the bubble shape, even when the immersed part is almost completely removed. Furthermore, the presence of the meniscus at the bubble base completely changes the overall charge distribution and induces a much lower critical electric field. Yet, its shape is not directly modified upon the application of an electric field.

Conversely, when a volume force is applied to the bubble, its meniscus deforms, forming a cylinder, leading to a clear distinction between the global shape of a bubble and that of a droplet. The next chapter (Ch. 7) is devoted to the description of the deformation of the meniscus and sessile bubbles under a uniform vertical magnetic field. Indeed, since the bubble is made of ferrofluid, the application of a uniform magnetic field induces a volume force due to the magnetic dipole present inside the ferrofluid.

7

Bubbles under Magnetic Fields

When a ferrofluid bubble is subjected to a magnetic field, its meniscus rises and forms a cylinder, which is a completely different deformation from that of a drop under the same magnetic field (see Ch. 3). This ferrofluid cylinder holds until the bubble blows up, at which point the ferrofluid separates into small droplets as a drop does when subjected to a sufficiently high magnetic field gradient [116]. This reaction means that the bubble not only forces the liquid volume into a singular shape, *i.e.* a meniscus, but also holds it together, preventing it from separating under the action of the magnetic field. The differences between the deformations of bubbles and droplets are due to their different liquid configuration and the fact that, regardless of the fluid properties, a magnetic volume effect cannot be avoided. Indeed, as the ferrofluid is uniformly distributed within a droplet, the magnetic field acts on the whole droplet. Conversely, in a bubble, most of the ferrofluid is concentrated within the meniscus and, therefore, most of the effect induced by the magnetic field takes place inside it. As with the comparison between droplets and bubbles under an electric field, this difference is presented in Fig. 1.2. Yet, ferrofluid bubbles are not the only kind of bubbles impacted by a magnetic field. Indeed, a liquid composed of particles bearing no permanent magnetic moment, namely a diamagnetic liquid (like most usual fluids), does not behave like a liquid composed of magnetic particles (*i.e.* a ferrofluid). However, whatever the liquid they are

made of, bubbles can still be manipulated with an applied magnetic field (see the section on diamagnetic bubbles in [51] for example), although a bubble or droplet made of ferrofluid has the advantage of having a very large response to the magnetic field compared to their diamagnetic counterparts.

In this chapter, we study the deformation undergone by a ferrofluid bubble under a homogeneous magnetic field. First, we highlight the specificity of the bubble's liquid distribution. Then, the experimental set-up as well as the method used to study the deformation are presented. Next, the overall steady shape of the bubble is studied to determine what hypotheses can be made to describe the deformation. Through this analysis and its conclusions, we rationalise the meniscus deformation, which is responsible for the deformation of the whole bubble. These observations are finally summarised in a conclusion to put them into the context of this thesis.

7.1 The Crucial Role of the Meniscus

As developed in Section 3.3, the magnetic field tends to align the magnetic moments $\vec{m}$ inside a liquid volume. Moreover, a magnetic gradient as well as magnetostrictive effects can induce a net force on the moments $\vec{m}$. In addition, as we seek to describe the static shape of the bubble, the speed term in Eq. 3.10 is null and the pressure equilibrium inside the ferrofluid under a field $\tilde{H}$ is written as follows

$$P_l + \mu_0 \int_0^{\tilde{H}} \left[\nu \frac{\partial M}{\partial \nu}\right]_{\tilde{H^*},T} \mathrm{d}\tilde{H^*} + \rho g z = \mathrm{cst}, \tag{7.1}$$

with the following boundary condition:

$$P_l + \underbrace{\mu_0 \int_0^{\tilde{H}} \left[\nu \frac{\partial M}{\partial \nu}\right]_{\tilde{H^*},T} \mathrm{d}\tilde{H^*}}_{P_{m,s}} + \underbrace{\mu_0 \int_0^{\tilde{H}} M \mathrm{d}\tilde{H^*}}_{P_{m,i}} + \underbrace{\frac{\mu_0}{2} M_n^2}_{P_{m,n}} = P_0 + P_\gamma, \tag{7.2}$$

with z the liquid depth and M its magnetisation. These equations are applicable everywhere inside the ferrofluid forming the bubbles but, since

the magnetic effects are directly related to the liquid volume, the most important manifestations take place where the liquid volume is concentrated, namely the meniscus. Finally, since we are not interested in compression phenomena, we assume an incompressible ferrofluid: the magnetostrictive term in Eq. 7.1 and Eq. 7.2 can be discarded without any consequence[1].

To analyse the deformation of the bubble meniscus, a sessile bubble resting on a microscope cover slip is used (see Fig. 7.1 (a)). As explained in Ch. 5, in such a situation the meniscus shape is defined by the surface tension/gravity competition and can be related to the capillary length. When we apply a uniform magnetic field, the meniscus height grows, changing the shape of the meniscus. Furthermore, the meniscus height increases as the intensity of the applied field does (see Fig. 7.1: $B_0 =$ 11.07 mT in (b) and $B_0 = 41.22$ mT in (c)). The shape of the meniscus is thus a competition between gravity, capillarity and magnetism.

This effect is certainly close to the one observed by Rosensweig [56] (see the application on the conical meniscus at the end of the fifth chapter on pages 79 to 82) who shows that the height of the meniscus formed around a wire emerging vertically from a ferrofluid pool depends on the current passing through this wire and, therefore, on the magnetic field intensity. Moreover, Elias *et al.* [65] have also noticed the impact of the magnetic field on the meniscus. In their paper, they studied the drainage of a ferrofluid soap film as well as the control and description of a ferrofluid soap foam inside a tube. They notably highlight the crucial role of the meniscus and the direction of the applied magnetic field on the drainage of the ferrofluid soap film, in particular on its velocity. Indeed, a magnetic field applied perpendicularly to the film tends to speed up the drainage whereas a field applied parallel to the film tends to slow it down. This is due to the interaction between the magnetic moments, which is less favourable inside the film than inside the meniscus when the field is perpendicular to the film, thus enhancing the drainage. A similar effect could be expected on a sessile bubble since they are also composed of a meniscus and a soap film. Yet, as the soap film is not flat, the effect might be more complex, especially for small bubbles

[1]At worst, it shifts the fluid pressure P_l by a constant amount.

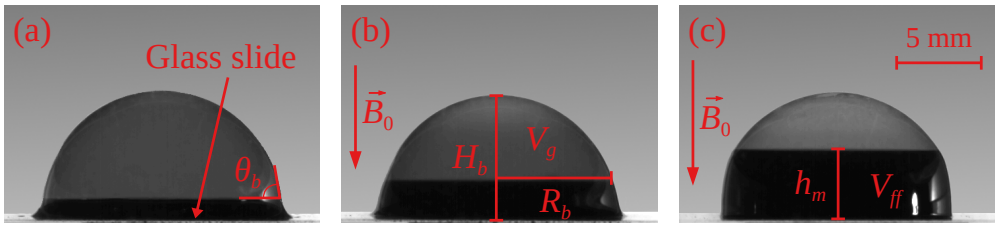

Figure 7.1: Pictures of bubbles resting on a microscopic slide under a uniform vertical magnetic field. Picture (a) shows the bubble on a slide when the intensity of the magnetic field $B_0 = 0$. Image (b) depicts the shape of a bubble under a uniform vertical magnetic field having an intensity of $B_0 = 11.07$ mT. Picture (c) illustrates a bubble further deformed by an applied field of higher intensity $B_0 = 41.22$ mT. The size of the bubble meniscus grows with the intensity of the uniform magnetic field. The bubble adopts the shape of a spherical cap siting atop of a cylinder. The height H_b, the radius R_b and the volume V_g of the bubble are measured, as well as the ferrofluid volume V_{ff} [m^3], the meniscus height h_m and the contact angle at the top of the meniscus θ_b.

with a larger curvature. Furthermore, the shape of the meniscus also depends on the applied magnetic field, which should make the drainage mechanics in a bubble even more complex.

Finally, there is another system closely related to a bubble resting on a solid surface: magnetic foams, which have also been studied by Elias *et al.* [135]. They used Hele-Shaw cells to observe the configuration adopted by a biphasic system consisting of two immiscible liquids: a ferrofluid and an organic oil. They investigated the effect of the ferrofluid surface fraction as well as those of the magnetic field intensity. They succeeded in obtaining ferrofluid droplets[2] inside the oil for lower applied magnetic fields ($\tilde{H}_0 = 13.1$ kA/m) and lower ferrofluid fractions (*i.e.* 20%). They also obtained dry and wet froth, but unlike the previous case, the ferrofluid has the higher surface fraction and oil forms the liquid shells between the ferrofluid droplets. Based on the knowledge

[2]They called them "bubbles", but as there is only one oil/ferrofluid interface, we substitute the terms to maintain consistency throughout the thesis.

developed in these papers, we propose in the following to analyse how gravity, capillarity and magnetic field prescribe the meniscus shape.

7.2 Materials and Methods

The deformations due to the application of a uniform magnetic field were studied using two coils mounted in a Helmholtz configuration. The uniformity of the magnetic field between the two coils was verified in a circular area of 50 mm radius whose centre corresponds to that of the coils. The deviation relative to the field at the centre was found to be of the order of 3%, at worst. Moreover, the vertical uniformity of the field was even better, diverging by less than 1% over 20 mm. As the size of the bubbles is smaller, the applied field can be considered as uniform over the entire bubble. A power source was used to establish the direct current inside the coils, which was first amplified to reach field intensities of up to 50 mT. The law linking the uniform magnetic field at the centre of the coils to the voltage ϕ used to establish the current was found to be linear as expected (see the graphic on the left-hand side of Fig. 7.2 (b)). The linear law adjusted gives us $B_0 = 6.7\phi - 3$ for the magnetic field intensity in mT. The images of the bubbles were recorded thanks to a camera placed in front of them. To limit their evaporation, bubbles were caged inside an hermetic chamber made of transparent Perspex sheets with some wadding soaked with water. Sketches of the experimental set-up are presented in Fig. 7.2.

A droplet of a preset volume of ferrofluid soap V_{ff} was released onto a microscope slip glass using a micro pipette with an accuracy of 0.1 µl. After dropping the droplet off, a syringe pump was used to inflate the bubble by injecting air directly inside the soapy solution. Bubbles created in this way not only have their size (through the injected air volume V_g) fixed, but also the amount of ferrofluid V_{ff} used to create it. The whole process between the bubble creation and the beginning of the experiment lasted about 10 s. Three initial gas volumes ($V_g = 1,\ 0.5$ and 0.25 ml) together with five ferrofluid volumes ($V_{ff} = 3, 7\ , 15\ , 30$ and 60 µl) were used. As for the bubbles under an electric field, due to compressibility and air leakage, V_g was not perfectly reproducible. Therefore, we also determined the precise volume a

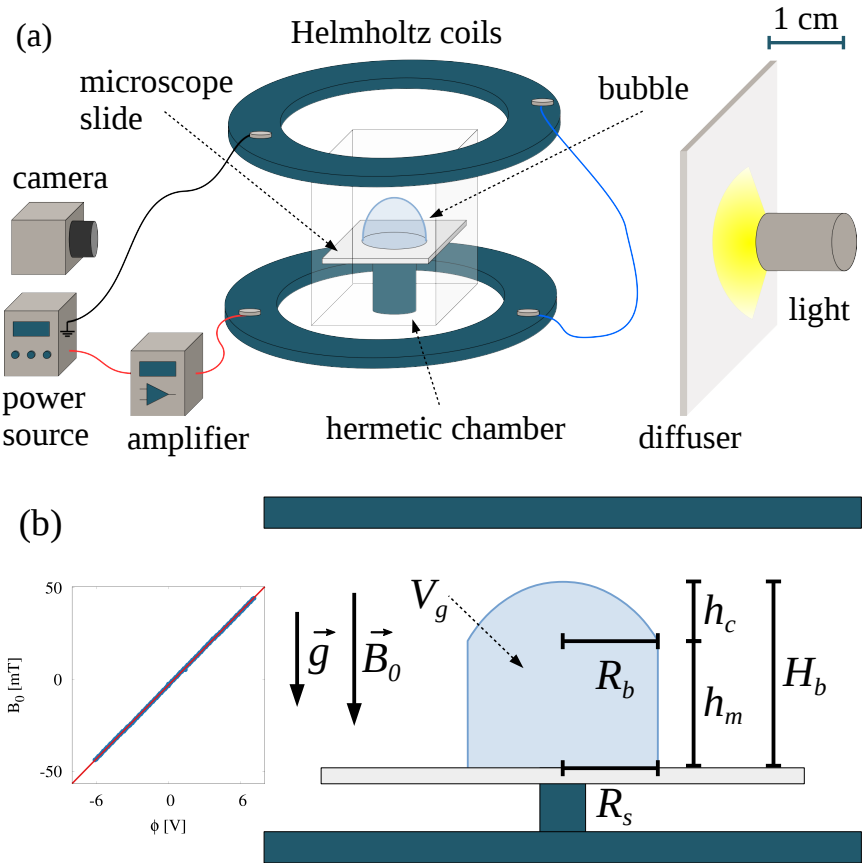

Figure 7.2: Sketches of the experimental set-up used for measurements performed on sessile bubbles under magnetic field. (a) Summary of the elements composing the experimental set-up. (b) Drawing of the geometrical measurements of the experiment: the magnetic field $\vec{B}_0$, the gravity field $\vec{g}$, the heights of both the meniscus and the spherical cap forming the bubble, its total height H_b and its internal volume V_g as well as two of its radii R_b and R_s [m] measured respectively at the top of the meniscus and at the base of the bubble. The graphic showing the linear relationship between the applied potential ϕ and the intensity of the uniform magnetic field B_0 is presented on the left of the sketch. The adjusted linear law is drawn in red. The scale of both sketches is the same and is indicated in the upper right-hand corner.

posteriori, by imaging.

The ferrofluid soap is described in Appendix B. The magnetisation curve of the ferrofluid, presented in Fig. 7.3 and obtained with a vibrating sample magnetometer, is typical of a superparamagnetic colloid. The graphic represents the magnetisation M of the ferrofluid as a function of the internal field $\tilde{H}$, the blue dots being the measured values and the red curve a phenomenological adjustment to the data. The function used to adjust the data describes not only the magnetisation under low fields (which is generally approximated by a linear function), but also the magnetisation at higher fields (a logarithmic function is usually used in this case, see Ref. [109] for example). This function is written as follows:

$$M(\tilde{H}) = \frac{\chi_l M_s \tilde{H}}{M_s + \chi_l \tilde{H}} \tag{7.3}$$

with χ_l and M_s [A/m] the two fitting parameters, χ_l being the magnetic susceptibility in the linear regime and M_s the saturation value of magnetisation. For the soap ferrofluid, the two parameters are equal to $\chi_l = 2.65 \pm 0.04$ and $M_s = 41 \pm 0.08$ kA/m.

The experiments were carried out by recording 1 min videos in which the intensity of the applied magnetic field B_0 was increased in 2.01 mT increments every 10 s. The videos are a succession of approximately 5 s of bubble shape recording followed by 5 s of black screen during which the magnetic field is modified and the bubble reaches its steady shape. As the bubble lifetime did not allow the full range of magnetic fields to be explored (from -3 mT to 43.23 mT) several bubbles were used. Each recording started at -3 mT before either picking up where the last bubble had allowed us to arrive, or changing the parameters and starting a new one. All experiments were performed at least three times and three experiments were done with negative magnetic fields (namely from -3 mT to -43.2 mT), to verify that only the field intensity mattered and not its direction.

The video recordings of the experiments were cut into segments of constant field and, as the bubble reached a steady regime, each part of the recording was summarised into a single image by averaging all those composing the portion using ImageJ [136]. The average pictures thus obtained are then analysed using an home-made Python code in order to

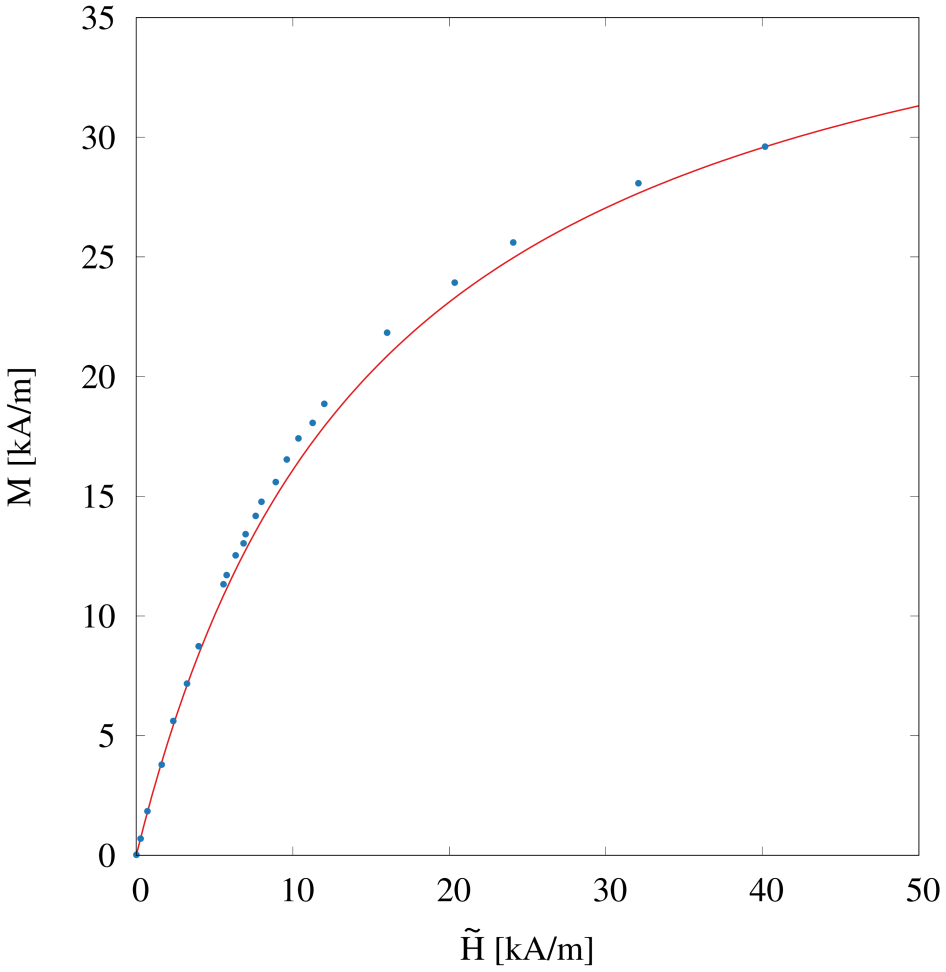

Figure 7.3: Magnetisation curve of the ferrofluid soap obtained with a vibrating sample magnetometer. It represents the magnetisation of the ferrofluid M as a function of the field $\tilde{H}$ inside it. The blue bullets are the measured values and the red line is the phenomenological adjusted function. This function takes the form described by Eq. 7.3 with χ_l and M_s being the two fitting parameters. For the ferrofluid soap, the fitting parameters are equal to $\chi_l = 2.65 \pm 0.04$ and $M_s = 41 \pm 0.08\,\mathrm{kA/m}$, respectively.

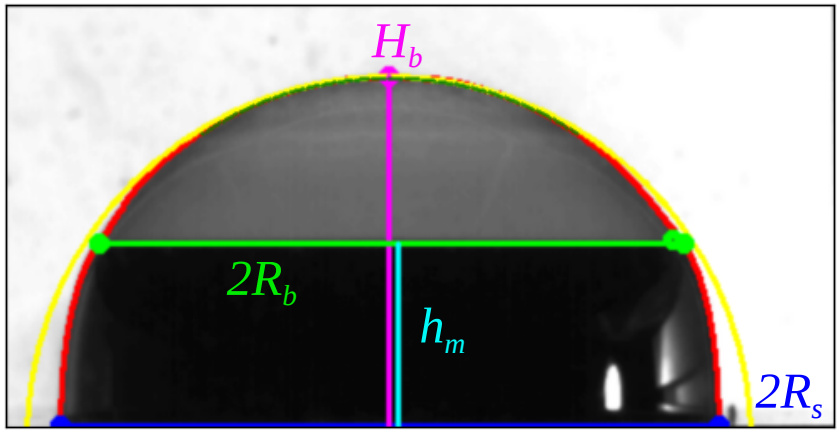

Figure 7.4: Picture used to obtain the different lengths characterising the bubble shape. The image was obtained by first averaging a segment of a video recording of a bubble ($V_g = 0.5$ ml and $V_{ff} = 15$ µl) under a uniform magnetic field $B_0 = 31.17$ mT and then processing it with an home-made Python program. The black frame around the picture represents the region of interest used to define the cropping of the image. The detected edge of the bubble is drawn in red, its height H_b in pink, its base length $2R_s$ in blue. The meniscus height h_m is shown in cyan and the length $2R_b$ at the meniscus top in green. The highest part of the edge used to determine the curvature and the position of the apex is highlighted in dark green. The circle resulting from the curvature is drawn tangentially to the bubble apex in yellow.

extract the different characteristic lengths defining the bubbles shapes. The procedure applied by the Python program is the same as that used on the floating bubble under an electric field, described in Section 6.2. In addition to the measurements performed by the routine already detailed (*i.e.* h_m, H_b, R_b, h_c, S_g [m^2], V_g), the radius at the base of the bubble R_s, was also measured (note that the measured surface and volume are the total surface and volume S_g and V_g and not those of the floating part since there is no longer an immersed part). Finally, the angle at the top of the meniscus θ_b, modified by the application of a magnetic field, is directly measured on the pictures averaged with ImageJ. The Python

routine was not used to extract θ_b because, as $\theta_b \sim 90^\circ$ on sessile bubbles, the third degree polynomial used to compute it on floating bubble fails to give a satisfactory accuracy[3] (see Ch. 5). An example of such an averaged picture and the detected lengths is presented in Fig. 7.4.

The origin of the typical errors on H_b and R_b has already been described in Section 5.1 and leads to the same result (*i.e.* 50 µm for the error on H_b and smaller for that on R_b). Moreover, in Section 6.2, the errors on S_g and V_g were determined to be of the order of a few percents and it was shown that the error on h_m has the same origin as that on H_b and therefore has the same magnitude, namely 50 µm. Finally, the error on R_s is only related to the base detection and is then smaller than that on h_m or H_b and the error on θ_b is estimated to be of the order of 1°. To summarise, this corresponds to a relative error of one percent or less for all characteristic lengths.

7.3 Whole Bubbles under Magnetic Fields

In order to rationalise the effect observed in the pictures presented in Fig 7.1, the meniscus height h_m was measured for an increasing applied field $\tilde{H}_0$. The results are presented in Fig 7.5 for a bubble of $V_g = 0.5$ ml and $V_{ff} = 15$ µl. Each point represents the average of three different measurements with the associated standard deviation. Pictures (i) and (ii) of Fig. 7.5 show the ferrofluid bubble under a field intensity $\tilde{H}_0 = 8.86$ kA/m and $\tilde{H}_0 = 32.96$ kA/m respectively. A first observation can be made: as the applied field $\tilde{H}_0$ increases and the meniscus rises higher, the shape of the sessile bubble changes from a hemispherical shape to one that closely resembles that of a spherical cap siting atop of a cylinder, with the meniscus forming the cylinder.

To make informed assumptions about the internal field $\tilde{H}$ inside the meniscus, the overall shape of the bubble must be determined. Indeed, $\tilde{H}$ directly depends on the bubble shape through the demagnetising factor D_m, and can be written as follows

$$\tilde{H} = \tilde{H}_0 - D_m M. \tag{7.4}$$

[3]On sessile bubbles, the edge rises almost vertically and therefore θ_b cannot be captured by a function.

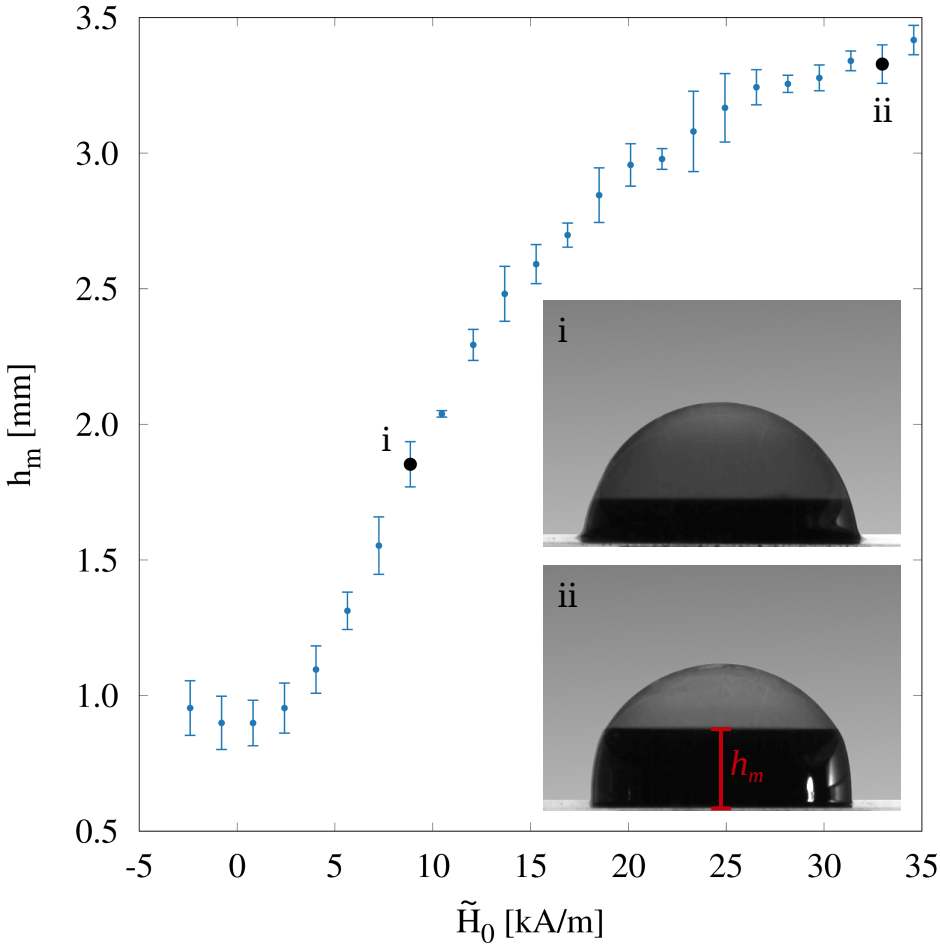

Figure 7.5: Steady height of the bubble meniscus h_m as a function of the applied field $\tilde{H}_0$. The volume of the sessile bubble and the ferrofluid volume used to create it were respectively $V_g = 0.5$ ml and $V_{ff} = 15$ µl. Each point represents the averages of three measurements made on three distinct bubbles, with the associated standard deviation. Picture (i) and (ii) illustrate the shape of the bubble under $\tilde{H}_0 = 8.86$ kA/m and $\tilde{H}_0 = 32.96$ kA/m respectively.

Due to the uniformity of the internal magnetisation, this factor can be calculated exactly for the simplest cases such as spheres, solid cylinders or infinite planes (see Ref. [79] for example) and Osborn [137] has tabulated it for a general ellipsoid.

Since most of the ferrofluid is concentrated inside the meniscus, which is very similar in shape to a cylinder, we assume that the ferrofluid forms a cylinder with a thickness e_m [m] at least ten times smaller than its outer radius. To validate the cylinder hypothesis, the radius at the base of the bubble and that at the top of the meniscus, respectively labelled R_s and R_b, were measured. The closer the values of the radii are, the more valid the hypothesis is. The results are presented in Fig. 7.6 for the different values of the ferrofluid volume V_{ff}. As it can be observed, the radii are very close to each other when the amount of ferrofluid is small and the bubbles are large. This was expected because, according to cylindrical symmetry, the amount of liquid per unit length around the bubble base is proportional to V_{ff}/R_b. Thus, the smaller the bubbles and the greater the amount of liquid, the more ferrofluid accumulates in the meniscus. As the height is prescribed, the accumulation induces a lateral extension, eventually leading to a larger difference between the two radii.

Furthermore, the difference between the radii is small compared to the value of h_m, except for low values of the applied field $\tilde{H}_0$ where they are comparable[4]. Under these conditions, the ferrofluid can be considered to rise almost perpendicular to the substrate. This approximation is fairly accurate for all sets of parameters, except perhaps in the worst case when $V_g = 0.25$ ml, $V_{ff} = 60$ µl and for small $\tilde{H}_0$. As we are interested in describing the meniscus under an increasing field and since the approximation improves with increasing field strength, we decided to assume that the meniscus has a cylindrical shape for all sets of parameters. The radius of this cylinder is assumed to be equal to the average of the two radii, namely $R_a = (R_b + R_s)/2$ [m], its height being equal to h_m and its volume to V_{ff}[5].

[4]Again, this was expected since, at zero field, the lateral extension of the meniscus and its height are both of the order of magnitude of the capillary length κ^{-1}

[5]Indeed, the amount of liquid inside the spherical cap is very small as $2\pi R_s^2 e_b \ll V_{ff}$, with e_b the film thickness.

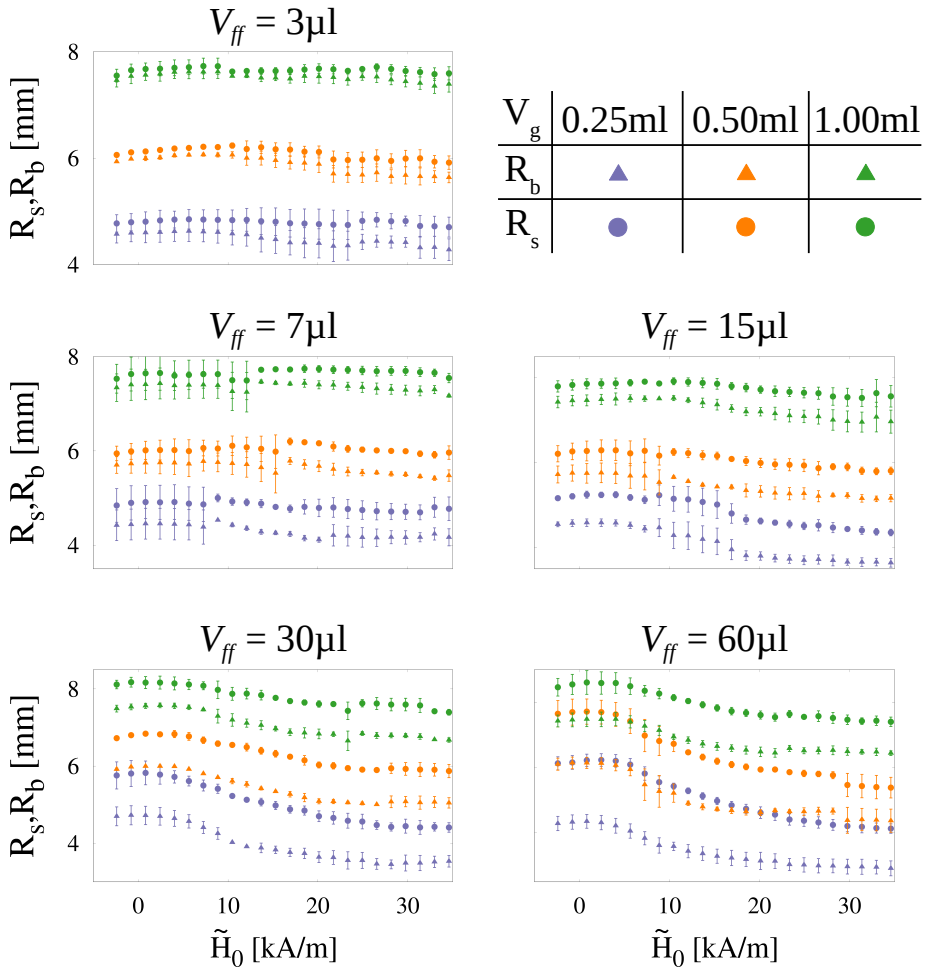

Figure 7.6: Values of R_b (solid triangles) and R_s (solid circles) for the five ferrofluid volumes considered (V_{ff} = 3, 7 , 15 , 30 and 60 µl). The three air volumes used V_g are represented by the same colour in each graphic for all applied fields $\tilde{H}_0$: V_g = 0.25 ml in lilac, V_g = 0.50 ml in orange and V_g = 1.00 ml in green. Each point represents the average of three measurements with the corresponding standard deviation.

Above the meniscus, the thin film of soap that closes the bubble is almost transparent and can therefore be assumed to contain a very small amount of ferrofluid. Therefore, both effects of $\tilde{H}_0$ and gravity are assumed to be negligible and the film should take a shape prescribed by surface tension alone, namely a spherical cap. To validate this hypothesis, the value of the measured cap height $h_{c,m}$ [m] can be compared to the calculated one $h_{c,c}$ [m]. The latter is calculated from the measured cylinder radius R_a and the angle measured at the top of the meniscus θ_b. Assuming a spherical cap, this leads to

$$h_{c,c} = R_a \frac{1 - \cos(\theta_b)}{\sin(\theta_b)}. \tag{7.5}$$

If the two values of h_c (*i.e.* $h_{c,m}$ and $h_{c,c}$) are close, the soap film adopts the shape of a spherical cap. In this case, gravity and magnetism have negligible effects on the soap film.

In Fig. 7.5 each point once again represents the average of three measurements with the corresponding standard deviation. The measured and calculated h_c are plotted for each set of parameters, namely for the five V_{ff}, the three V_g and for all applied fields $\tilde{H}_0$. The solid black line is a guide for the eyes representing $h_{m,c} = h_{c,c}$. As it can be seen, if the standard deviation is taken into account, all data evidence that the calculated and measured heights are equal. Consequently, in the following, we consider that the part of the bubble located at the top of the meniscus adopts a spherical cap shape.

A further validation of the overall bubble shape is given by comparing the measured volume $V_{g,m}$ [ml] with that obtained by assuming a spherical cap setting atop of a cylinder $V_{g,c}$ [ml]. The total volume is calculated by adding the volume of a cylinder of measured radius and height R_a and h_m respectively, with that of a spherical cap having the same radius and a measured angle θ_b. This results in the following expression, the left-hand side being the cylinder volume and the right-hand side that of the spherical cap:

$$V_{g,c} = \pi h_m R_a^2 + \frac{\pi}{3} \frac{(2 + \cos(\theta_b))(1 - \cos(\theta_b))^2}{\sin^3(\theta_b)} R_a^3. \tag{7.6}$$

The comparison between the two volumes V_g (*i.e.* $V_{g,m}$ and $V_{g,c}$) is drawn in Fig. 7.8, each point representing the average of three measure-

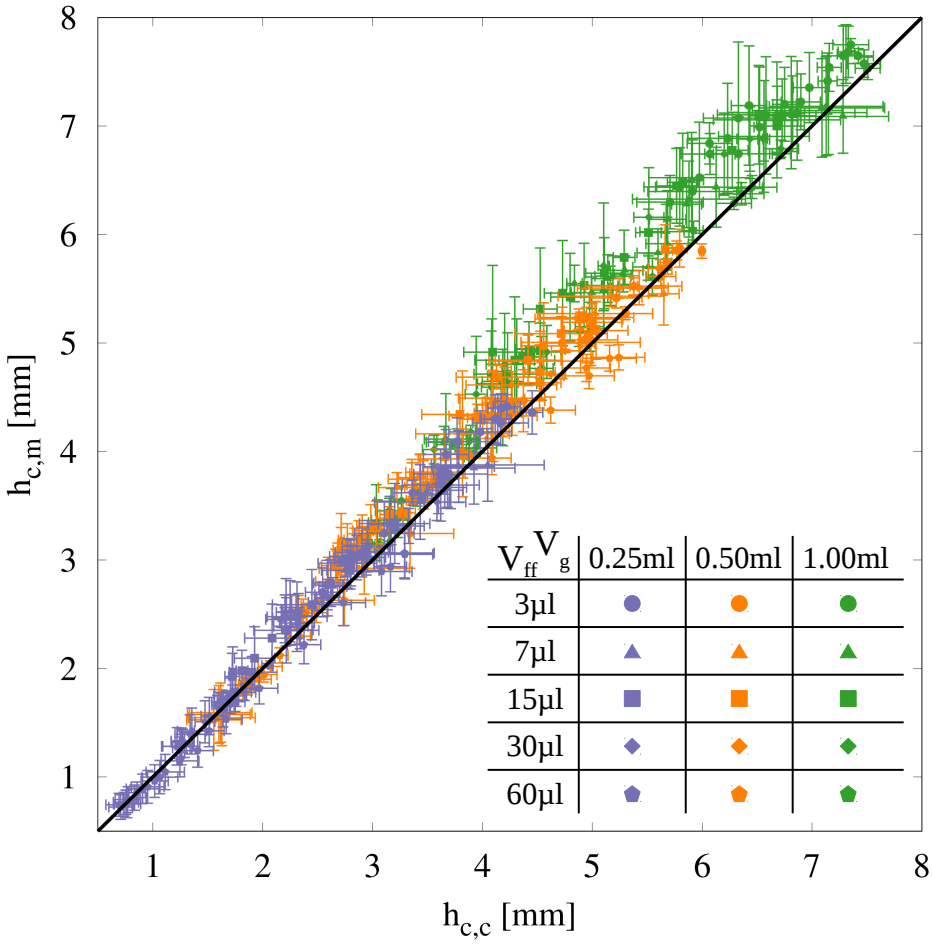

Figure 7.7: Comparison between the calculated height $h_{c,c}$ and the measured height $h_{c,m}$ for each set of parameters V_g, V_{ff} and for all applied fields $\tilde{H}_0$. The three air volumes V_g and the five ferrofluid volumes V_{ff} used are represented as follows: $V_g = 0.25$ ml in lilac, $V_g = 0.50$ ml in orange and $V_g = 1.00$ ml in green together with $V_{ff} = 3$ µl with solid circles, $V_{ff} = 7$ µl with solid triangles, $V_{ff} = 15$ µl with solid squares, $V_{ff} = 30$ µl with solid diamonds and $V_{ff} = 60$ µl with solid pentagons. The black line is a guide that represents $h_{c,c} = h_{c,m}$.

ments with the corresponding standard deviation. The same label is used to represent the different parameters. All the data cluster in three groups around the preset values of the gas volume V_g, showing that, although there is some dispersion around these values, the predefined volumes are reasonably accurate. The solid black line is a guide for the eyes representing $V_{g,c} = V_{g,m}$. Similarly to the cap height, almost all data points follow the black curve, meaning that the measured volume is equal to the calculated one. The only sets of parameters for which the $V_{g,c}$ is too large are $V_g = 0.5$ ml, $V_{ff} = 60$ µl and small applied fields $\tilde{H}_0$. However, even for these sets of parameters, the error on the calculated value remains limited. Altogether, the approximation made on the shape seems to describe very well the deformation of the bubble under a magnetic field. The meniscus is therefore considered to be subject to all the effects of the magnetic field and to form a cylinder while the rest of the bubble is only affected through the meniscus deformation and forms a spherical cap.

The shape assumed by the ferrofluid bubble having been verified, the value of the corresponding demagnetising factor can be determined. Beleggia *et al.* [138] have derived an approximate analytical expression for this demagnetising factor for cylindrical shells and in particular for thin cylindrical shells (see formula 20 in their paper). Considering that the height h_m of the cylinder is of the same order of magnitude than its radius R_a and that its thickness e_m is at least ten times smaller than R_a, the demagnetising factor takes a value of the order of 0.1. This is the worst-case scenario, corresponding to the thickest cylinders obtained with $V_g = 0.25$ ml, $V_{ff} = 60$ µl and weak applied fields $\tilde{H}_0$. Moreover, the magnetisation curve presented in Fig 7.3 shows that the magnetisation M has the same order of magnitude as the internal field $\tilde{H}$. According to these two considerations, the internal field $\tilde{H}$ decreases by a factor 1.1 compared to the applied field $\tilde{H}_0$. At first sight, we therefore consider that the applied field $\tilde{H}_0$ is equal to the internal one $\tilde{H}$. This assumption can be further justified. Firstly, as shown in Fig 7.3, as soon as the internal field $\tilde{H}$ increases, the ratio between M and $\tilde{H}$ decreases. Consequently, as the applied field $\tilde{H}_0$ increases, $\tilde{H}$ approaches $\tilde{H}_0$. Secondly, a taller cylinder has a smaller demagnetising factor. Because the meniscus height increases with $\tilde{H}_0$ (see Fig. 7.5), this further

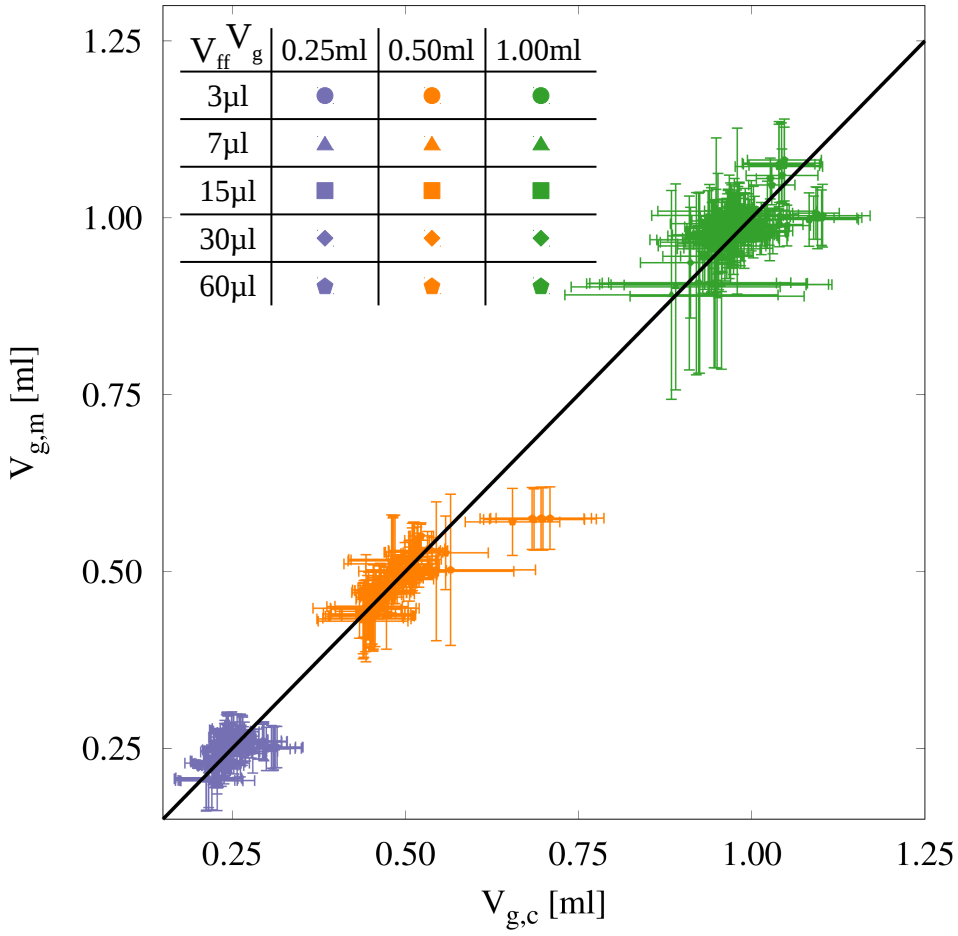

Figure 7.8: Measured volume $V_{g,m}$ plotted against calculated volume $V_{g,c}$ for each set of parameters and for all applied fields. The same label as in the previous figure (Fig. 7.7) is used to depict each set of parameters. The black line is a guide that represents $V_{g,m} = V_{g,c}$.

decreases the difference between $\tilde{H}$ and $\tilde{H}_0$ as $\tilde{H}_0$ increases. Finally, $D_m = 0.1$ is the upper limit of D_m corresponding to the worst-case scenario ($V_g = 0.25$ ml, $V_{ff} = 60$ µl). For all other combinations of parameters, D_m decreases and reaches $D_m = 0.01$ in the most favourable cases. All in all, if the assumption on $\tilde{H}$ fails, it will be for small $\tilde{H}_0$ and for small bubbles with a large amount of ferrofluid. This combination of unfavourable factors is the same as the one already highlighted with the discussion on Fig. 7.6. We therefore decided to stick to these assumptions and keep in mind that they could fail in most unfavourable cases.

7.4 Meniscus under Magnetic Fields

In order to rationalise the meniscus growth under magnetic field, let us first characterise its size without magnetic field. Although this problem has already been solved[6], rethinking it in the light of dimensional analysis is a good starting point for understanding the whole phenomenon we are dealing with. Assuming that the bubble is large enough so that its horizontal curvature has no effect on the meniscus, its shape can be entirely characterised by its height alone. Moreover, the two pressures involved in its creation are the hydrostatic $P_h \sim \rho g h_m$ and the capillary $P_\gamma \sim \gamma h_m^{-1}$ pressures. Consequently, h_m can be expressed as a function of the three dimensional governing parameters, which are ρ, g and γ. All having an independent dimension, we formulate h_m as follows

$$[h_m] = [\rho]^{-1/2}[g]^{-1/2}[\gamma]^{1/2}. \tag{7.7}$$

Therefore, according to dimensional analysis and the Buckingham Π-theorem [132], the following relation can be written:

$$h_m = C_0 \kappa^{-1} \tag{7.8}$$

with C_0 a dimensionless constant and $\kappa^{-1} = \sqrt{\gamma/\rho g}$ the capillary length. Thanks to the reflection carried out in Ref. [30, 8], we can find that the value of the constant must be close to $C_0 = \sqrt{2(1 - cos(\theta_b)}$.

[6] See Teixeira *et al.* [8] for floating bubbles or de Genne *et al.* [30] for those that are sessile, taking into account the precautions explained in Ch. 5.

When a field $\tilde{H}_0$ is applied to the ferrofluid, magnetic pressures come into play. According to Eq. 7.2, these pressures arise from two effects: the first is the magnetic pressure inside the fluid $P_{m,i} = \mu_0 \int_0^{\tilde{H}} M \mathrm{d}\tilde{H}^*$ and the second is the magnetic pressure at the interface due to the normal continuity of the magnetic field $P_{m,n} = \mu_0 M_n^2/2$. As the cylinder rises in the direction prescribed by the magnetic field, with all the magnetic dipoles of the ferrofluid aligned in the same direction, the component of the magnetisation normal to the interface is zero, as is the second contribution to the magnetic pressure. Moreover, the magnetisation M is related to the internal field $\tilde{H}$ by Eq. 7.3 and, therefore, the set of magnetic effects can be characterised by two dimensional parameters M and μ_0 and a dimensionless one χ, the magnetic susceptibility, which, in general, is a function of $\tilde{H}$. We have chosen to keep M instead of $\tilde{H}$ or $\tilde{H}_0$ because it directly measures the magnetic effects inside the ferrofluid. Assuming that the horizontal curvature still has no effect on the meniscus[7], the height h_m can be defined as a function of five dimensional parameters, ρ, g, γ, μ_0 and M and a dimensionless one χ. Four of the dimensional parameters have independent dimensions and the dimension of the fifth can therefore be expressed as a product of the others. If the dimension of μ_0 is chosen as the dependent one, it can be formulated as follows

$$[\mu_0] = [\rho]^{1/2}[g]^{1/2}[\gamma]^{1/2}[M]^{-2}. \tag{7.9}$$

Moreover, the dimension of h_m has also been expressed as the product of the same four dimensional parameters (see Eq. 7.7 with $[M]$ exponent to the zero power). Then, according to dimensional analysis and the Buckingham Π-theorem [132], the following relation applies:

$$h_m = \kappa^{-1} f_m \left(\frac{\mu_0 M^2}{\sqrt{\rho g \gamma}}, \chi \right) \tag{7.10}$$

with $f_m(\mu_0 M^2/\sqrt{\rho g \gamma}, \chi)$ a function of the two dimensionless numbers $\mu_0 M^2/\sqrt{\rho g \gamma}$ and χ.

[7]This seems consistent since this contribution was already negligible in the absence of a magnetic field. Therefore, adding a term that becomes increasingly dominant as the magnetic field increases does not make the effect of the horizontal curvature any less negligible.

This dimensionless number can be manipulated to highlight the two characteristic lengths of the problem. If we define the magnetic length l_m [m]:

$$l_m = \frac{\mu_0 M^2}{\rho g}, \tag{7.11}$$

Eq. 7.10 can be rewritten as follows

$$h_m = \kappa^{-1} f_m \left(\frac{l_m}{\kappa^{-1}}, \chi \right). \tag{7.12}$$

The two characteristic lengths reflect a competition between a driving effect, which pulls the liquid upward, and a restraining effect, which has the opposite outcome. For both characteristic lengths, the restrain is gravity, which pulls the ferrofluid down, but the motor is different. In κ^{-1}, it is capillarity that is at work, whereas in l_m it is the magnetic in-fluid pressure $P_{m,i}$. As f_m is a function of the ratio between these two lengths, two different regimes are expected: one dominated by capillarity and the other by magnetic pressure. The transition between these two regimes occurs when the two lengths are equal, namely at a critical magnetic field $M_c \approx 4.2$ kA/m. In the capillary regime, the meniscus shape is close to the usual one, with its height h_m defined by Eq. 7.8. In the magnetic regime, the meniscus shape is gradually transformed into a cylinder. This metamorphosis erases the initial curvature of the meniscus, inducing the disappearance of the capillary pressure linked to this curvature. As the horizontal curvature is not taken into account in this first-order model, capillarity and magnetism can be considered to act solely in their respective regimes.

To highlight the effect of the magnetic field on the meniscus height, h_m has been plotted as a function of the squared magnetisation M^2 in Fig. 7.9 for each volume of air ($V_g = 1,\ 0.5$ and 0.25 ml) and volume of ferrofluid ($V_{ff} = 3,\ 7,\ 15,\ 30$ and 60 µl). The labels used in the figure are the same as previously and each point represents the average of three different measurements with the corresponding standard deviation. The vertical red line indicates the transition between the capillary-dominant and magnetic-dominant regimes. As it can be seen, only the points corresponding to a very weak magnetic field belong to the first regime (the first two points of each data set, corresponding to a negative value

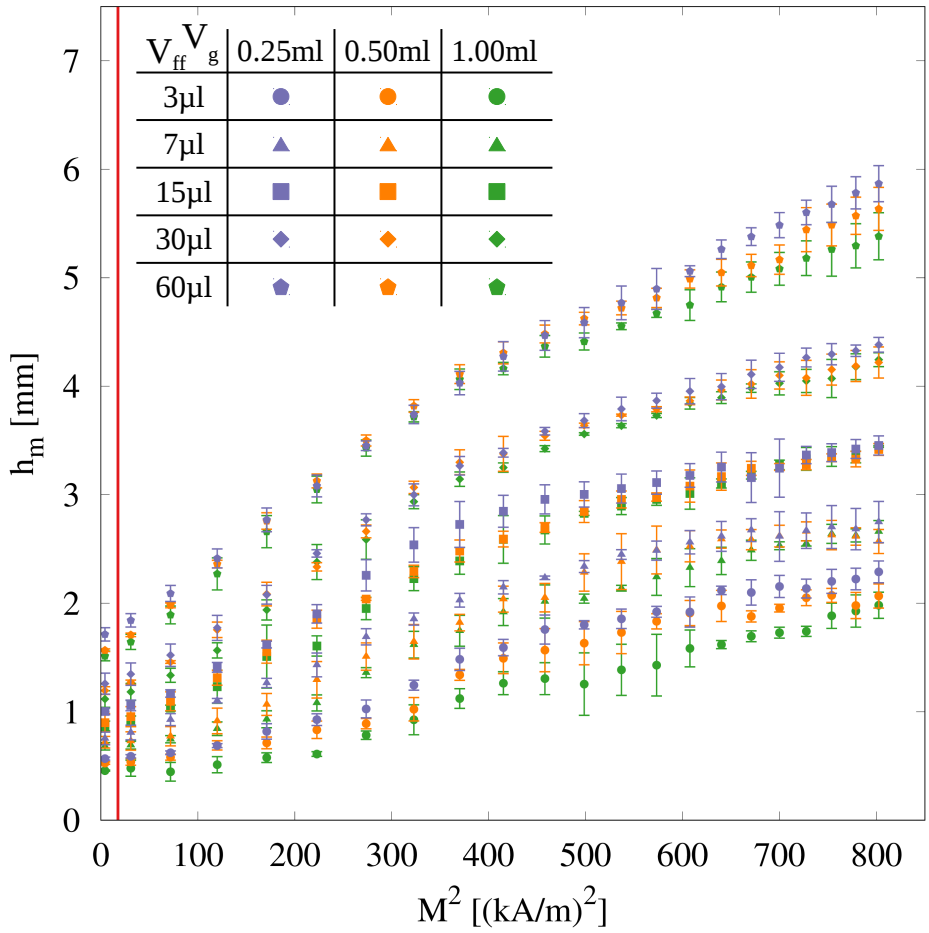

Figure 7.9: Meniscus height h_m drawn as a function of the squared magnetisation M^2 for each volume of air ($V_g = 1,\ 0.5$ and 0.25 ml) and volume of ferrofluid ($V_{ff} = 3,\ 7\ 15\ 30$ and 60 µl). The label used is the same as in the two previous figures and similarly, each point represents the average of three measurements with the corresponding standard deviation. The vertical red line marks the separation between the capillary-dominant regime and the magnetic-dominant one, namely when $M_c^2 = 17.64$ kA/m.

of M, have been omitted in this graphic to keep it clear). Therefore, almost the entire range of applied fields corresponds to a meniscus shape prescribed by the magnetic field. Another observation can be made on this graphic: all data seem to be roughly sorted into five categories, each corresponding to a different V_{ff}. Furthermore, the value of the meniscus height in the capillary-dominant regime $h_{m,0}$ [m] varies with V_{ff} and V_g. However, this value must be fixed by κ^{-1}, which is the same for all parameters. To resolve this apparent contradiction, we need to first propose a form for the f_m function describing the effect of the magnetic pressure.

7.5 Linear regime

The main restriction on the function f_m describing the deformation of the meniscus under magnetic field is that it must tend to C_0 when the magnetic field tends to zero (see Eq. 7.8), *i.e.* when h_m is prescribed by κ^{-1}. Conversely, as the field increases, the shape must be in the magnetic regime. A function that satisfies the definition given by Eq. 7.12 can be proposed for a weak applied field, *i.e.* when M increases linearly with $\tilde{H}$. If we consider Eq. 7.3, when the field inside the liquid is weak compared to the saturation magnetisation M_s, $M(\tilde{H}) \approx \chi_l \tilde{H}$. Under these conditions, the internal magnetic pressure $P_{m,i}$ takes a much simpler form: $P_{m,i} \sim \mu_0 M^2/2\chi_l$. Therefore, $l_m/2\chi_l$ is nothing but the characteristic meniscus length obtained by equating $P_{m,i}$ and $P_h \sim \rho g h_m$. Since l_m directly represents the pressures' ratio, this suggests that f_m could be linear in l_m under weak fields. According to this, h_m could be described by the following equation:

$$h_m = \kappa^{-1} \left(C_1 + \frac{C_2}{2\chi_l} \frac{l_m}{\kappa^{-1}} \right) \tag{7.13}$$

with C_1 and C_2 two constants. In addition to corresponding to the definition imposed by Eq. 7.12, this equation is the expression of two distinct regimes: a capillary one represented by $C_1\kappa^{-1}$ and a magnetic one characterised by $C_2 l_m/2\chi_l$. Therefore, under near zero fields, the constant C_1 must be equal to C_0 to satisfy Eq. 7.8. However, $C_1\kappa^{-1}$ is also the value of the meniscus height in the capillary-dominant regime

$h_{m,0}$. When Eq. 7.13 is adjusted to each set of parameters independently, C_1 (and C_2) varies drastically with V_{ff} and, to a lesser extent, with V_g (as expected from the graphic displayed in Fig. 7.9). This apparent contradiction can be resolved by remembering that Eq. 7.8 is only completely valid for a meniscus rising from a liquid pool along a solid wall. For a bubble with a limited amount of liquid, the meniscus shape (and thus its height) is not solely determined by κ^{-1}, but also by the amount of liquid.

To rationalise this dependency, we assume that the meniscus has a height $h_{m,0}$ of the same order of magnitude that its lateral extension and that its shape is the same inside and outside the bubble. These assumptions make it symmetrical with respect to the plane perpendicular to the substrate and passing through its middle. Under these assumptions, and taking into account the cylindrical symmetry, the following formula can be written

$$h_{m,0}^2 = C_s \frac{V_{ff}}{R_0} \tag{7.14}$$

with C_s a shape constant and R_0 [m] the radius of the bubble in the capillary-dominant regime. This radius is calculated for $M = 2.1$ kA/m, which is, among our data, the magnetisation that is closest to M_c while remaining below its value. Besides this, R_0 is defined in the same way as for the cylinder, by taking the average of the base radius R_s and the radius at the top of the meniscus R_b at $M = 2.1$ kA/m.

The graphic of $h_{m,0}^2$ as a function of V_{ff}/R_0 is presented in Fig. 7.10. The data points are obtained by adjusting a linear function to the data corresponding to each set of parameters and are shown with the corresponding labels. As the phenomenon leading to the meniscus rise is different in each regime and acts within it, the following linear function was used to directly obtain the meniscus height within the capillary-dominant regime:

$$h_m = h_{m,0} + \frac{C_2}{2\chi_l} \frac{\mu_0}{\rho g} (M^2 - M_c^2), \tag{7.15}$$

with $h_{m,0}$ and C_2 the two fitting parameters. The vertical standard deviation is calculated by propagating the one given by the adjustment procedure. Furthermore, to determine the horizontal standard deviation,

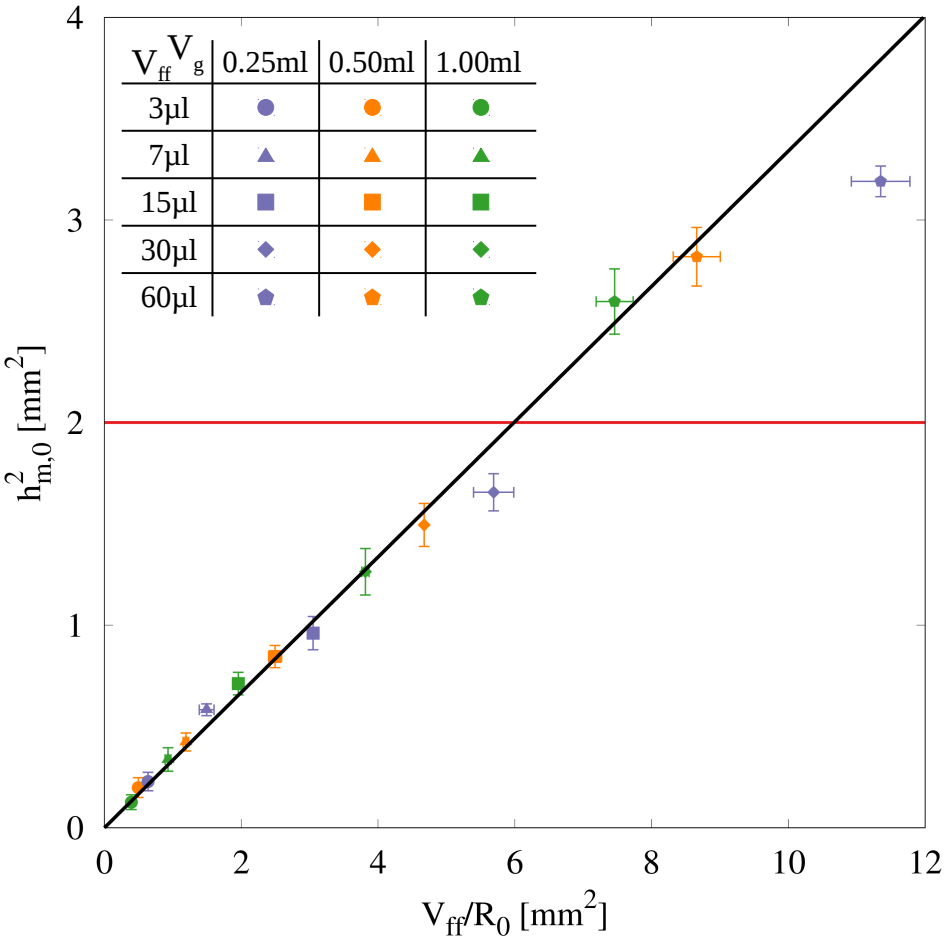

Figure 7.10: Initial meniscus height squared $h_{m,0}^2$ which is the square of the first fitting parameter obtained by adjusting a function defined by Eq. 7.15 on each set of parameters. This height is plotted as a function of V_{ff}/R_0 and each point is displayed with the label corresponding to its data set. The vertical standard deviation is obtained from that given by the fitting procedure and the horizontal one is based on the error on R_0. The black line is the law obtained by adjusting Eq. 7.14 to the $h_{m,0}^2$ smaller than the square of the capillary length, represented by the red line, and the fitting procedure gives $C_s = 0.33$.

we have considered that the error on the pipetted volume of ferrofluid is small enough to be neglected and the error is, therefore, based on that on R_0. Two regimes seem to emerge from Fig. 7.10: one below $(\kappa^{-1})^2$ and one above. The red line represents this transition.

In the first regime, the volume of liquid per unit length around the bubble base, proportional to V_{ff}/R_0, is too small to allow $h_{m,0}$ to reach κ^{-1}. In this regime V_{ff}/R_0 prescribes $h_{m,0}$ according to the law given by Eq. 7.14. We obtained the value of the shape constant $C_s = 0.33$ by adjusting this law to all $h_{m,0}^2$ below the red line[8]. In the second regime, the amount of liquid per unit length is sufficiently large and $h_{m,0}$ becomes comparable to κ^{-1}. In this case, the competition between capillary and hydrostatic pressures begins to limit the meniscus height. However, the maximum height, defined by Eq. 7.8, is still not reached and $h_{m,0}$ depends on V_{ff} and V_g. In this regime, we observe that the lateral extension of the meniscus starts to become larger than its height, especially for small V_g, thus invalidating the assumption used to justify the small liquid quantities regime. It should be noted that the values taken by $h_{m,0}$ in the second regime could also be interpreted as the expression of the saturation regime, in which the maximum meniscus height, depending on the bubble size through the angle θ_b, is reached. However, without additional data, no definite conclusions can be drawn about this particular set. Nevertheless, all experiments can be sorted into two groups: most of them belong to the first regime in which $h_{m,0}$ is defined by Eq. 7.14, while the others approach or are equal to the saturation height and can be classified into the transition or saturation regime.

According to Eq. 7.15, the slope of the adjusted linear function is equal to $C_2\mu_0/2\rho g\chi_l$. This slope has been plotted as a function of V_{ff} in Fig. 7.11 labelled in the same way as in the previous figure. Again, the vertical standard deviation comes from the adjusting procedure. As it can be seen, the slopes are a function of V_{ff}, but appear to be almost independent of V_g if the error bars are considered. The values of C_2 can be evaluated knowing that $\mu_0/2\rho g\chi_l \approx 1.6\ 10^{-2}\ \mathrm{mm}^3/\mathrm{A}^2$. This gives us a value of $C_2 = 0.146$ for $V_{ff} = 3\ \mu\mathrm{l}$ to $C_2 = 0.409$ for $V_{ff} = 60\ \mu\mathrm{l}$. Taking

[8]This value seems consistent as it is close to that obtained by assuming a constant curvature of the meniscus, *i.e.* 0.37.

into account all the hypotheses made about the bubble shape as well as about the ferrofluid distribution, and, considering that the effect of the demagnetising factor has been neglected, the values obtained seem reasonable. Furthermore, it should be noted that Fig. 7.10 and 7.11 suggest that $h_{m,0}$ and C_2 could reach saturation values for sufficiently large V_{ff}. These saturation values could be obtained by using floating bubbles as we did in Ch. 6, but this work is beyond the experimental study we want to present here.

Since the slopes of the linear function do not depend on the internal gas volumes of the bubbles V_g, the average values of the slopes for each given ferrofluid volume V_{ff} were obtained by adjusting a unique linear function, defined by Eq. 7.15, to all points corresponding to a given V_{ff}. To get rid of the influence of the initial meniscus height $h_{m,0}$, which depends on V_g, the variation of the meniscus height $\Delta h_m = h_m - h_{m,0}$ [m] was plotted as a function of M^2. According to Eq. 7.15, Δh_m is described by the following law:

$$\Delta h_m = \frac{C_2}{2\chi_l}\frac{\mu_0}{\rho g}(M^2 - M_c^2), \tag{7.16}$$

with C_2 the only fitting parameter. The results of Δh_m are presented as a function of M^2 in Fig. 7.12. The representations used in this figure are the same as those in Fig. 7.9 except that the standard deviations are not shown for clarity. The law in the linear weak fields regime defined by Eq. 7.16 is adjusted for each V_{ff} and is shown in black on each given data set. They are identified at the top right of the graphic. This graphic confirms what the one in Fig. 7.11 already shows, namely that C_2 is independent of V_g, but varies with V_{ff}. Moreover, the linear law is meaningful over almost half of the data range (namely for $M < 21$ kA/m). After the linear regime, the deformations saturate as expected from the magnetisation curve.

We decided not to do this because, as the effect of the demagnetising field was neglected, the volume of the ferrofluid is a geometric limiting factor and not a body or surface force.

It should be noted that, given the ferrofluid volume dependency, we could have added a sixth dimensional parameter V_{ff}, with the corresponding dimensionless parameter $V_{ff}/(\kappa^{-1})^3$ in the dimensional analy-

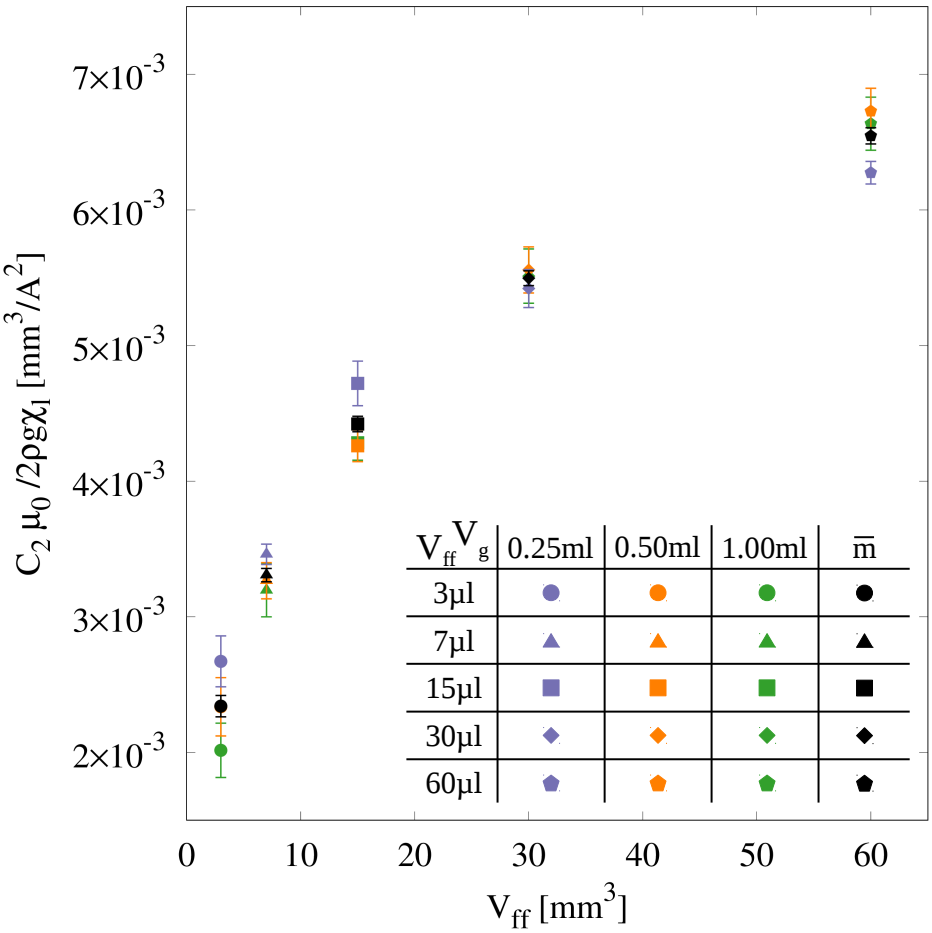

Figure 7.11: Slopes of the adjusted function $C_2\mu_0/2\rho g\chi_l$ defined by Eq. 7.13 as a function of V_{ff}. Each point represents the value obtained for a given data set and is displayed with the same label. Standard deviations are given by the adjusting procedure. The black bullets represent the mean values for each V_{ff} obtained by adjusting a linear law defined by Eq. 7.16 on all Δh_m corresponding to a given V_{ff}. Again, the standard deviations are given by the adjusting procedure.

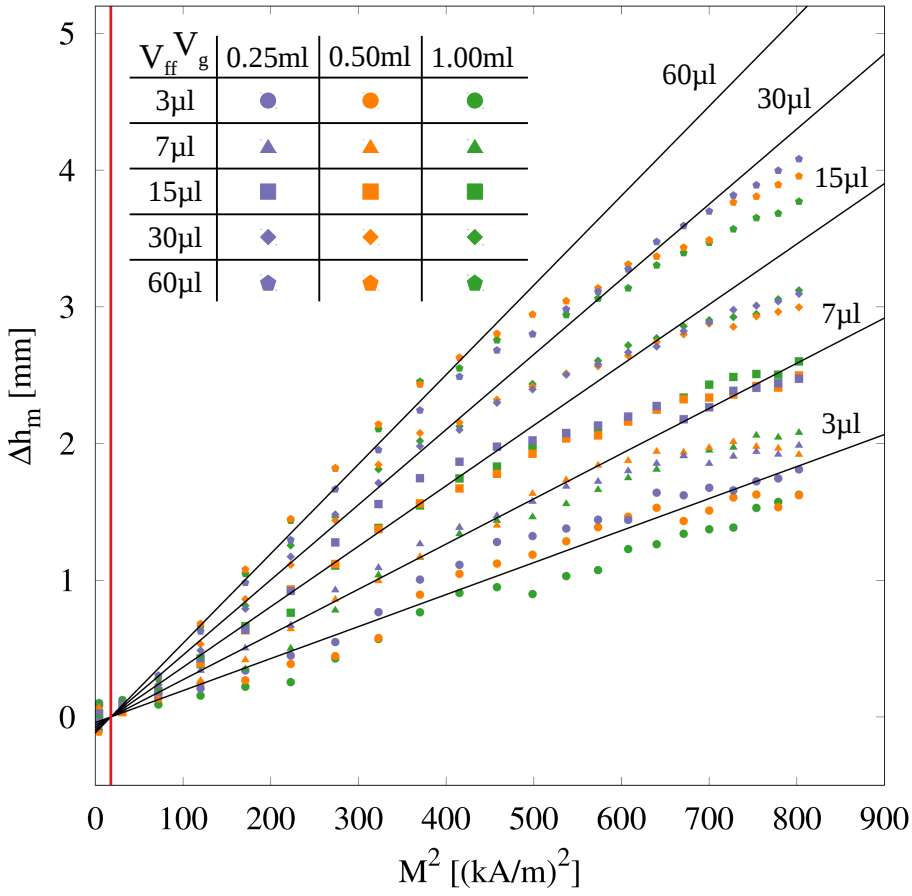

Figure 7.12: Variation of the meniscus height Δh_m as a function of M^2 for each V_g and V_{ff}. The label used is the same as in the previous graphics, each point represents the average of three measurements and the red line marks the transition between the capillary-dominant and the magnetic-dominant regimes. However, the standard deviations have been omitted to maintain a readable representation. Their order of magnitude is the same as in Fig. 7.9 (more precisely, the error bars are slightly larger due to the errors on $h_{m,0}$). Finally, the black lines represent the linear law adjusted at low field values and for a given V_{ff} (see Eq. 7.16), with their slopes being represented in black in Fig. 7.11.

sis. We decided not to do this because, the effect of the demagnetising field having been neglected, the ferrofluid volume is a geometric limiting factor and not a body or surface force. In this perspective, dimensional analysis is used to highlight the effects of the different forces involved and the law that links them, while V_{ff} modifies the coefficient of this law. Its linear form, describing the height of the meniscus under weak fields in the magnetic regime (*i.e.* for $M_c < M < 21$ kA/m), could be summarised by the following equation:

$$h_m = h_{m,0} + C_2 \frac{\Delta l_m}{2\chi_l}, \tag{7.17}$$

with $\Delta l_m = l_m(M) - l_m(M_c)$ [m], $h_{m,0}$ a function of V_{ff}/R_0 and C_2 a function of V_{ff}. Since χ_l is supposed to contain all the information about the specificities of ferrofluid, $h_{m,0}$ and C_2 can be presumed universal and therefore do not depend on the ferrofluid used. However, without further experiments with a different soap, this assertion cannot be verified. Yet, the dimensional analysis does not depend on the ferrofluid peculiarities and assuming that its magnetisation curve is similar to that presented in Fig. 7.3, Eq. 7.12 describes the size of the meniscus under an applied magnetic field, whatever the ferrofluid used. Furthermore, in the linear regime, the particular form of f_m is determined and the meniscus height is well approximated by Eq. 7.17. It should be noted that the value at which the data cease to be correctly grasped by the linear approximation (*i.e.* the weak fields limit) increases as V_{ff} decreases.

7.6 Conclusion

The deformations of bubbles made of ferrofluid soap resting on a dry, solid substrate were measured when subjected to a vertical uniform magnetic field generated by two coils mounted in Helmholtz configuration. Particular attention was paid to the meniscus as it concentrates most of the deformation. Indeed, as the magnetic field intensity increases, so does the height of the meniscus (see Fig. 7.5). As a result, the initially hemispherical bubble takes on a shape increasingly resembling a spherical cap (see Fig. 7.7) located at the top of the cylinder formed by the meniscus (see Fig. 7.6). Unlike drops under magnetic field, we

did not observe a critical magnetic field at which the ferrofluid volume separates into several daughter droplets. This lack of separation is due to the liquid film and the related surface tension that holds the cylinder together. However, when the bubble blows up naturally, the film disappears, allowing the ferrofluid that made up the meniscus to form small droplets that repel each other.

Based on the bubble shape, the internal field inside the meniscus can be approximated and the law linking this internal field to the meniscus height has been defined by Eq. 7.12 (see Fig. 7.9). Thus written, the law highlights the presence of the two characteristic lengths of the phenomenon: the capillary length κ^{-1} and the magnetic length l_m. Both of these lengths represent the competition between gravity, which pulls the liquid downwards, and a driving effect which pulls the liquid upwards: the capillary for κ^{-1} and the magnetic pressure for l_m. Since the two lengths appear as a ratio in Eq. 7.12, the growth of the meniscus is driven by two distinct regimes. In the first regime, the capillary pressure dominates the magnetic one and the shape of the meniscus is prescribed by the competition between gravity and capillarity. This regime corresponds to the well-known meniscus shape, namely a curved meniscus with its centre of curvature pointing outwards from the liquid, inducing a capillary pressure that pulls the liquid upwards. In the second regime, capillarity is negligible and the meniscus height is entirely defined by the competition between magnetism and gravity. In this new regime, the shape assumed by the meniscus is a cylinder due to the alignment of the magnetic dipoles, present inside the ferrofluid, with the internal field. In particular, the meniscus height under weak fields (*i.e.* for $M < 21\,\mathrm{kA/m}$) evolves linearly with the square of the magnetisation and is represented by Eq. 7.17 (see Fig. 7.12). The independent term in this equation represents the capillary regime and the dependent one depicts the magnetic regime. Both the independent term and the angular coefficient are functions of the liquid properties (γ, ρ for both and χ_l for the angular coefficient) as well as the amount of liquid (see Fig. 7.10 and Fig. 7.11, respectively).

The experiments presented here as well as their description confirm that, due to the intrinsic volumetric nature of the magnetic force, bubbles and droplets behave completely differently when subjected to a

uniform vertical magnetic field. Indeed, apart from the clear distinction between the shape of bubbles and droplets presented in Fig. 1.2, neither the localisation of the magnetic effect nor its expression are similar. In particular, unlike the droplet where capillarity and magnetism counteract each other, in the bubble both capillarity and magnetism favour meniscus growth. The competitions that take place inside a bubble and a droplet under uniform vertical magnetic fields are completely different and it is therefore not surprising to obtain such a difference in shape. Moreover, the volumetric nature of the magnetic force can be further highlighted by comparing the deformation induced by an electric or magnetic fields on bubbles (second column in Fig. 1.2). Indeed, although they both impact the liquid phase of the bubbles, they clearly do not deform the bubble in the same way. Due to its superficial nature, the electric force mainly affects the liquid distribution with the largest surface to volume ratio, namely the liquid shell, deforming it into a hemispherical shell. Conversely, the volumetric nature of the magnetic force induces that its effects to occur inside the liquid distribution with the smallest surface to volume ratio, *i.e.* the meniscus. These two comparisons (one with droplets under magnetic field and the other with bubbles under electric field) clearly reveal the volumetric nature of the magnetic force based on where and how it reshapes the bubble.

8

Closing Remarks and New Horizons

8.1 Closing Remarks

Now that our journey is coming to an end, it is time to look back at the distance we have travelled and see what conclusions we can draw. This journey, like the bubbles, has two phases. In the former (Ch. 2 and 3), we took the time to define the toolkit we needed to study our subject, namely bubbles. In Ch. 2, the equation of motion and the boundary conditions were presented and we extracted the pressures describing the different effects of surface and body forces. This description was also an opportunity to illustrate with the wave turbulence theory that some forces act at the fluid surface while others operate directly inside the fluid volume. In our case, surface tension and the attraction of free charges by the applied electric field induce surface forces whereas gravity and the alignment of the magnetic dipoles in the magnetic field produce volume forces (the alignment in the magnetic field also causes a surface force in addition to the volume one). If Ch. 2 served to define the tools we needed to construct our thesis and to put them into practice, Ch. 3 for its part, lays the foundations on which we built it. In this chapter, we have analysed the effect of the different body forces on an object whose shape is qualitatively similar to that of a bubble: a droplet.

Yet, although bubbles and droplets are similar in shape, their liquid distribution is completely different. In droplets, the liquid occupies the whole volume, whereas in bubbles it is confined within a thin shell with a possible meniscus if the bubbles rest on a solid or liquid substrate. The observations made in this third chapter have allowed us to grasp how the different forces influence the shape of a droplet. More importantly, with our knowledge about similarities and differences between bubbles and droplets, it serves as a map to guide us in our journey to determine the deformation induced by external fields on bubbles.

Being properly equipped, we were able to start our expedition, in the second phase of our thesis (Ch. 4 to 7). In Ch. 4, we initiate the voyage by presenting why, in our opinion, bubbles are a wonderful object of study and why the questions asked about them are relevant. The answer lies in two points: the multiphasic and multi-scale nature of bubbles. This unique combination allows to specifically target a part of the bubble with a given force. Indeed, as the gaseous and liquid phases possess different properties, they are not impacted in the same way by the forces. In our case, the gas being air, it is only affected by gravity. Conversely, the liquid phase can be made up of conducting liquid or ferrofluid, allowing its manipulation with electric or magnetic forces in addition to gravity. Moreover, due to its unique liquid distribution, the electric and magnetic effects manifest themselves quite differently in the bubble. Indeed, due to its surface nature, the force deriving from an electric field impacts the entire bubble surface, unlike the volume force induced by a magnetic field, which mainly reshapes the meniscus since it contains the majority of the liquid volume. These reflections, based on the nature of the forces highlighted in Ch. 2 and 3 and the peculiarities of the bubbles, were the first steps in the journey. They provide the basis for understanding how to manipulate bubbles with fields and give a first glimpse into why bubbles are a perfect tool for probing the nature of the body forces that act on it.

After these promising first steps, we continued our journey to deepen our guide on bubble manipulation by answering the two main questions of our thesis: how and where do the body forces manifest their effects on bubbles? Furthermore, this work has also been an opportunity to further illustrate the very distinct reactions of bubbles under different

fields. Indeed, we use the following three chapters to rationalise and obtain the different balances that define the bubble steady shape under different fields: gravity in Ch. 5, electric fields in Ch. 6 and magnetic fields in Ch. 7. In the same spirit as presented in Ch. 3, these equilibria are derived from a set of equations consisting of a generalised Bernoulli equation and boundary conditions. First, based on the different pressure terms that appear in these equations, we have build dimensionless numbers that allow us to express the competitions between the different forces involved. Second, we have provided a first order analysis describing the bubble deformations under electric or magnetic fields through a linear function of these dimensionless numbers. Third, the deviation of the deformations from the predictions of the linear laws allowed us to properly define the limits of weak fields in the electric and magnetic cases.

In Ch. 5, we saw that gravity impact both the liquid and the gaseous phases of the bubbles. The general shape of the floating bubbles derives from the competition between buoyancy due to the gaseous phase and surface tension that is represented by the Bond number $\mathrm{Bo}_b = g\rho R_c^2/\gamma$ (see the left-hand side of the lower part of Fig. 8.1). The liquid phase for its part is more locally impacted. Indeed, most of the gravity effect takes place inside the meniscus, whose size is prescribed by the capillary length $\kappa^{-1} = \sqrt{\gamma/\rho g}$, and only slightly modifies the overall shape of the largest bubbles.

In Ch. 6, the shape of sessile and floating bubbles deformed by an applied uniform electric field has been rationalised. Conversely to gravity, electric force acts only on the liquid phase of the bubbles, deforming their overall shape through liquid manipulation. As the electric force is a surface force, it directly impacts the liquid shell, reshaping it proportionally to the Bond electrical number $\mathrm{Bo}_e = \varepsilon_0 E_0^2 R_c/2n\gamma$. This number describes the competition between the two surface forces: the electric force that pulls the liquid towards the charged plate and the capillary one that tends to keep the bubble spherical. Moreover, provided that the effect of gravity has been taken into account for the initial shape of the floating bubbles, we show that both floating and sessile bubbles are similarly described by Bo_e. In the limit of weak fields, we have shown that the function predicting this deformation is linear in Bo_e (see

Eq. 6.15 and the lower central part of Fig. 8.1). Its independent term is a function of Bo_b while its slope is a constant. Thanks to this law, we were finally able to extract the limit of weak fields, namely that the deformation is linear for $\mathrm{Bo}_e < 0.05$. We also observed that the meniscus is almost not impacted by the electric force even if it modifies the overall charge distribution on the bubble.

In Ch. 7, we observed the deformation of sessile ferrofluid bubbles under a magnetic field. Like electric fields, magnetic fields only reshape the overall shape of the bubble through liquid manipulation, but unlike electric fields, they affect the meniscus. We have shown that there are two regimes defining the shape of the meniscus: a capillary and a magnetic regime. In the capillary regime, the meniscus have a size defined by the κ^{-1} as shown in Ch. 5. Conversely, in the magnetic regime, the capillary effects are negligible and the meniscus size is due to a competition between gravity and the magnetic force that tends to align the ferrofluid dipoles. These two forces are volume forces and their competition is conveniently described by a magnetic length $l_m = \mu_0 M^2/\rho g$. In the magnetic regime, the law describing the meniscus size as a function of $\Delta l_m = l_m(M) - l_m(M_c)$ was found to be linear under weak fields (see Eq. 7.17 and the right-hand side of Fig. 8.1). Both its independent term and its slope are functions of the ferrofluid volume V_{ff}. This linear law allowed us to show that the fields can be considered weak when $M < 21$ kA/m.

From these three chapters and their respective conclusions, we now have all the pieces in hand to draw the final plan of this thesis. Bubbles turned out to be a puzzling and wonderful object that can be manipulated with fields. Due to their unique liquid distribution, a specific part of the bubble can be deformed by choosing an electric or magnetic field. Indeed, while the electric field mainly deforms the spherical shell into an ellipsoid, the magnetic field induces the growth of the meniscus, reshaping the bubble into a spherical cap sitting atop of a cylinder. These deformations are the reasons why bubbles are so well suited to illustrate the nature of the forces acting on them. Moreover, the physical ingredients we have extracted to explain these deformations invite us to return to the comparison proposed in Fig. 1.2 in order to better grasp it. Indeed, what were merely justifications of observations based

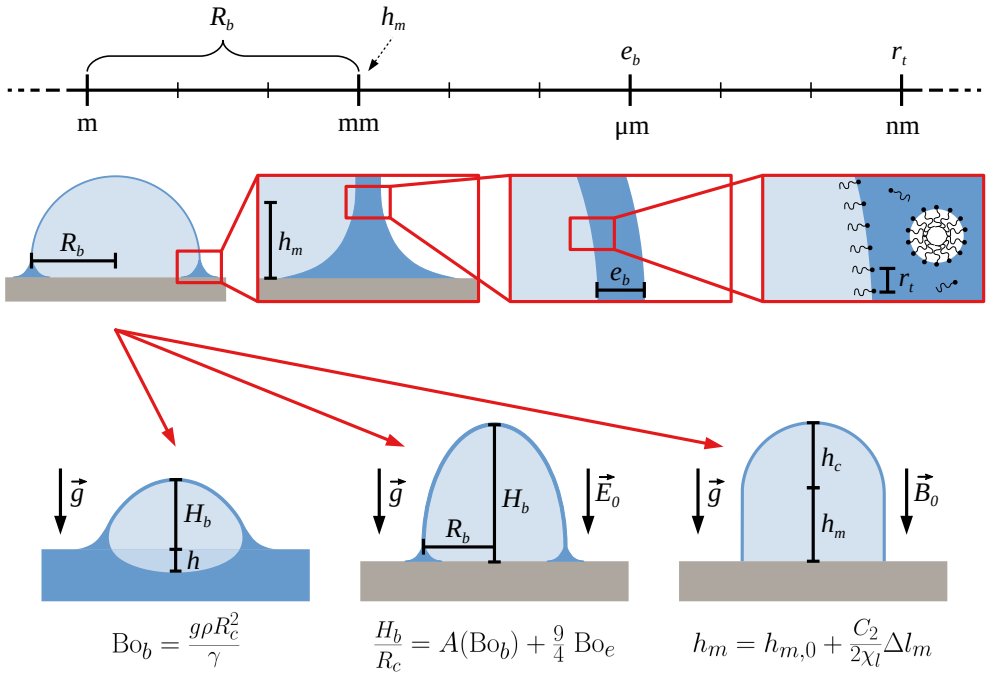

Figure 8.1: Same miniature as presented in Ch. 4 (see Fig. 4.1), except that the chapter corresponding to each deformation studied has been replaced by the relevant dimensionless number or the linear laws obtained. In Ch. 5, we showed that the shape of floating bubbles is completely prescribed by $\mathrm{Bo}_b = g\rho R_c^2/\gamma$, the buoyancy Bond number. In Ch. 6, we found that the deformation of floating or sessile bubbles can be characterised by a pair of dimensionless numbers: Bo_b and $\mathrm{Bo}_e = \varepsilon_0 E_0^2 R_c/2n\gamma$, the electrical Bond number. The law describing these bubbles is linear, the initial shape only depending on Bo_b and the deformation solely on Bo_e. Finally, in Ch. 7, we obtained that the meniscus shape evolves according to two regimes: a capillary regime under very weak fields and a magnetic one. The linear function that defines this shape in the magnetic regime also highlights the presence of the capillary one. On the one hand, the independent term represents the capillary regime and is linked to the capillary length $\kappa^{-1} = \sqrt{\gamma/\rho g}$. On the other hand, the dependent term displays the influence of the magnetic field and is directly proportional to the magnetic length $l_m = \mu_0 M^2/\rho g$.

on our knowledge of the nature of the bubbles and forces have been transformed into laws rationalising these deformations. The similarities and differences between bubbles and droplets under, respectively, an electric or a magnetic field now appear as a natural consequence of these laws. In a sense, we are back to where we started. Yet, the journey we have undertaken has, I hope, given you a better understanding of the equilibria involved in a bubble and has convinced you that the bubble still has every reason to fascinate after so many years.

8.2 New Horizons

The end we reach here is only apparent. Indeed, as the fact that we are returning to where we have began suggests, the road is ahead and it is up to us to start a new journey with our brand new knowledge. While working on bubbles during my thesis, I came across questions that, in my opinion, are worth answering. However, choices had to be made and so we therefore decided not to pursue these ways, despite the fact that they were promising. These questions are presented in what follows, in addition to an ongoing work that I didn't have time to close.

Beyond steady state: the ongoing work is in line with that presented in Ch. 6. In that chapter, we focused on characterising the shape of bubble under an electric field below that needed to trigger a Taylor cone. Yet, the exact electric field for which the Taylor cone is triggered E_T is not easy to obtain. Indeed, as shown in Fig. 6.5, the time required for a bubble to reach its steady state becomes very long as the applied electric field approaches E_T. Similarly, for an electric field just above E_T, the appearance of the Taylor cone is also quite slow. Therefore, at a given potential, the distinction between a bubble slowly progressing towards a Taylor cone or towards a steady shape is rather uneasy. A more accessible method to obtain E_T is based on the following observation: above E_T, the necessary time to trigger the Taylor cone Δt [s] becomes smaller as the difference between the transition and the set potential becomes larger. By measuring Δt as a function of the applied field E_0, we can extract E_T by determining when $\Delta t \to \infty$ or, more conveniently, when $\Delta t^{-1} \to 0$. An example of this measurement is given in Fig. 8.2 for a floating bubble of $V_g = 0.25$ ml inside a capacitor of $d = 15$ mm.

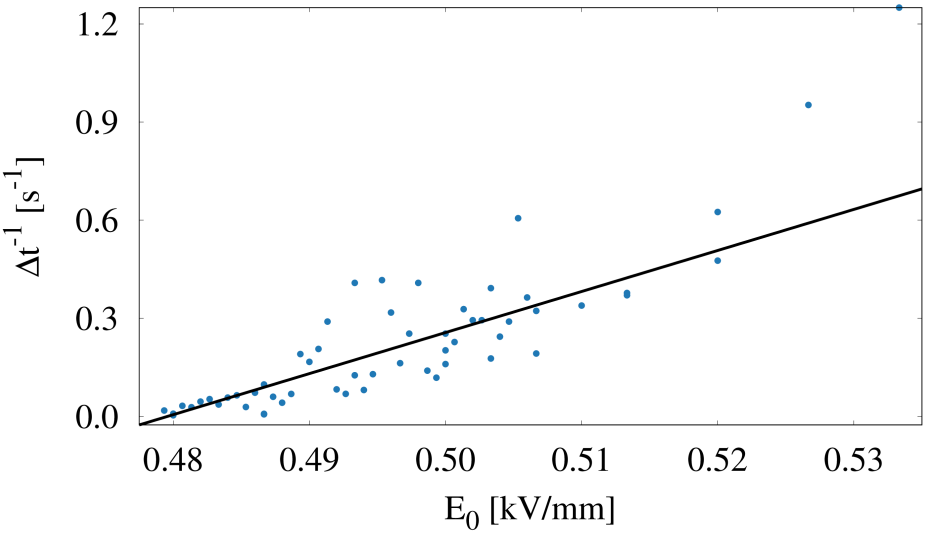

Figure 8.2: Inverse of the time between the application of the potential and the triggering of the Taylor cone Δt^{-1} as a function of the applied electric field E_0. The size of the capacitor was $d = 15$ mm and the volume of the bubble was $V_g = 0.25$ ml. The black line is the fitting function, described by Eq. 8.1, used to obtain the electric field that triggers the Taylor cone E_T. For this experiment, $E_T = 480$ V/mm.

We used a linear function to obtain E_T which reads as follows:

$$\Delta t^{-1} = C(E_0 - E_T), \tag{8.1}$$

with C [m/Vs] and E_T, the two fitting parameters. The E_T obtained and the corresponding Bond numbers Bo_e^* for the five sets of parameters tested are given in Table 8.1.

These results show that both E_T and Bo_e^* depend on the experimental parameters. This means that even if the Bond number was sufficient to describe the deformation of soap bubbles under weak electric fields, it does not allow to characterise the triggering of the Taylor cone. Another physical ingredient is therefore necessary and we suspect that it

V_g [ml]	d [mm]	E_T [V/mm]	Bo_e^* [-]
1.00	15	312 ± 3	$551\ 10^{-4} \pm 1.6\%$
0.50	20	402 ± 1	$772\ 10^{-4} \pm 0.4\%$
0.25	25	480 ± 2	$879\ 10^{-4} \pm 0.8\%$
0.25	25	503 ± 1	$966\ 10^{-4} \pm 0.2\%$
0.25	25	504 ± 2	$972\ 10^{-4} \pm 0.7\%$

Table 8.1: The E_T obtained and the corresponding Bond numbers Bo_e^* for the five sets of parameters considered. The values and the standard deviations are given by adjusting Law 8.1 on each data set. The third row corresponds to the set presented in Fig. 8.2.

is related to the shape of a bubble beyond the transition. Indeed, as Cloupeau *et al.* [94, 95] observed on droplets, there are multiple ways for a bubble to deform when it reaches E_T. As we have said, it can form a Taylor cone vibrating with a greater or lesser amplitude. If the thickness of the capacitor is small enough, it is also possible that the bubble directly touches the upper electrode or to discharges thanks to a spark. We have also observed, as Hilton *et al.* [129] have already pointed out, that a part of the bubble can be torn off without condemning it (see Fig. 8.3). Finally, instead of deforming the whole bubble to form a Taylor cone, the electric field can induce the appearance of a liquid accumulation at the apex of the bubble. Conversely to "conventional" Taylor cone, the liquid is not emitted from the liquid shell, but directly from the accumulation which adopts a shape that has already been numerically obtained by Harris *et al.* [134] for droplets resting at the end of a nozzle. They call this shape a "nipple-like shape" as it closely resembles the nipple of a baby bottle (see Fig. 8.4). This particular configuration leads to a more quiescent bubble because it inhibits its vibration. Clearly, these different kinds of destabilisation should have an impact on the critical field at which the bubble destabilises. Therefore, in order to understand how and at which critical electric field a bubble destabilises, determining which elements induce one instability or another is a mandatory first step.

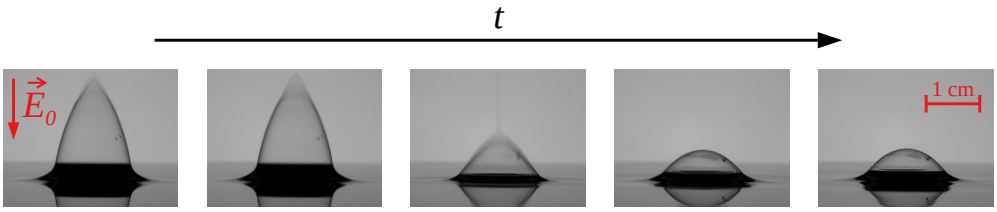

Figure 8.3: Pictures illustrating the removal of part of the bubble and its self-healing under an applied electric field $E_0 = 550$ V/mm generated by a capacitor of thickness $d = 25$ mm. The time between each picture is approximately equal to 0.05 s. On the third picture, the bubble, initially having $V_g = 0.25$ ml, loses a part of its liquid shell, resulting in a drastic decrease of its internal volume. This set of parameters corresponds to the fifth row of Table 8.1.

Electrospray and self-healing abilities: in parallel with these observations and their first analysis, we also recorded the ejections emitted by a bubble under a field $E_0 > E_T$ with an ultra high-speed camera in order to determine their nature. Indeed, if an electrospray is induced on a drop, the liquid emission comes directly from the liquid volume to form tiny droplets. Conversely, when a bubble is subjected to an electrospray, the liquid comes from its liquid shell, possibly inducing differences in the liquid emission. Moreover, the torn liquid could also puncture the bubbles' film. Since it does not automatically blows up when a Taylor cone is triggered, and if a hole is actually induced by the electrospray, the bubble must self-heal. In addition, as presented in Fig. 8.3, a bubble in a Taylor cone state seems to be able to self-heal much larger holes than expected without electric field (see Appendix D). The presence of electric charges and the conical shape of the film induced by the applied electric field could influence the conditions under which this self-healing can occur and explain these enhanced healing abilities.

Charge distribution and liquid flows: beside these experiments on bubbles under a field intensities $E_0 > E_T$, there is also promising investigation that can be done on steady bubbles. For example, there is no experimental verification of the charge distribution along the bubble

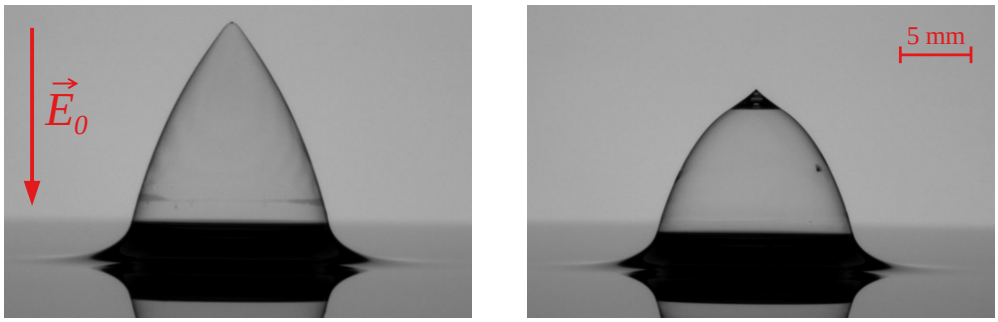

Figure 8.4: Pictures emphasising two possible liquid emissions. The "classical" Taylor cone is depicted on the left-hand side and the nipple-like configuration on the right-hand one. The capacitor thickness and the bubble gas volume in both cases are $d = 25$ mm and $V_g = 0.25$ ml (fifth row of the Table 8.1.). However, the Taylor cone and the nipple configuration are obtained respectively under a field intensity $E_0 = 507$ V/mm and $E_0 = 526$ V/mm.

surface (see Harris *et al.* [134] for numerical results). Obtaining the local charge density experimentally is a challenge, but an astute way to get it could be based on measuring the local curvature of the shell. Through the pressure equilibrium and by measuring both the pressure inside and outside the bubble, the local curvature could be directly linked to the local field and, consequently, to the local charge. In particular, this study could shed light on the impact of the meniscus on the global charge distribution. In addition, Bonhomme *et al.* [139] showed that an electric field applied to a cylindrical soap film induces an electro-osmotic flow. This flux counteracts the natural drainage (see Appendix C) increasing the lifetime of the film. Similar flows can be observed in electrified soap bubbles and to understand them, a good knowledge of the local electric field (and thus of the charge distribution) is a mandatory first step. Furthermore, obtaining the charge distribution could also be a way to physically justify the weak fields limit and to propose a law that describes the deformation of bubbles beyond this limit.

Influence of the ferrofluid nature and the liquid volume: the experiments performed to determine the shape of magnetic bub-

bles also raise unresolved questions. As with the bubbles under electric field, physically explaining the weak fields limits is the next step in the reflection. In addition, this study could help propose a law based on the whole magnetisation curve that describes the meniscus size at any magnetisation. Furthermore, submitting bubbles floating on their own ferrofluid to a magnetic field could help us complete the picture drawn in the Ch. 7. This presumption is based on Fig. 7.10 and 7.11, which suggest that the values of $h_{m,0}$ and C_2 could reach saturation for an infinite amount of liquid. Floating bubbles therefore seem perfectly suited to obtain these values and get rid of the influence that V_{ff} has on the phenomenon. This interrogation, which at first sight seems to be linked only to bubbles under magnetic field, is in fact much more general. Indeed, although much has already been done to define the bubbles shape without any other field applied than gravity, nobody has studied the impact of the volume of liquid used to create the bubble on its shape. In Ch. 7, we saw that V_{ff} clearly impacts the meniscus shape and height, but it could also have an impact on the overall shape of the bubble. Moreover, in Ch. 6, we noticed that even when the depth of the liquid bath e on which a bubble floats is smaller than its penetration depth h, the overall shape of the bubble closely resembles that of a non-frustrated floating one. These two observations lead to the following question: what defines a floating or a sessile bubble? Indeed, what we have perceived throughout our thesis as two mutually exclusive states of a bubble appears rather as a continuum. The study of the influence of the liquid volume on the bubble could help determine whether there is an abrupt transition between sessile and floating bubbles and, if so, what characterises it.

As my final words, I would simply like to say that, even if they may be seen at first sight as a scientific or artistic curiosity, or even a child's toy, bubbles are a puzzling and fascinating object of study which, although it is not always taken seriously[1], reveal complex physical phenomena. The few perspectives developed here show that there are still many questions to be answered and potential applications to be found. All I hope is that the concepts developed in this thesis can serve

[1]I have lost count of the number of times I have had to confirm that I am actually working on soap bubbles and that this is not some kind of joke.

as a starting point for new fascinating discoveries on fluid manipulation with fields and more specifically in or with bubbles.

A

Shape of a Sessile Droplet

As explained in the main text of the thesis, the shape transition undergone by a droplet arises from the competition between gravity and surface tension. On the one hand, gravity favours the flattening of the liquid to minimise its height. On the other hand, surface tension aims to reduce the interface between air and water, in other words to reduce the surface of the droplets. Since the minimum surface for a given volume is a sphere, any deformation from a spherical shape, such as, for example, flattening, increases the surface of the droplet. Thus, gravity and surface tension, described by hydrostatic and Laplace pressure respectively, counteract each other. The hydrostatic pressure scales with the depth of the liquid and therefore with the droplet size ($P_h = \rho g z$). In addition, the Laplace pressure scales with the curvature of the liquid and thus with the inverse of the droplet size ($P_\gamma = \gamma\ \mathcal{C}$). The effect of surface tension, namely the area minimisation, should accordingly be dominant for small droplets, leading to a shape close to a hemisphere. Conversely, the shape of larger droplets is prescribed by the hydrostatic pressure, inducing the height minimisation and the formation of puddles[1].

Mathematically, this transition in shape can be rationalised by com-

[1]Since, in general, neither the hydrostatic pressure nor the Laplace one is constant within the droplet bulk (neither the depth nor the curvature is constant), the complete description of the droplet profile requires finding the equilibrium through a force equation (for a resolution, see Ref. [30] page 40 to 42, for example

paring the effects of the Laplace pressure induced by a given curvature $\mathcal{C}$, namely $P_\gamma = \gamma\ \mathcal{C}$ with those due to the hydrostatic pressure at a depth $\mathcal{C}^{-1}$, *i.e.* $P_h = \rho g\ \mathcal{C}^{-1}$. Dividing one by the other allows us to define of the dimensionless number that compares the gravitational and capillary effects: the Bond number

$$\mathrm{Bo} = \rho g\ \mathcal{C}^{-2}/\gamma. \tag{A.1}$$

If $\mathrm{Bo} \gg 1$, gravity effects are dominant in the studied system and the capillary ones can be neglected in their respect. Reciprocally, when $\mathrm{Bo} \ll 1$, capillary effects take precedence over gravity ones. As the Bo scale with the square of the length, the larger the drop, the more likely it is to be influenced by gravity. The transition between the two regimes occurs when $\mathrm{Bo} = 1$, *i.e.* when the two pressures are equal, leading to the definition of the capillary length κ^{-1} by Eq. 3.3.

To complete the description of the droplet shape in Fig. 3.1, a last effect must be address. This phenomenon takes place at the junction line between the solid substrate, the liquid and the surrounding gas and fixes the contact angle between the substrate and the liquid phase at the junction. This property, called wetting, arises from capillary effects between not only the liquid and the air but also between the solid and the air as well as between the solid and the liquid. To explain it in a simple way, the spreading of a liquid on a solid replaces a pre-existing interface by two others: a solid/gas interface is substituted by a solid/liquid and a liquid/gas one. If the total energy of the system is decreased thanks to the creation of the two interfaces, the liquid spreads all over the solid, forming a nanometric layer in order to maximise the gain in energy. This phenomenon is called "total wetting" because the liquid totally wets the substrate and is represented in Fig. A.1 (a). Conversely, if the formation of the two interfaces is energy costly, the liquid forms a droplet on the surface, leading to the situation illustrated in Fig. 3.1 and drawn in Fig. A.1 (b-c). This is situation is called "partial wetting".

The contact angle θ_c [°] between the substrate and the liquid droplet at the junction between three phases results from the equilibrium between the three interfacial tensions, the liquid/solid, the solid/air and the liquid/air tension (the last one corresponding to the surface tension already defined). If the contact angle with a given liquid θ_c is less than

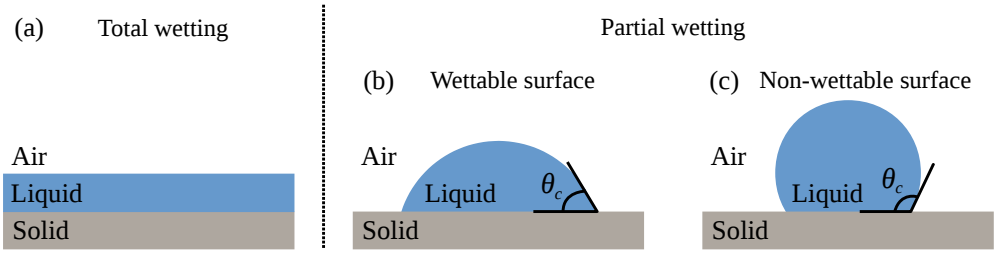

Figure A.1: Sketches representing the different behaviours that a liquid can adopt when deposited on a solid surface. (a) If the substitution of the solid/air interface with two other, one solid/liquid, one liquid/air, decreases the total energy of the system, the liquid spreads over the whole surface, totally wetting it. On the contrary, when the replacement of the initial interface by two new ones is energy costly, a droplet of liquid is formed. (b) On a wettable surface, the contact angle $\theta_c < 90°$. (c) On a non-wettable surface, the contact angle $\theta_c > 90°$.

90° (see Fig. A.1 (b)), the surface is said to have a high wettability, with this given liquid. Conversely, if θ_c is greater than 90° (see Fig. A.1 (c)), the surface has low wettability. For water, surfaces with high wettability are called hydrophilic surfaces while those with low wettability are designated as hydrophobic. There is even a third category for surfaces whose θ_c is close to 180°: superhydrophobic surfaces. A well-known example of a superhydrophobic surface is the lotus leaf, on which water droplets roll thanks to the texture of its surface, which gives it self-cleaning properties [140, 141]. A more complete explanation can be found in these two references [30, 29]. Furthermore, it should be noted that, even if the apparent contact angle is modified by an applied external field (like a magnetic or an electric one), there is practically no change in the liquid/medium or liquid/substrate interfacial tension. The electrowetting phenomenon, as well as the magnetowetting one, is mainly due to electrostatic or magnetostatic pressures deforming the general shape of the droplet [142, 143, 118].

To sum up, the shape of a liquid on a solid primarily depends on the wettability of the substrate: if the liquid does not completely wet the

substrate, it forms a droplet. The contact angle between the droplet and the substrate depends on the wettability of the surface, while the overall shape of the droplet depends on its size. If its characteristic size is smaller than the capillary length, its shape is imposed by capillary effects and the droplet forms a spherical cap. Conversely, if the characteristic length is greater than the capillary length, the shape is dictated by the gravity and tends to spread out, forming a puddle.

B
Amphiphilic Molecules

Amphiphilic molecules, also called surfactant molecules due to their effect on the surface tension, are so named because of their interaction with water. Indeed, when particles are added to water, they may or may not dissolve in the water. As the H_2O molecules are highly polarised, polar molecules or ions have a strong affinity with water and are soluble in it. They are called hydrophilic particles. Conversely, apolar particles are insoluble in water and are therefore named hydrophobic particles. There is also a third possibility, right on the edge of the first two, which can occur for more complex molecules. This intermediate case appears when part of the molecule is polar and therefore hydrophilic, whereas the rest of it is apolar and thus hydrophobic. A sketch of one of these molecules is drawn in the right part of Fig. 5.1. They are amphiphilic molecules and, due to their particular configuration, they agglomerate at the interface. Indeed, at the interface, amphiphilic molecules can minimise their global energy by orienting themselves in such a way that the polar heads remain in the water while the apolar tails are in the air. Aggregating naturally at the interface, these molecules greatly influence the surface tension, justifying their name of surfactant molecule, by decreasing it from 72 mN/m to ~ 20 mN/m in the case of soap diluted in water. This decrease is induced by the fact that the surfactant molecules soften the transition between water and air. As the concentration of surfactant molecule increase, the surface tension decreases, until reaching

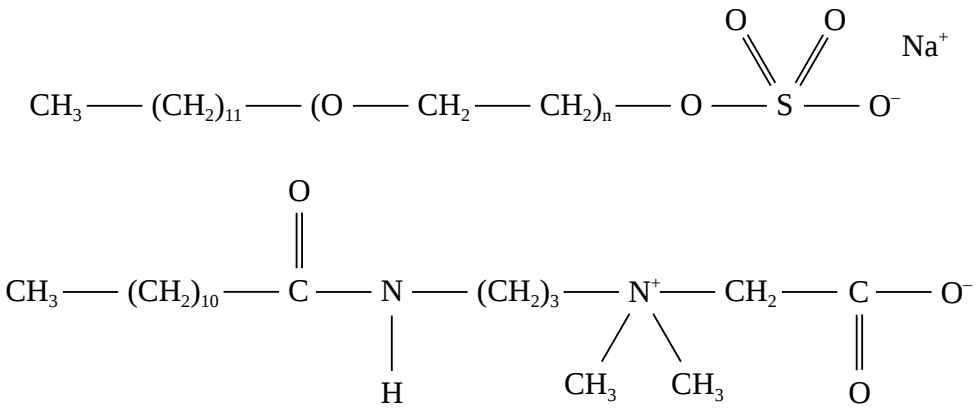

Figure B.1: Semi-developed chemical formulæ of SLES, an anionic surfactant (top) and CABP, a zwitterionic one (bottom), both used in Denkov's soap.

a saturation.

This saturation occurs when, instead of agglomerating at the congested interface, the surfactant molecules self-assemble to form a structure in the bulk. The simplest structure[1] in which these molecules can assemble is a spherical shell with all the heads facing outwards, thus avoiding contact between the inner apolar tails and water. These structures are known as micelles and the concentration at which they start to form is the Critical Micelle Concentration (hereinafter refereed to as CMC). The surfactants concentrations in the solutions used in this thesis are higher than the CMC and therefore saturation of the surface tension is always achieved, making it less sensitive to changes in concentration. An enlargement of the situation inside the liquid film forming a bubble is presented on the left part of Fig. 5.1. Most surfactant molecules aggregate at the interface, stiffening it, but others are diluted in the bulk or form micelles.

Two types of soaps are used in this thesis: Denkov's soap and ferrofluid soap. The former is a surfactant mixture based on the stock solu-

[1]Other structures are also possible, such as the well-known bilayer that separates a cell from its surroundings.

tions formulated in [66]: the stock solution is composed of two types surfactant molecules. Specifically, 6.6 wt % of sodium lauryl-dioxyethylene sulfate (SLES from Stepan Company) and 3.4 wt % of cocoamidopropyl betaine (CAPB from Evonik Industrie) are diluted with water. Next, 0.4 wt % of myristic acid (MAc from Roth Carl) was dissolved by heating the mixture up to 60 . Finally, in order to increase the viscosity of the final mixture, the stock solution was diluted 10 times in a mixture 60 wt % of glycerol (from Sigma-Aldrich) and 40 wt % of distilled water. The semi-developed chemical formulæ of both surfactant molecules are represented in Fig. B.1. SLES is an anionic surfactant, which means that the polar head (the OSO_3 group) bears a negative charge, whereas CPAB is zwitterionic, meaning the polar head is polarised, bearing both a positive and a negative charge on two non-adjacent atoms. It the case of CAPB, the positive charge is located on the nitrogen atom while the negative charge is carried by one of the oxygen atom in the CO_2 group. The combination of two surfactant molecules, a fatty acid and a viscous solvent allows us to obtain bubbles that may last for hours when blown from the resulting mixture. The viscosity of the solution described is $\eta = 10.5\ 10^{-3}$Pa s at 22 according to a Haake MARS III rheometer. The surface tension, measured using the pendant drop method [144] (CAM 200 model from KSV Instrument), and the density of the mixture are given in Table 3.1.

The ferrofluid soap is also a surfactant mixture, which has already been used by Elias *et al.* [65]. The solution consists of a water-based ferrofluid of maghemite particles ($\gamma-Fe_2O_3$) to which 2 wt % of a surfactant, the sodium dodecyl sulfate (SDS), has been added. SDS is, like SLES, an anionic surfactant with a negatively charged polar head.

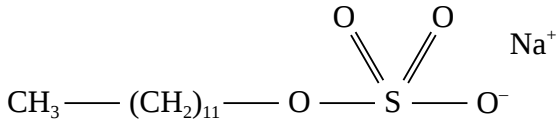

Figure B.2: Semi-developed chemical formula of SDS, an anionic surfactant used in the ferrofluid soap.

Its semi-developed chemical formula is represented in Fig. B.2. As the maghemite particles are surrounded by negative electrostatic charges to stabilise the solution, they are repelled by the SDS molecule preventing their agglomeration at the interface. The physical properties, obtained directly from Ref. [65], are given in Table 3.1. Moreover, the viscosity is estimated to be $\eta \approx 20\ 10^{-3}$Pa s.

C Bubbles Life

Although the main objective of the thesis is the steady shape reached by a bubble after being deformed by an external field, achieving this stable shape does not ensure that there is no flow inside the liquid shell forming the bubble nor that this flow is stationary. The flow within the liquid shell is a complex dynamic process that is highly dependent of the liquid nature in which the bubbles are made. These processes greatly influenced the choice of soap we made to carry out our experiments and are briefly explained in this appendix. It should be noted that the drainage dynamics are certainly modified by the external electric or magnetic field, but the description of this influence is beyond the scope of this thesis.

C.1 Life of "Bare" Bubbles

Even if it is technically possible to create a film of water to form a bubble, the object formed collapses almost instantly on itself due to gravity and surface tension induced drainage of the film and the resulting shrinkage. Indeed, even though gravity has no effect on the overall shape of the bubble, it does drain the liquid towards the bottom of the film due to its mass. Moreover, the liquid inside the film is subjected to an excess of pressure P_l due to the curvature of the interface. Comparatively, at the base of the bubble, inside the meniscus, as the radius of curvature points

outwards the liquid, the pressure is lower than the external pressure. As the pressure inside the meniscus is lower than the one inside the film, the liquid is drained towards the meniscus by capillarity.

Therefore, both effects drain the liquid from the film to the base of the bubble, which eventually leads to its death. To find out which is dominant, the Bond number Bo and the capillary length κ^{-1} can be used. Indeed, the two pressures being compared are the pressure due to the bubble curvature and the one due to weight of a "column" of liquid. Since, in a bubble, the radius related to the curvature is also the typical height of the liquid column, the two pressures are equal when the radius $R_c \approx \kappa^{-1}$ (conversely, when the general bubble shape is analysed, the relevant parameter is the weight of a thickness e_b inducing the flattening of the bubble which leads to the definition of $\varkappa^{-1}$). In our experiments, the bubbles have an $R_b \gg \kappa^{-1}$, consequently the drainage is dominated by gravity (see Table 3.1). For bubble of "bare" liquid drained by the gravity, Debrégas *et al.* [145] assumed fully mobile interfaces, inducing free-fall drainage and thus plug flow within the film[1]. Yet, the flow speed is constant at a given bubble latitude leading to an exponential decay of the film thickness at the bubble apex, characterise by

$$e_b(t) = e_{b,0}\, e^{-t/\tau_v} \qquad \text{with} \qquad \tau_v = \frac{\eta}{\rho g R_c} \tag{C.1}$$

and $e_{b,0}$ [m] the initial film thickness. As water have a viscosity of $\eta \sim 10^{-3}$ Pa s and for a bubble of $R_c \sim 5$ mm, the characteristic shrinkage time $\tau_v \approx 10^{-5}$ s, which means that a bubble of water blows up almost instantaneously. Conversely, Debrégas *et al.* [145] showed that bubbles of highly viscous liquid (such as melten polydimethylsiloxane or lava) can have a long lifetime. However, from our daily experience, we know that long-lived bubbles can be obtained in liquid of lower viscosity such as soap. These bubbles owe their long life to the amphiphilic molecules.

[1]Indeed, as the interface falls with the entire liquid volume in the air, which has a negligible viscosity compared to that of the liquid, there is no stress at the interface.

C.2 Life of Soap Bubbles

The presence of surfactant molecules within the mixture drastically changes the draining behaviour and therefore the characteristic bubble life span. Indeed, as pointed out by Lhuissier *et al.* [126], even an extremely small amount of surfactant molecule is able to maintain the bubble integrity for a far longer time than would be expected on the basis of viscosity alone. They studied the case of bubble formed with tap water, which has typically a surface tension of 1 mN/m less than that of pure water, and are able to obtain bubbles that last up to 40 s. This radical change is achieved through the establishment of a surfactant molecules gradient that induce a surface tension gradient during the early time of the bubble's life. During this initial phase, the surfactant molecules are drag down to the bubble foot with the primary flow. As the surface tension increases with decreasing surfactant concentration, the surface tension at the bubble apex become greater than at its foot and a Marangoni flow counteracting the drainage is established.

The authors also showed that, after the establishment of the surface tension gradient, a second drainage regime follows the first. This second regime is completely prescribe by the flow within a pinch region at the junction between the meniscus and the liquid cap. This pinch region has been studied by Aradian *et al.* [146], who showed that its origin is due the flow induced by the pressure difference between the cap and the meniscus. These thinner parts eventually rise towards the bubble apex to replace the thicker zones, in a phenomenon called marginal regeneration, thus ensuring the mass conservation [147]. The liquid flux inside the pinch and the marginal regeneration are coupled and Lhuissier *et al.* [126] observed that their combined effect drives the drainage of bubbles consisting of highly diluted surfactant solution.

However, they postulate that marginal regeneration can only occur in bubbles blown from a dilute surfactant solution as it imparts mobile behaviour to the liquid film. In contrast, surfactant-saturated soap bubbles, such as the one we used in our experiments, cannot experience destabilisation of the pinch region and then marginal regeneration. Therefore, their drainage mechanism is no longer valid when the surfactant concentration increases. Yet, our observations as well as those made

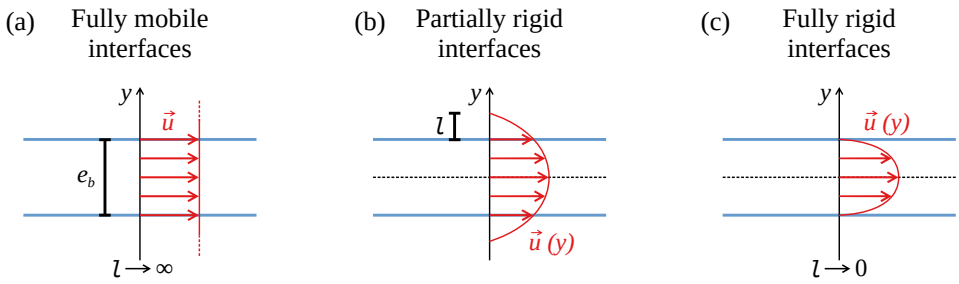

Figure C.1: Sketches of the different drainage profiles within the soap film of thickness e_b as a function of interface mobility. (a) Fully mobile interfaces lead to a plug flow, namely a constant fluid velocity $\vec{u}$ over the whole interface thickness and the extrapolation length l tends, accordingly, to infinity. (b) Partially rigid interfaces induce a variation of the velocity $\vec{u}(y)$ along the direction perpendicular to the interface like a classical Poiseuille flow. However, even if the velocity is maximal at the centre of the interface, it does not cancel out at its extremities. The length l takes on a finite value and can thus allow these flows to be fully characterised. (c) Totally rigid interfaces are described by a classical Poiseuille flow with a null velocity at the interface extremities and a length l tending towards zero.

by Champougny *et al.* [148] reveals that marginal regeneration is always present regardless of surfactant concentration. This suggests that, rather than being non-existent, marginal regeneration is dominated by another phenomenon as the surfactant concentration increases.

In the same article, Champougny *et al.* succeed in describing the gravity-induced drainage of bubbles consisting of a soap solution, regardless of their surfactant concentration. As the surfactant concentration greatly influences the surface mobility, they model the drainage with a partially rigid interface. In this model, the interfaces move with a fraction of the liquid velocity at the centre of the film. The velocity profile resulting from this model (see Fig. C.1 (b)) is in between a plug flow, representing drainage with fully mobile interfaces, such as "bare" bubbles (see Fig. C.1 (a)), and a classical Poiseuille flow, expected in

the case of fully rigid interfaces (see Fig. C.1 (c)). This hybrid flow is characterised by a symmetric velocity profile forming a parabola, as in the classical Poiseuille flow, but with a non-zero velocity at the interface. Accordingly, it can equivalently be defined thanks to an extrapolation length l [m] which is the distance between the interface and the point where the tangential velocity $\vec{u}(y)$ goes to zero. This distance l varies from zero for a classical Poiseuille flow to infinity for a plug one. When the interfaces are quite mobile, namely when $l \gg e_b/2$, the drainage is close to that observed in case of "bare" bubbles. Accordingly, the film thickness at the bubble apex experiences an exponential decay characterised by

$$e_b(t) = e_{b,0}\ e^{-t/\tau_m} \qquad \text{with} \qquad \tau_m = \frac{\eta R_c}{\rho g l^2}, \tag{C.2}$$

the characteristic shrinkage time for mobile interfaces (measured in [s]). Bubbles made of ferrofluid soap exhibit this behaviour and have a typical lifetime of one minute. Conversely, when the interfaces are almost perfectly rigid, $l \ll e_b/2$ and the flow can be assimilated to a classical Poiseuille one, inducing an algebraic decay:

$$e_b(t) = \frac{e_{b,0}}{\sqrt{1 + t/3\tau_r}} \qquad \text{with} \qquad \tau_r = \frac{\eta R_c}{\rho g e_{b,0}^2}, \tag{C.3}$$

the characteristic shrinkage time for rigid interfaces (measured in [s]). Bubbles made of Denkov's solution belong to this regime, allowing them to reach lifetimes of the order of an hour. It should be noted that, in general, the drainage dynamics of a surface bubble does not solely depend of the surfactant concentration, but also on the bubble size as numerically studied by Atasi *et al.* [149]. Indeed, when the size of the bubble changes, the dominant drainage mechanism could switch from gravity to capillarity. Furthermore, the bubble shape is predicted by its size and this also has an impact on the drainage.

D
Bubbles Death

The drainage of a soap bubble induces the thinning of its liquid shell. As it is known from our daily experience, this thickness reduction eventually leads to the nucleation of a hole inside the bubble, potentially driving it to its death. Indeed, when a hole is punctured inside the liquid shell, two capillary pressures counteract each other. On the one hand, the pressure induced by the curvature of the circular hole itself P_c [N/m^2] (with F_c [N] the associated force) tends to close it. On the other hand, the curvature of the liquid film around the hole generates a pressure P_o [N/m^2] (with F_o [N] the associated force), which tends to open the hole[1]. These two capillary pressures are respectively $P_c \sim \gamma/R_h$, with R_h [m] the hole radius and $P_o \sim 2\gamma/e_b$, with $e_b/2$ the typical magnitude of the curvature radius of the liquid film at its rupture. If the radius of the hole is smaller than the half thickness, the closing pressure is larger than the opening one and the hole closes, in a kind of self-healing fashion. However, when $R_h > e_b/2$ the hole opens, further increasing the pressure difference and causing the bubble to burst. The minimum

[1]It should be noted that there is, strictly speaking, a third curvature, that of the soap film forming the bubble, whose radius is directed towards the centre of the bubble. However, since the size of the bubble is at least two orders of magnitude larger than the thickness of its film, this curvature contributes negligibly to the closing pressure. It is therefore reasonable to assume that the hole is contained in a plane tangential to the bubble surface.

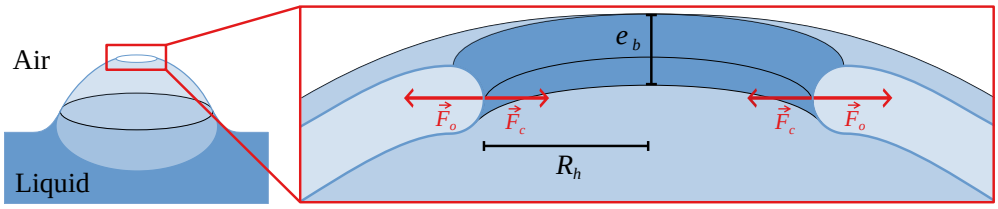

Figure D.1: Sketch of a hole puncture inside the liquid cap forming the bubble. The pressure driving its opening is $P_o \sim 2\gamma/e_b$, with $e_b/2$ the typical curvature radius of the film thickness at its rupture. Conversely, the closing pressure is $P_c \sim \gamma/R_h$, with R_h the curvature radius of the hole. When $e_b/2 < R_h$, $P_o > P_c$ and the hole expands, eventually leading to the bubble death. The forces F_o and F_c, respectively associated with P_o and P_c, are represented in red.

required energy to prompt the hole nucleation is, therefore, of the order of $\gamma e_b^2 \sim 10^{-12}$J.

Nevertheless, the origin of this puncturing energy remains unsettled. Indeed, as it was showed by Lhuissier *et al.* [126] for bubble with a vanishing amount of surfactant, the involving energies due to thermal or velocity fluctuations are not sufficient to fuel the hole nucleation. Moreover, Van der Waals forces are only effective in puncturing very thin films of tens of nanometres, which is far smaller than the typical e_b, namely few micrometres. Furthermore, the lifetime of these bubbles appears to be partially stochastic, although the laws governing drainage are purely deterministic [148, 150], suggesting the absence of a direct link between the time at which the rupture occurs and e_b. Poulain *et al.* [150] rationalise this apparent discrepancy by coupling deterministic drainage with local stochastic perturbations. These perturbations can either be extrinsic, such as violent air flow or droplet and dust impacts, or intrinsic, such as microbubbles and dirt already present in the solution. They locally modify the surface tension inducing a Marangoni stress. These stresses themselves induces a divergent flow, eventually leading to the film thinning [151]. Once thinned, the film is more likely to be broken by thermal fluctuation or Van der Waals forces. Since disturbances are ubiquitous, but stochastic, this explanation justifies the

stochastic nature of the bubble lifetime.

Furthermore, Champougny *et al.* [148] show that, in addition to increasing the lifetime of the bubble, the surfactant concentration seems to decrease the stochastic nature of this lifetime. This observation is concomitant with a change in the nucleation point from a random distribution near the foot of the bubble (as observed by Lhuissier *et al.* [126]), to a systematic explosion at the bubble apex[2]. Bubbles consisting of a surfactant-saturated solution thus have a deterministic lifetime and are much more robust to surface disturbances, whereas low-concentrated bubbles exhibit opposite trends. The transition between these two regimes occurs at the CMC, further confirms the importance of the nature of the bubbles interfaces on their life. This conclusion is reinforced by the work presented by Rio and Biance [152] who list the different times involving in soap film coalescence and show the drastic difference that the interfaces rigidity induces on these times. Finally, Champougny *et al.* show in another article [153] that evaporation also has an effect on the break-up of a soap film, even if it has no impact on the film thinning.

After the puncturing of the film, if the hole is large enough to induce its opening, the hole grows at a constant speed which solely depends on the liquid properties and film thickness. This speed u_o [m/s] have been independently derived by Taylor and Culick [154, 155] and is written as follows

$$u_o = \sqrt{\frac{2\gamma}{\rho e_b}}. \tag{D.1}$$

The hole opening induce an accumulation of liquid at its edge and the expression for the speed is obtained by evaluating the work done by the capillary forces on this accumulation of liquid, assuming that there is no disturbance of the film away from the hole. This work must supply not only the kinetic energy of edge, but also the energy needed to accelerate

[2]It is important to note that Debregeas *et al.* [145] showed that bubbles without surfactant also explode at their apex. There is therefore a discontinuity between bubbles with a low surfactant concentration and bubbles made of pure liquid, even though their drainage profiles are very close. This observation seems to support the assumption that the rupture of low-concentrated bubbles is due to local disturbances, whereas pure and highly concentrated bubbles die due to gravity induced drainage.

the initially still liquid. McEntee *et al.* [156] experimentally verified the relationship between the film thickness and the opening speed and show a good agreement for films up to 0.1 µm thickness. The measurement of this opening speed is therefore a regularly used means to measure the thickness of the liquid cap [6, 147].

References

[1] A. Frey, *The Soap Bubble Trope*, (2021) DAILY.JSTOR.ORG/THE-SOAP-BUBBLE-TROPE/ (visited 2022-09-26).

[2] I. Newton, *Opticks* (Project Gutenberg, 2010).

[3] C.V. Boys, *LI. Experiments with soap-bubbles*, Lond. Edinb. Dublin philos. mag. j. sci. **25**, 409 (1888).

[4] C.V.Boys, *Soap-Bubbles and the Forces Which Mould Them* (Project Gutenberg, 2010).

[5] C. Isenberg, *The Science of Soap Films and Soap Bubbles* (Dover Publications, New York, United States, 1992).

[6] C. Cohen, B.D. Texier, E. Reyssat, J.H. Snoeijer, D. Quéré and C. Clanet, *On the Shape of Giant Soap Bubbles*, Proc. Natl. Acad. Sci. U.S.A. **114**, 2515 (2017).

[7] M.A.C. Teixeira and P.I.C. Teixeira, *Contact angle of a hemispherical bubble: An analytical approach*, J. Colloid Interface Sci. **338**, 193 (2009).

[8] M.A.C. Teixeira, S. Arscott, S.J. Cox and P.I.C. Teixeira, *What is the Shape of an Air Bubble on a Liquid Surface?*, Langmuir **31**, 13708 (2015).

[9] C.T.R. Wilson and G.I. Taylor, *The Bursting of Soap-bubbles in a Uniform Electric Field*, Math. Proc. Camb. Philos. Soc. **22**, 728 (1925).

[10] W.A. Macky, *Deformation of Soap Bubbles in Electric Fields*, Math. Proc. Camb. Philos. Soc. **26**, 421 (1930).

[11] J. Kuneš, *Dimensionless Physical Quantities in Science and Engineering* (Elsevier, London, United Kingdom, 2012).

[12] J. Beroz, A.J. Hart and J.W.M. Bush, *Stability Limit of Electrified Droplets*, Phys. Rev. Lett. **122**, 244501 (2019).

[13] J.V.I. Timonen, M. Latikka, L. Leibler, R.H.A. Ras and O. Ikkala, *Switchable Static and Dynamic Self-Assembly of Magnetic Droplets on Superhydrophobic Surfaces*, Science **341**, 253 (2013).

[14] S. Mawet, H. Caps and S. Dorbolo, *Deformation of soap bubbles in uniform electric fields*, Phys. Rev. Fluids **6**, 043603 (2021).

[15] I. Newton, *PhilosophiæNaturalis Principia Mathematica* Trans. by A. Motte (Daniel Adee, York, United States, 1846).

[16] L.G. Leal, *Advanced Transport Phenomena: Fluid Mechanics and Convective Transport Processes* (Cambridge University Cambridge, United Kingdom, adresse, 2007).

[17] E. Guazzelli, J.F. Morris and S. Pic, *A Physical Introduction to Suspension Dynamics* (Cambridge University Press, Cambridge, UK, 2011).

[18] B. Lautrup, *Physics of Continuous Matter* (CRC Press, Boca Raton, United States, 2011).

[19] G. De Moor and J.-C. André, *Navier, un honnête homme de la mécanique, et les équations de Navier-Stokes*, La Météorologie **50**, 51 (2005).

[20] Marc Thiriet, *Biology and Mechanics of Blood Flows, Part II* (Springer, New York, United States, 2008).

[21] E. Guyon, J.-P. Hulin and L. Petit, *Hydrodynamique Physique* (Dover Publications, Paris, France, 2001).

[22] G.K. Batchelor, *An Introduction to Fluid Dynamics* (Cambridge University Press, Cambridge, United Kingdom, 2000).

[23] P.-S. de Laplace, *Traité de mécanique céleste* (Courcier, Paris, France, 1805).

[24] T. Young, *III. An essay on the cohesion of fluids*, Philos. Trans. Royal Soc. A **95**, 65 (1805).

[25] N. Adami and H. Caps, *Capillary-driven two-dimensional buoyancy in vertical soap films*, EPL **106**, 46001 (2014).

[26] A. Pockels, *Surface Tension* Trans. by Lord Rayleigh, Nature **43**, 437 (1891).

[27] A. Pockels, *On the Relative Contamination of the Water-Surface by Equal Quantities of Different Substances*, Nature **46**, 418 (1892).

[28] A. Pockels, *Relations Between the Surface-Tension and Relative Contamination of Water Surfaces*, Nature **48**, 152 (1893).

[29] A. Marchand, J.H. Weijs, J.H. Snoeijer and B. Andreotti, *Why is surface tension a force parallel to the interface?*, Am. J. Phys. **79**, 999 (2011).

[30] P.-G. de Gennes, F. Brochard-Wyart and D. Quéré, *Gouttes, bulles, perles et ondes* (Édition Belin, Paris, France, 2005).

[31] L.D. Landau and E. M. Lifshitz, *Course of theoretical physics: Fluid Mechanics* Trans. by J.B. Sykes and W.H. Reid (Pergamon Press, Oxford, United Kingdom, 1966).

[32] A. Cazaubiel, S. Mawet, A. Darras, G. Grosjean, J.J.W.A. van Loon, S. Dorbolo and E. Falcon , *Wave Turbulence on the Surface of a Fluid in a High-Gravity Environment*, Phys. Rev. Lett. **123**, 244501 (2019).

[33] C. Falcón, E. Falcon, U. Bortolozzo and S. Fauve, *Capillary wave turbulence on a spherical fluid surface in low gravity*, EPL **86**, 14002 (2009).

[34] M. Berhanu, E. Falcon, G. Michel, C. Gissinger and S. Fauve, *Capillary wave turbulence experiments in microgravity*, EPL **128**, 34001 (2020).

[35] W. Gilbert, *De Magnete* Trans. by P. Fleury Mottelay (Dover Publications, New York, United States, 1963).

[36] G.I. Taylor, *Disintegration of Water Drops in an Electric Field*, Proc. R. Soc. Lond. A **280**, 383 (1964).

[37] J.R. Melcher and G.I. Taylor, *Electrohydrodynamics: A Review of the Role of Interfacial Shear Stresses*, Annu. Rev. Fluid Mech **1**, 111 (1969).

[38] S.D. Pawar, P. Murugavel and D.M. Lal, *Effect of Relative Humidity and Sea Level Pressure on Electrical Conductivity of Air over Indian Ocean*, J. Geophys. Res. Atmos. **114**, D02205 (2009).

[39] G.I. Taylor and A.D. McEwan, *The stability of a horizontal fluid interface in a vertical electric field*, J. Fluid Mech. **22**, 1 (1965).

[40] L.D. Landau and E.M. Lifshitz, *Course of theoretical physics: Electrodynamics of Continuous Media* Trans. by J.B. Sykes, J.S. Bell and M.J. Kearsley (Pergamon Press, Oxford, United Kingdom, 1984).

[41] B. Apffel and E. Fort, *Frequency Conversion Cascade by Crossing Multiple Space and Time Interfaces*, Phys. Rev. Lett. **128**, 064501 (2022).

[42] G. Néron de Surgy, J.-P. Chabrerie, O. Denoux and J. Wesfreid, *Linear growth of instabilities on a liquid metal under normal electric field*, J. Phys II France **3**, 1201 (1993).

[43] A. Onuki, *Interface instability induced by an electric field in fluids*, Physica A **217**, 38 (1995).

[44] E. Schäffer, T. Thurn-Albrecht, T. Russell and U. Steiner, *Electrically induced structure formation and pattern transfer*, Nature **403**, 874 (2000).

[45] E. Schäffer, T. Thurn-Albrecht, T. Russell and U. Steiner, *Electrohydrodynamic instabilities in polymer films*, EPL **53**, 518 (2001).

[46] M. Firouznia and D. Saintillan, *Electrohydrodynamic instabilities in freely suspended viscous films under normal electric fields*, Phys. Rev. Fluids **6**, 103703 (2021).

[47] V.A. Briskman and G.F. Shaidurov, *Parametric Instability of a Fluid Surface in an Alternating Electric Field*, Dokl. Phys. **13**, 540 (1968).

[48] R.J. Raco and R.L. Peskin, *Stability of a Plane Fluid Interface in the Presence of a Transverse Electrostatic Field*, Phys. Fluids **12**, 568 (1969).

[49] C.-S. Yih, *Stability of a Horizontal Fluid Interface in a Periodic Vertical Electric Field*, Phys. Fluids **11**, 1147 (1968).

[50] M.V. Berry and A.K. Geim, *Of flying frogs and levitrons*, Eur. J. Phys **18**, 307 (1997).

[51] L. Feng, X.-Y. He, J.-L. Zhu and W.-Y. Shi, *Magnetic manipulation of diamagnetic droplet on slippery liquid-infused porous surface*, Phys. Rev. Fluids **7**, 053602 (2022).

[52] S. Klumpp and D. Faivre, *Magnetotactic bacteria - Magnetic navigation on the microscale*, Eur Phys J Spec Top **225**, 2173 (2016).

[53] A. Petroff, A. Rosselli-Calderon B. Roque and P. Kumar, *Phases of active matter composed of multicellular magnetotactic bacteria near a hard surface*, Phys. Rev. Fluids **7**, 053102 (2022).

[54] L. González, W. Ruder, A. Mitchell, W. Messner and P. Leduc, *Sudden motility reversal indicates sensing of magnetic field gradients in Magnetospirillum magneticum AMB-1 strain*, The ISME journal **9**, 1399 (2014).

[55] S.S. Papell, *Low viscosity magnetic fluid obtained by colloidal suspension of magnetic particles*, US Patent 3,215,572 (1965).

[56] R.E. Rosensweig, *Ferrohydrodynamics* (Dover Publications, New York, United States, 2014).

[57] J.-C. Bacri, R. Perzynski, D. Salin, V. Cabuil and R. Massart, *Phase diagram of an ionic magnetic colloid: Experimental study of the effect of ionic strength*, J. Colloid Interface Sci. **132**, 43 (1989).

[58] H. Knieling, R. Richter, I. Rehberg, G. Matthies and A. Lange, *Growth of surface undulations at the Rosensweig instability*, Phys. Rev. E **76**, 066301 (2007).

[59] M.D. Cowley and R.E. Rosensweig, *The interfacial stability of a ferromagnetic fluid*, J. Fluid Mech. **30**, 671 (1967).

[60] F. Boyer and E. Falcon, *Wave Turbulence on the Surface of a Ferrofluid in a Magnetic Field*, Phys. Rev. Lett. **101**, 244502 (2008).

[61] B. Abou, G. Néron De Surgy and J. Wesfreid, *Dispersion Relation in a Ferrofluid Layer of Any Thickness and Viscosity in a Normal Magnetic Field; Asymptotic Regimes*, J. Phys II France **7**, 1159 (1997).

[62] F. Pétrélis, E. Falcon and S. Fauve, *Parametric stabilization of the Rosensweig instability*, Eur. Phys. J. B **15**, 3 (2000).

[63] S. Dorbolo and E. Falcon, *Wave turbulence on the surface of a ferrofluid in a horizontal magnetic field*, Phys. Rev. E **83**, 046303 (2011).

[64] D.R. Lide, *CRC Handbook of Chemistry and Physics* (CRC Press, Boca Raton, United States, 2005).

[65] F. Elias, J.-C. Bacri, C. Flament, E. Janiaud, D. Talbot, W. Drenckhan-Andreatta, S. Hutzler and D. Weaire, *Magnetic soap films and magnetic soap foams*, Aspects **263**, 65 (2005).

[66] K. Golemanov, N.D. Denkov, N.D. Tcholakova, M. Vethamuthu and A. Lips, *Surfactant Mixtures for Control of Bubble Surface Mobility in Foam Studies*, Langmuir **24**, 9956 (2008).

[67] W.N Bond and D.A. Newton, *LXXXII. Bubbles, drops, and Stokes' law. (Paper 2)*, Lond. Edinb. Dublin philos. mag. j. sci. **5**, 794 (1928).

[68] J.D. Sartor, *Electricity and Rain*, Phys. Today **22**, 45 (1969).

[69] C.T.R Wilson, *Some Thundercloud Problems*, J. Franklin Inst. **208**, 1 (1929).

[70] C.T.R Wilson, *A Theory of Thunder Cloud Electricity*, Proc. R. Soc. Lond. A **236**, 297 (1956).

[71] W.A. Macky, *Some Investigations on the Deformation and Breaking of Water Drops in Strong Electric Fields*, Proc. R. Soc. Lond. A **133**, 565 (1931).

[72] J.J. Nolan and J.G. O'Keeffe, *Electric Discharge from Water Drops*, Proc. R. Ir. Acad. A **40**, 86 (1932).

[73] Lord Rayleigh, *The Influence of Electricity on Colliding Water Drops*, Proc. R. Soc. Lond. A **28**, 406 (1879).

[74] N. Ashgriz and J.Y. Poo, *Coalescence and separation in binary collisions of liquid drops*, J. Fluid Mech. **221**, 183 (1990).

[75] C. Gotaas, P. Havelka, H.A. Jakobsen and H.F. Svendsen, *Evaluation of the impact parameter in droplet-droplet collision experiments by the aliasing method*, Phys. Fluids **19**, 102105 (2007).

[76] M. Brandenbourger, H. Caps, Y. Vitry and S. Dorbolo, *Electrically Charged Droplets in Microgravity. Impact and Trajectories*, Microgravity Sci. Technol. **29**, 229 (2017).

[77] M. Brandenbourger and S. Dorbolo, *Electrically charged droplet: case study of a simple generator*, Can. J. Phys. **92**, 1203 (2014).

[78] M. Brandenbourger, N. Vandewalle and S. Dorbolo, *Displacement of an Electrically Charged Drop on a Vibrating Bath*, Phys. Rev. Lett. **116**, 044501 (2016).

[79] D.J. Griffiths, *Introduction to Electrodynamics* (Prentice Hall, New Jersey, United States, 1999).

[80] O.A. Basaran and L.E. Scriven, *Axisymmetric Shapes and Stability of Isolated Charged Drops*, Phys. Fluids A **1**, 799 (1989).

[81] Lord Rayleigh, *On the Equilibrium of Liquid Conducting Masses Charged with Electricity*, Philos. Mag. **14**, 184 (1882).

[82] D. Duft, H. Lebius, B.A. Huber, C. Guet and T. Leisner, *Shape Oscillations and Stability of Charged Microdroplets*, Phys. Rev. Lett. **89**, 084503/1 (2002).

[83] D. Duft, T. Achtzehn, R. Müller, B.A. Huber and T. Leisner, *Rayleigh Jets from Levitated Microdroplets*, Nature **421**, 128 (2003).

[84] O.A. Basaran and L.E. Scriven, *Axisymmetric Shapes and Stability of Charged Drops in an External Electric Field*, Phys. Fluids A **1**, 795 (1989).

[85] G. Iooss and D.D. Joseph, *Elementary Stability and Bifurcation Theory* (Springer, New York, United States, 1990).

[86] B.W. Wagoner, P.M. Vlahovska, M.T. Harris and O.A. Basaran, *Electric-field-induced transitions from spherical to discocyte and lens-shaped drops*, J. Fluid Mech **904**, R4 (2020).

[87] A. Marin, *The Saturnian droplet*, J. Fluid Mech **908**, F1 (2020).

[88] Q. Brosseau and P.M. Vlahovska, *Streaming from the Equator of a Drop in an External Electric Field*, Phys. Rev. Lett. **119**, 034501 (2017).

[89] K.J. Ptasinski and P.J.A.M. Kerkhof, *Electric Field Driven Separations : Phenomena and Applications*, Sep. Sci. Technol. **27**, 995 (1992).

[90] W. Dong, R.Y. Li, H.L. Yu and Y.Y. Yan, *An Investigation of Behaviours of a Single Bubble in a Uniform Electric Field*, Exp. Therm. Fluid Sci. **30**, 579 (2006).

[91] J. Zeleny, *On the Condition of Instability of Electrified Drops, with Application to the Electrical Discharge from Liquid Point*, Proc. Cambridge Philos. Soc. **18**, 71 (1915).

[92] J. Zeleny, *Instability of Electrified Liquid Surfaces*, Phys. Rev. **10**, 1 (1917).

[93] J. Zeleny, *The Role of Surface Instability in Electrical Disharge from Drops of Alcohol and Water in Air at Atmospheric Pressure*, J. Franklin Inst. **219**, 659 (1935).

[94] M. Cloupeau and B. Prunet-Foch, *Electrostatic Spraying of Liquids in Cone-jet Mode*, J. Electrostat. **22**, 135 (1989).

[95] M. Cloupeau and B. Prunet-Foch, *Electrostatic Spraying of Liquids: Main Functioning Modes*, J. Electrostat. **25**, 165 (1990).

[96] R.T. Collins, J.J. Jones, M.T. Harris and O.A. Basaran, *Electrohydrodynamic Tip Streaming and Emission of Charged Drops from Liquid Cones*, Nat. Phys. **4**, 149 (2008).

[97] Y.M. Shin, M.M. Hohman, M.P. Brenner and G.C. Rutledge, *Experimental Characterization of Electrospinning the Electrically Forced Jet and Instabilities*, Polymer **42**, 09955 (2001).

[98] J.-U. Park, M. Hardy, S.J. Kang, K. Barton, K. Adair, D.K. Mukhopadhyay, C.Y. Lee, M.S. Strano, A.G. Alleyne, J.G. Georgiadis, P.M. Ferreira and J.A. Rogers, *High-resolution Electrohydrodynamic Jet Printing*, Nat. Mater. **6**, 782 (2007).

[99] M. Gamero-Castaño and V. Hruby, *Electrospray as a Source of Nanoparticles for Effcient Colloid Thrusters*, J. Propuls. Power **17**, 977 (2001).

[100] I.G. Loscertales, A. Barrero, I. Guerrero, R. Cortijo, M. Marquez and A.M. Gañán-Calvo, *Micro/Nano Encapsulation via Electrified Coaxial Liquid Jets*, Science **295**, 1695 (2002).

[101] K. Kataria, A. Gupta, G. Rath, R.B. Mathur and S.R. Dhakate, *In Vivo Wound Healing Performance of Drug Loaded Electrospun Composite Nanofibers Transdermal Patch*, Int. J. Pharm. **469**, 102 (2014).

[102] C.J. Luo, S. Loh, E. Stride and M. Edirisinghe, *Electrospraying and Electrospinning of Chocolate Suspensions*, Food Bioproc Tech **5**, 2285 (2012).

[103] J.B. Fenn, M. Mann, C.K. Meng, S.F. Wong and C.M. Whitehouse, *Electrospray Ionization for Mass Spectrometry of Large Biomolecules*, Science **246**, 64 (1989).

[104] O.A. Basaran and L.E. Scriven, *Axisymmetric Shapes and Stability of Pendant and Sessile Drops in an Electric Field*, J. Colloid Interface Sci. **140**, 10 (1990).

[105] J.-C. Bacri, D. Salin and R. Massart, *Study of the deformation of ferrofluid droplets in a magnetic field*, J. Phys. Lett. **43**, 179 (1982).

[106] J.-C. Bacri and D. Salin, *Instability of ferrofluid magnetic drops under magnetic field*, J. Phys. Lett. **43**, 649 (1982).

[107] J.-C. Bacri and D. Salin, *Dynamics of the shape transition of a magnetic ferrofluid drop*, J. Phys. Lett. **44**, 415 (1983).

[108] A. Ivanov, O.B. Kuznetsova and I. Subbotin, *Magnetic properties of ferrofluid emulsions: Model of non-interacting droplets*, Magnetohydrodynamics **47**, 129 (2011).

[109] S. Afkhami, A.J. Tyler, Y. Renardy, M. Renardy, T.G. St. Pierre, R.C. Woodward and J.S. Riffle, *Deformation of a hydrophobic ferrofluid droplet suspended in a viscous medium under uniform magnetic fields*, J. Fluid Mech. **663**, 358 (2010).

[110] O. Lavrova, G. Matthies, V. Polevikov and L. Tobiska, *Numerical modeling of the equilibrium shapes of a ferrofluid drop in an external magnetic field*, Proc. Appl. Math. Mech **4**, 704 (2004).

[111] Y. Filali, M. Er-Riani and M. El Jarroudi, *The deformation of a ferrofluid drop under a uniform magnetic field*, Int J Non Linear Mech **99**, 173 (2018).

[112] P. Rowghanian, C.D. Meinhart and O. Campás, *Dynamics of ferrofluid drop deformations under spatially uniform magnetic fields*, J. Fluid Mech. **802**, 245 (2016).

[113] A. Lebedev, A. Engel, K. Morozov and H. Bauke, *Ferrofluid drops in rotating magnetic fields*, New J. Phys. **5**, 57 (2003).

[114] C. Rigoni, J. Fresnais, D. Talbot, R. Massart, R. Perzynski, J.-C. Bacri and A. Abou-Hassan, *Magnetic Field-Driven Deformation, Attraction, and Coalescence of Nonmagnetic Aqueous Droplets in an Oil-Based Ferrofluid*, Langmuir **36**, 5048 (2020).

[115] C. Rigoni, M. Pierno, M. Giampaolo, D. Talbot, R. Massart, J.-C. Bacri, A. Abou-Hassan, *Static Magnetowetting of Ferrofluid Drops*, Langmuir **32**, 7639 (2016).

[116] C. Rigoni, S. Bertoldo, M. Pierno, D. Talbot, A. Abou-Hassan and M. Giampaolo, *Division of Ferrofluid Drops Induced by a Magnetic Field*, Langmuir **34**, 9762 (2018).

[117] M. Latikka, M. Backholm, A. Baidya, A. Ballesio, A. Serve, G. Beaune, J.V.I. Timonen, T. Pradeep and R.H.A. Ras, *Ferrofluid Microdroplet Splitting for Population-Based Microfluidics and Interfacial Tensiometry*, Adv. Sci. **7**, 2000359 (2020).

[118] M. Latikka, B. Matilda, J.V.I Timonen and R.H.A Ras, *Wetting of ferrofluids: Phenomena and control*, Curr. Opin. Colloid Interface Sci. **36**, 118 (2018).

[119] R. Deb, B. Sarma and A. Dalal, *Magnetowetting dynamics of sessile ferrofluid droplets: a review*, Soft Matter **18**, 2287 (2022).

[120] T. Jamin, C. Py and E. Falcon, *Instability of the Origami of a Ferrofluid Drop in a Magnetic Field*, Phys. Rev. Lett. **107**, 204503 (2011).

[121] T. Langen, *Dipolar supersolids: Solid and superfluid at the same time*, Physics Today **75**, 36 (2022).

[122] L.B. King, E. Meyer, M.A. Hopkins, B.S. Hawkett and N. Jain, *Self-Assembling Array of Magnetoelectrostatic Jets from the Surface of a Superparamagnetic Ionic Liquid*, Langmuir **30**, 14143 (2014).

[123] J. Miguet, *Amincissement et stabilité de bulles de surface*, PhD Thesis, Université Paris Saclay (2019).

[124] S. Arscott, *Wetting of soap bubbles on hydrophilic, hydrophobic, and superhydrophobic surfaces*, Appl. Phys. Lett. **102**, 254103 (2013).

[125] M. Clerget, A. Delvert, L. Courbin and P. Panizza, *Different scenarios of shrinking surface bubbles*, Am. J. Phys. **89**, 244 (2021).

[126] H. Lhuissier and E. Villermaux, *Bursting bubble aerosols*, J. Fluid Mech. **696**, 5 (2012).

[127] G. Liger-Belair, *The Physics Behind the Fizz in Champagne and Sparkling Wines*, Eur. Phys. J. Spec. Top. **201**, 1 (2012).

[128] A. Pelesz, *Charging of a Single Soap Bubble*, Przeglad Elektrotechniczny **2018**, 176 (2018).

[129] J.E. Hilton and A. van der Net, *Dynamics of Charged Hemispherical Soap Bubbles*, EPL **86**, 24003 (2009).

[130] D.E. Moulton and J.A. Pelesko, *Theory and experiment for soap-film bridge in an electric field*, J. Colloid Interf. Sci. **322**, 252 (2008).

[131] A. Lukichev, *Physical Meaning of the Stretched Exponential Kohlrausch Function*, Phys. Lett. A **383**, 2983 (2019).

[132] G.I. Barenblatt, *Scaling, Self-similarity, and Intermediate Asymptotics* (Cambridge University Press, Cambridge, UK, 1996).

[133] M.M. Wind, J. Vlieger and D. Bedeaux, *The Polarizability of a Truncated Sphere on a Substrate {I}*, Physica A **141**, 33 (1987).

[134] M.T. Harris and O.A. Basaran, *Capillary Electrohydrostatics of Conducting Drops Hanging from a Nozzle in an Electric Field*, J. Colloid Interface Sci. **161**, 389 (1993).

[135] F. Elias, C. Flament, J.-C. Bacri and S. Neveu, *Macro-Organized Patterns in Ferrofluid Layer: Experimental Studies*, J. Phys. I France **7**, 711 (1997).

[136] C. Schneider, W.S. Rasband and K.W. Eliceiri, *NIH Image to ImageJ: 25 years of image analysis*, Nat. Chem. Biol **9**, 671 (2012).

[137] J.A. Osborn, *Demagnetizing Factors of the General Ellipsoid*, Phys. Rev. **67**, 351 (1945).

[138] M. Beleggia, D. Vokoun and M. De Graef, *Demagnetization factors for cylindrical shells and related shapes*, J. Magn. Magn. Mater. **321**, 1306 (2009).

[139] O. Bonhomme, O. Liot, A.-L. Biance and L. Bocquet, *Soft Nanofluidic Transport in a Soap Film*, Phys. Rev. Lett. **110**, 054502 (2013).

[140] A. Lafuma and D. Quéré, *Superhydrophobic states*, Nat. Mater. **2**, 457 (2003).

[141] T. Darmanin and F. Guittard, *Superhydrophobic and superoleophobic properties in nature*, Mater. Today **18**, 273 (2015).

[142] K.H. Kang, *How Electrostatic Fields Change Contact Angle in Electrowetting*, Langmuir **18**, 10318 (2002).

[143] J. Buehrle, S. Herminghaus and F. Mugele, *Interface Profiles near Three-Phase Contact Lines in Electric Fields*, Phys. Rev. Lett. **91**, 086101 (2003).

[144] J.D. Berry, M.J. Neeson, R.R. Dagastine, D.Y.C. Chan and R.F. Tabor, *Measurement of Surface and Interfacial Tension Using Pendant Drop Tensiometry*, J. Colloid Interf. Sci. **454**, 226 (2015).

[145] G. Debrégeas, P.-G. de Gennes and F. Brochard-Wyart, *The Life and Death of "Bare" Viscous Bubbles*, Science **279**, 1704 (1998).

[146] A. Aradian, E. Raphael and P.-G. de Gennes, *"Marginal pinching" in soap films*, EPL **55**, 834 (2001).

[147] J. Miguet, M. Pasquet, F. Rouyer, Y. Fang and E. Rio, *Marginal regeneration-induced drainage of surface bubbles*, Phys. Rev. Fluids **6**, L101601 (2021).

[148] L. Champougny, M. Roché, W. Drenckhan and E. Rio, *Life and death of not so "bare" bubbles*, Soft Matter **12**, 5276 (2016).

[149] O. Atasi, D. Legendre, B. Haut, R. Zenit and B. Scheid, *Lifetime of Surface Bubbles in Surfactant Solutions*, Langmuir **36**, 7749 (2020).

[150] S. Poulain, E. Villermaux and L. Bourouiba, *Ageing and burst of surface bubbles*, J. Fluid Mech. **851**, 636 (2018).

[151] B. Néel and E. Villermaux, *The spontaneous puncture of thick liquid films*, J. Fluid Mech. **838**, 192 (2017).

[152] E. Rio and A.-L. Biance, *Thermodynamic and Mechanical Timescales Involved in Foam Film Rupture and Liquid Foam Coalescence*, Chemphyschem **15**, 3692 (2014).

[153] L. Champougny, J. Miguet, R. Henaff, F. Restagno, F. Boulogne and E. Rio, *Influence of Evaporation on Soap Film Rupture*, Langmuir **34**, 3221 (2018).

[154] G.I. Taylor, *The dynamics of thin sheets of fluid. III. Disintegration of fluid sheets*, Proc. R. Soc. Lond. A **253**, 313 (1959).

[155] F.E.C. Culick, *Comments on a Ruptured Soap Film*, J. Appl. Phys. **31**, 1128 (1960).

[156] W.R. McEntee and K.J. Mysels, *Bursting of soap films. I. An experimental study*, J. Phys. Chem. A **73**, 3018 (1969).